

**ALMA MATER STUDIORUM  
UNIVERSITÀ DI BOLOGNA**

SCUOLA DI INGEGNERIA E ARCHITETTURA  
- Sede di Forlì -

CORSO DI LAUREA  
IN INGEGNERIA AEROSPAZIALE  
Classe: LM-20

TESI DI LAUREA  
in TOLLERANZA AL DANNO LM

**CHARACTERIZATION OF MODE I DISBONDING  
BEHAVIOUR OF CARBON/EPOXY COMPOSITES BONDED  
WITH TWO ADHESION QUALITIES**

CANDIDATO  
Matteo Careddu

RELATORE:  
Prof. Enrico Troiani

CORRELATORE:  
Dr.ir. René Alderliesten

CONTRORELATORE:  
Prof. Alessandro Airoidi

Anno Accademico 2012/13

Sessione II



*Never give up control, live life on your own terms.  
One of these times, hell! maybe even today day,  
I'm gonna hear some bad news, but until then, who's in charge? Me!  
That's how I live my life.*

*Walter White*



# Abstract

---

I materiali compositi hanno assunto significativa importanza per l'industria aerospaziale. Le principali ragioni sono da ricondurre alla sostanziale riduzione del peso strutturale e ai vantaggi introdotti nel comportamento meccanico delle strutture, come la maggiore resistenza e rigidità per unità di peso se comparati con l'alluminio tradizionale. D'altro canto i compositi laminati sono soggetti a fenomeni preoccupanti quali la delaminazione, che può essere brevemente descritta come un modo di cedimento rappresentato dallo sviluppo di una cricca tra gli strati del materiale.

La mancanza di procedure standard per la verifica delle strutture in compositi, al contrario dei materiali metallici, porta all'esigenza di una continua ricerca nel settore, al fine di ottenere risultati significativi che culminino in una standardizzazione delle procedure.

In tale contesto si colloca il presente elaborato di laurea. La ricerca svolta per la stesura dello stesso è stata condotta presso il laboratorio *DASML* del *TU Delft*, nei Paesi Bassi. Il materiale studiato è un *prepreg* (*preimpregnated*) costituito da fibre di carbonio (*M30SC*) e matrice epossidica (*DT120*) con la particolare configurazione  $[0^\circ/90^\circ/\pm 45^\circ/\pm 45^\circ/90^\circ/0^\circ]$ . L'adesivo utilizzato per l'incollaggio è di tipo epossidico (*FM94K*). Il materiale è stato assemblato in laboratorio in modo da ottenere i provini da testare, di tipo *DCB*, *ENF* e *CCP*. Due differenti qualità dello stesso materiale sono state ottenute, una *buona* ottenuta seguendo le istruzioni del produttore, ed una *povera* ottenuta modificando il processo produttivo suggerito, che risulta in un incollaggio di qualità nettamente inferiore rispetto al primo tipo di materiale.

Lo scopo era quello di studiare i comportamenti di entrambe le qualità sotto due diversi modi di carico, modo I o *opening mode* e modo II o *shear mode*, entrambi attraverso test quasi-statici e a fatica, così da ottenere risultati comparabili tra di essi che permettano in futuro di identificare se si dispone di un materiale di buona qualità prima di procedere con il progetto dell'intera struttura.

L'approccio scelto per lo studio dello sviluppo della delaminazione è un adattamento della teoria della Meccanica della Frattura Lineare Elastica (*LEFM*), che permette di calcolare i valori dell'Energia di Deformazione Elastica  $G$  (*SERR*, *Strain Energy Release Rate*) da confrontare con il valore critico  $G_{Ic}$  o  $G_{IIc}$  (*IFT*, *Interlaminar Fracture Toughness*). La *SERR* si utilizza nello studio dei compositi in una legge di tipo Paris analogamente allo Stress Intensity Factor (*SIF*) per i metalli. Nel caso dei test a fatica viene utilizzato un metodo particolare per definire la  $G_{eff}$  da utilizzare, il quale differisce da quelli generalmente proposti, ma si dimostra essere più coerente nell'analogia tra la *SERR* per i compositi e lo *SIF* per i metalli.

I test sotto carico in modo I sono stati condotti nel rispetto degli standard proposti dalla *ASTM* (*American Society for Testing and Materials*), ai quali viene dedicato ampio spazio nella trattazione. In particolare per il modo II di carico il lavoro di ricerca è stato iniziato con la produzione dei provini ma essi non sono stati testati per via della brevità del tempo a disposizione per la ricerca; vengono pertanto proposti i diversi approcci presenti in letteratura con l'intenzione di agevolare chi intenderà portare avanti il lavoro di sperimentazione.

I risultati ottenuti dai test in laboratorio portano ad affermare che le differenze sono dovute al differente processo di incollaggio seguito in fase di manifattura. In generale le due qualità presentano risultati concordanti, in quanto essi possono essere ottenuti dall'una o dall'altra semplicemente traslando le curve, che presentano lo stesso andamento, verso differenti range di valori, sia per i test quasi-statici che per quelli a fatica. La conclusione cui si è giunti è che per ottenere un materiale che presenti buone caratteristiche in termini di resistenza, rigidità e risposta alla delaminazione, devono necessariamente essere seguite le istruzioni fornite dai produttori, in modo tale da evitare i rischi di fallimenti catastrofici delle strutture in servizio.

# Contents

---

Abstract	v
Symbols	ix
Subscripts	xi
Abbreviations	xii
List of figures	xiii
List of tables	xvi
1. Introduction	1
2. Literature Review	3
2.1 Composite Materials Introduction	3
2.1.1 Fibrous Composite Materials	3
2.1.2 Laminate Composite Materials	5
2.1.3 Particulate Composite Materials	6
2.1.4 Combination of composite materials	6
2.2 Material Characterisation	6
2.2.1 Mechanical Behaviour of Composite Materials	6
2.2.2 Terminology of Laminated Fibre-Reinforced Composite Materials	7
2.3 Laminates failure	9
2.3.1 Modes of failure	9
2.3.2 Theories of adhesion and nature of bonding	10
2.3.3 Adhesive Bonding	11
2.3.4 Disbonding	12
2.3.5 Delamination	13
2.3.6 Linear Elastic Fracture Mechanics approach	13
2.4 Manufacturing Process Introduction	14
2.4.1 Layup processes	14
2.4.2 Curing	15
3. Specimens Manufacturing	17
3.1 Material Properties	17
3.2 Mode I tests – <i>DCB</i> specimens	17
3.2.1 Good Quality material	18
3.2.2 Poor Quality material	26
3.3 Mode II tests	30
3.3.1 <i>ENF</i> specimens	30
3.3.2 <i>CCP</i> specimens	31
4. Mode I Interlaminar Fracture Toughness Tests	34
4.1 Quasi-static test	34
4.1.1 Procedure	34
4.1.2 Calculation method	36
4.2 Fatigue test	38
4.2.1 Procedure	38
4.2.2 Calculation method	40

5. Mode II Interlaminar Fracture Toughness Tests	<b>44</b>
5.1 Three-point bending test	45
5.2 Central cut plies specimen test	52
6. Test Results	<b>58</b>
6.1 Quasi-Static tests	58
6.1.1 Good Quality material	58
6.1.2 Poor Quality material	73
6.2 Fatigue tests	83
6.2.1 Good Quality material	83
6.2.2 Poor Quality material	89
7. Discussion	<b>93</b>
7.1 Quasi-Static tests	93
7.2 Fatigue tests	98
8. Conclusions	<b>102</b>
References	<b>104</b>
Acknowledgements	<b>107</b>

## Symbols

a	Crack length	mm
b	Width	mm
$b_1, b_2$	Exponents in Incremental Polynomial Method	-
h	Thickness	mm
$h_d$	Constant Paris Law	-
l	Distance between supporting-point cracked portion to strain gauge	mm
m	Coefficient for mode II data reduction method	-
n	Exponent in Compliance Calibration Method	-
t	Cut plies thickness	mm
A	Coefficient for mode II data reduction method	-
$A_1$	Correction factor in Modified Compliance Calibration Method	-
C	Compliance	mm/N
$C_d$	Constant in Paris Law	-
$C_1, C_2$	Coefficients in Incremental Polynomial Method	-
da/dN	Crack growth rate	mm/N
E	Modulus of elasticity	N/m <sup>2</sup>
G	Strain energy release rate	J/m <sup>2</sup>
I	Second moment of cross-sectional area in crack-free portion	mm <sup>4</sup>
I'	Second moment of cross-sectional area in cracked portion	mm <sup>4</sup>
L	Length	mm
K	Stress Intensity Factor	N/ $\sqrt{m}$
N	Number of elapsed cycles	-
N	Constant in Incremental Polynomial Method	-
P	Load	N
R	Ratio of minimum load to maximum load	-
S	Load severity	-
$S_R$	Standard Deviation	-
$(CV)_R$	Coefficient of variation	%
$\alpha$	Coefficient in Central Cut Ply data reduction method	-
$\gamma$	Correction factor in Classical data reduction methods for mode II	-
$\delta$	Vertical displacement	mm
$\varepsilon$	Strain	-
$\sigma$	Stress	N/m <sup>2</sup>
$\chi$	Ratio of cut plies to number of total layers	-

$\Delta$	Correction factor in Modified Beam Theory	-
$\Delta a$	Crack length increment	mm
$\Delta G$	Strain Energy Release Rate increment	J/m <sup>2</sup>
$\Delta G_{\sqrt{}}$	Fracture parameter	J/m <sup>2</sup>
$\Delta \epsilon$	Strain increment	-
$\Delta K$	Stress Intensity Factor increment	N/ $\sqrt{m}$
$\Delta P$	Load increment	N

## *Subscripts*

a	Onset
appl	Applied
av	Average
c, cr	Critical
corr	Corrected
e	Equivalent
eff	Effective
in	Inner
out	Outer
max	Maximum
min	Minimum
net	Net section
prop	Propagation

CCM Compliance Calibration Method

MBT Modified Beam Theory

I Mode I

II Mode II

L Longitudinal

NL Non-linear

P Propagation

S Strain

T Total

0 Initial

1, 11 Longitudinal

13, 3 Transverse

## *Abbreviations*

AITM	Airbus Industries Test Method
ASTM	American Society for Testing and Material
CBBM	Compliance Based Beam Method
CCC	Coordinate Conversion Control
CCM	Compliance Calibration Method
CCP	Central Cut Ply
CFRP	Carbon Fibre Reinforced Composite Polymers
CSD	Crack Shear Displacement
DASML	Delft Aerospace Structures and Material Laboratory
DCB	Double Cantilever Beam
ENF	End-Notched Flexure
FPF	First Ply Failure
FPZ	Fracture Process Zone
FRP	Fibre Reinforced Polymer
GLARE	Glass Laminate Aluminium Reinforced Epoxy
IFT	Interlaminar Fracture Toughness
JIS	Japan Industrial Standards
LEFM	Linear Elastic Fracture Mechanics
MBT	Modified Beam Theory
NL	Non-Linearity
PAN	Polyacrylonitrile
RT	Room Temperature
RTM	Resin Transfer Moulding
SEM	Scanning Electron Microscopy
SERR	Strain Energy Release Rate
SIF	Stress Intensity Factor
SMC	Sheet Moulding Compound
TU	Technische Universiteit Delft
UD	Unidirectional
VIS	Visual observation

## List of figures

Figure 2.1	Types of polymers	5
Figure 2.2	Types of typical stress-strain behaviour	8
Figure 2.3	Types of laminates	9
Figure 2.4	Loading modes	10
Figure 2.5	General cure cycle	16
Figure 3.1	Double Cantilever Beam specimen	18
Figure 3.2	M30SC/TD120 roll	18
Figure 3.3	Mode I plates preparation	19
Figure 3.4	Vacuum bag	20
Figure 3.5	Autoclave for cure cycle	20
Figure 3.6	Laminae after first cure cycle	21
Figure 3.7	Good quality C-scan inspection results after first cure cycle	21
Figure 3.8	Good quality C-scan inspection results after second cure cycle	23
Figure 3.9	Double Cantilever Beam specimen dimensions	23
Figure 3.10	Good quality Double Cantilever Beam plate layout	24
Figure 3.11	Cut process, Unitom machine	25
Figure 3.12	DCB specimen ready to be tested	26
Figure 3.13	Poor quality C-scan inspection results after first cure cycle	26
Figure 3.14	Poor quality C-scan inspection results after second cure cycle	27
Figure 3.15	Poor quality Double Cantilever Beam plate layout	28
Figure 3.16	Poor quality DCB specimen separated while cutting	28
Figure 3.17	End-Notched Flexure specimen	29
Figure 3.18	End-Notched Flexure plate layout	30
Figure 3.19	Central Cut Ply specimen	31
Figure 3.20	CCP plate solution adopted against cure cycle pressure	31
Figure 3.21	CCP specimen: unloaded central plies	31
Figure 3.22	Central Cut Ply plate layout	32
Figure 4.1	Log C versus log a example plot	36
Figure 4.2	C versus N general plot	38
Figure 4.3	da/dN vs. a plot: comparison secant vs. polynomial method	40
Figure 4.4	Crack growth rate general plot	41
Figure 5.1	Three-point bending test example	44
Figure 5.2	Three-point bending test set up, strain gauge	49
Figure 5.3	P vs. $\delta$ and P vs. $\epsilon_x$ general plots	49
Figure 5.4	$G_{IIR}$ vs. $\Delta a$ general plots	49
Figure 5.5	Central Cut Ply test example	51
Figure 5.6	a vs. N example plot	52

Figure 5.7	$da/dN$ vs. $\Delta G_{\sqrt{}}$ example plot	53
Figure 5.8	$da/dN$ vs. $\Delta G/G_c$ example plot	54
Figure 5.9	$da/dN$ vs. $G_{II\max}/G_{IIc}$	56
Figure 6.1	DCB test example	57
Figure 6.2	P vs. $\delta$ plots, good quality specimens	58
Figure 6.3	R8 specimen: P vs. $\delta$ plot, load drop	59
Figure 6.4	R3 specimen: P vs. $\delta$ plot, load drop	59
Figure 6.5	Mode I good quality tests, example picture	60
Figure 6.6	Log C vs. log a good quality plots	61
Figure 6.7	$C^{1/3}$ vs. a good quality plots	62
Figure 6.8	$G_{Ic\ CCM}$ vs. $\Delta a$ good quality plots	65
Figure 6.9	$G_{Ic\ MBT}$ vs. $\Delta a$ good quality plots	65
Figure 6.10	$G_{Ic}$ good quality onset values	66
Figure 6.11	“Vague” region ahead the crack tip	67
Figure 6.12	Good quality specimen failure, cohesive vs. adhesive	68
Figure 6.13	$G_{Ic}$ vs. $\Delta a$ : comparison between CCM and MBT, good quality	68
Figure 6.14	Good quality specimen, fibre bridging example	70
Figure 6.15	Optical microscope inspection of adhesive, good quality material	71
Figure 6.16	P vs. $\delta$ plots, poor quality specimens	72
Figure 6.17	Poor quality specimens, mode I test final state	73
Figure 6.18	Log C vs. log a poor quality plots	74
Figure 6.19	$C^{1/3}$ vs. a poor quality plots	75
Figure 6.20	$G_{Ic\ CCM}$ vs. $\Delta a$ poor quality plots	76
Figure 6.21	$G_{Ic\ MBT}$ vs. $\Delta a$ poor quality plots	77
Figure 6.22	$G_{Ic}$ poor quality onset values	78
Figure 6.23	$G_{Ic}$ vs. $\Delta a$ : comparison between CCM and MBT, poor quality	79
Figure 6.24	Poor quality specimen, fibre bridging example	80
Figure 6.25	Poor quality specimen failure, adhesive failure	81
Figure 6.26	C vs. N good quality plots	83
Figure 6.27	$G_{I\max}$ vs. $\Delta a_1$ good quality plots	84
Figure 6.28	Representation of $\Delta a_1$ and $\Delta a_2$	85
Figure 6.29	$G_{I\max}$ vs. $\Delta a_2$ good quality plots	86
Figure 6.30	$\Delta G_{\sqrt{}}$ vs. N good quality plots	86
Figure 6.31	$da/dN$ vs. $\Delta G_{\sqrt{}}$ good quality plots	87
Figure 6.32	Fibre bridging examples, good quality	87
Figure 6.33	C vs. N poor quality plots	88
Figure 6.34	$G_{I\max}$ vs. $\Delta a_2$ poor quality plots	89
Figure 6.35	$\Delta G_{\sqrt{}}$ vs. N poor quality plots	90
Figure 6.36	$da/dN$ vs. $\Delta G_{\sqrt{}}$ poor quality plots	90

Figure 6.37	3D plot: $da/dN$ as a function of $\Delta G_{\sqrt{}}$ and $G_{\max}$ , poor quality	91
Figure 6.38	Fibre bridging example, poor quality	92
Figure 7.1	P vs. $\delta$ plots: comparison between good and poor quality	93
Figure 7.2	P vs. $\delta$ general plot: slope definition	94
Figure 7.3	P vs. $\delta$ plot slope: comparison between D2 and R3	95
Figure 7.4	$G_{Ic\ CCM}$ vs. $\Delta a$ plots: comparison between good and poor quality	96
Figure 7.5	$G_{Ic\ MBT}$ vs. $\Delta a$ plots: comparison between good and poor quality	96
Figure 7.6	$da/dN$ vs. $\Delta G_{\sqrt{}}$ plots: comparison between good and poor quality	98
Figure 7.7	$G_{I\max}$ vs. $\Delta a_2$ plots: comparison between good and poor quality	99
Figure 7.8	$\Delta G_{\sqrt{}}$ vs. N plots: comparison between good and poor quality	100
Figure 7.9	C vs. N plots: comparison between good and poor quality	101

## *List of tables*

Table 3.1	M30SC fibres properties	17
Table 3.2	DT120 epoxy properties	17
Table 3.3	FM94 adhesive properties	22
Table 6.1	Good quality quasi-static test collected data: R1 specimen	60
Table 6.2	Good quality $n$ values	61
Table 6.3	Good quality $\Delta$ values	61
Table 6.4	Good quality SERR values, Compliance Calibration Method	63
Table 6.5	Good quality SERR values, Modified Beam Theory	64
Table 6.6	Good quality $G_I$ onset values: comparison between Visual and NL	67
Table 6.7	Poor quality quasi-static test collected data: S2 specimen	73
Table 6.8	Poor quality $n$ values	74
Table 6.9	Poor quality $\Delta$ values	75
Table 6.10	Poor quality SERR values, Compliance Calibration Method	76
Table 6.11	Poor quality SERR values, Modified Beam Theory	77
Table 6.12	Poor quality $G_I$ onset values: NL	79
Table 6.13	Good quality fatigue test collected data: L4 specimen	83
Table 6.14	Poor quality fatigue test collected data: D9 specimen	88
Table 7.1	Maximum load: comparison between good and poor quality	93
Table 7.2	$G_{Ic}$ vs. $\Delta a$ slopes: comparison between quality and methods	95
Table 7.3	$G_{IcAV}$ values: comparison between good and poor quality	98
Table 7.4	Highest $G_{I_{max}}$ values: comparison between good and poor quality	99





# 1. Introduction

---

The present report illustrates the work carried out during the final thesis to complete the Master of Science degree in Aerospace Engineering at University of Bologna.

A study was conducted on a composite material, the unidirectional carbon/epoxy prepreg *M30SC/TD120* supplied by Delta-Tech. The tested plates were bonded with the *FM94K* epoxy adhesive in order to obtain the particular configuration  $[0^\circ/90^\circ/\pm 45^\circ/\pm 45^\circ/90^\circ/0^\circ]$ .

Composite materials nowadays have captured the interest of aerospace industry. This is mainly due to the significant reduction introduced in structural weight and some advantages in mechanical behaviour such as the higher strength and stiffness to weight ratio if compared with metal alloys. On the other hand composites made of laminates exhibit a worrying susceptibility toward a phenomenon identified as delamination, which can be briefly described as the growth of cracks between the layers. Delamination represents one of the most life-consuming failure modes of laminated composites.

Thus a literature review is furnished in *Chapter 2* to introduce the reader to the world of composite materials and describe their features, the mechanical behaviour and the methods to study it.

In particular the aim of the present work was to reach a description of the behaviour of two different qualities of the mentioned material, denoted as *good* and *poor* qualities and compare them. The first one was obtained following the instructions given by the suppliers of both the prepreg and the adhesive, while the second quality was manufactured changing the characteristics of the bonding process.

The plates were manufactured and tested in the *DASML Lab* at *TU Delft*. The manufacturing processes are accurately described in *Chapter 3*.

Tests were carried on to study material behaviour under mode I loading so to determine both the interlaminar fracture toughness through quasi-static tests and the delamination crack growth through fatigue tests. *Chapter 4* reports the procedures deduced by the standards actually available and the data reduction methods utilized to process the acquired data.

Mode II tests with the same propose were initially planned, but the limited period available to carry on the research did not allow to perform these tests. The approach chose to conduct them is nevertheless presented in *Chapter 5*, in the event that they will be retained appropriate for testing the manufactured plates in the future.

*Chapter 6* illustrates the results found out both for *good* and *poor* quality. The substantial points were enfaced in the way to furnish the description of the parameters suggested in the standards and trying to analyse some phenomena occurred during the tests' progress. Every aspect analysed is supported by tables of values, graphs and images where necessary.

A discussion on the results reached is presented in *Chapter 7*. In particular the attention is focused on a comparison between the two qualities, in order to furnish a model to describe and identify them.

The conclusions drawn from the carried experimental work and its analysis are exposed in *Chapter 8*.

## 2. Literature Review

---

### *2.1 Composite materials introduction*

Composite materials have reached a commercial use in the aircraft industry after World War Second, when firstly have been applied to military aircrafts [2].

A composite could be defined as follows: two or more materials combined on a macroscopic scale to form a useful third material. The latter exhibits the best qualities of its components or constituents and sometimes also qualities that it neither have. These qualities could be primarily resumed as:

- Strength
- Stiffness
- Weight reduction (compared to metallic alloys)
- Fatigue life
- Corrosion resistance
- Wear resistance
- Attractiveness
- Temperature-dependent behaviour
- Thermal insulation
- Thermal conductivity
- Acoustical insulation

Of course not all the composite materials have all of these characteristics simultaneously, or better, they show all these properties but some of the values cannot be good enough. The final goal is to create a material which only has the properties necessary to perform the design task; for that reason some of the above characteristic may be in contrast between them.

Composite materials could be classified in four main categories:

1. Fibrous Composite Materials
2. Laminated Composite Materials
3. Particulate Composite Materials
4. Combinations of the above

Each category will be presented in the following paragraphs.

#### *2.1.1 Fibrous composite materials*

A fibre has a more perfect structure than the bulk form, because crystals are aligned along the fibre axis; therefore long fibres in various forms are much more stiffer and stronger than the same material in the bulk form. They also present fewer internal defects than bulk materials; for example in materials that present dislocations, the fibre form has fewer dislocations than

the bulk one. A dislocation can be commonly described as a change in relation of the crystal, i.e. a crystallographic defect inside a crystal structure, which strongly affects material properties, such as the stiffness and the strength.

Note carefully that a comparison between fibres and metals is not really valid because fibres need a matrix surrounding them to perform in a structural member, while metals are “ready to use”.

Each component of a fibrous composite material presents several properties; they can be resumed as follows:

- a. *Properties of fibres*: Fibres are geometrically characterised by a high length-to-diameter ratio and by near-crystal-sized diameter.  
Nowadays commonly used fibres are the graphite and carbon ones, both made from rayon, pitch or PAN (polyacrylonitrile) precursor fibres, heated in an inert atmosphere of 1700°C to carbonize the fibres. Great relevance is also given to glass fibres, by which *GLARE* is composed for example. They are made on a basis of silica, whose pure form exists as a polymer; it does not present a real melting point but softens up to 1200°C, where it begins to degrade.
- b. *Properties of whiskers*: A whisker has a similar near-crystal-sized diameter as a fibre, but it is shorter and more stubby. It presents higher mechanical properties than a fibre compared to the same material in bulk form; this is possible thanks to the almost perfect alignment of crystals, deriving from the crystallization on a very small scale.
- c. *Properties of matrix materials*: Matrix is defined as a binder material used to bond together fibres (or whiskers), to take the form of a structural element that can carry the loads.

Matrix main functions are:

- Support of the fibres/whiskers
- Protection of fibres/whisker
- Stress transfer between broken fibres/whiskers

Although combined with fibres/whisker they have increased strength and stiffness compared to metals, matrix materials have a considerable lower density, stiffness and strength.

The materials used as matrix are polymers, metals, ceramics and carbon.

Polymers (poly= many, mer= unit or molecule) are of three different types (fig. 2.1):

- *Linear polymers*, which is a chain of mers;
- *Branched polymers*, which present a primary chain with other chains attached in three dimensions, like three branches;
- *Cross-linked polymers*, composed by a large number of three dimensional interconnected chains.

The latter present the major strength and stiffness because of their stronger internal structure, while linear polymers have the least strength and stiffness.

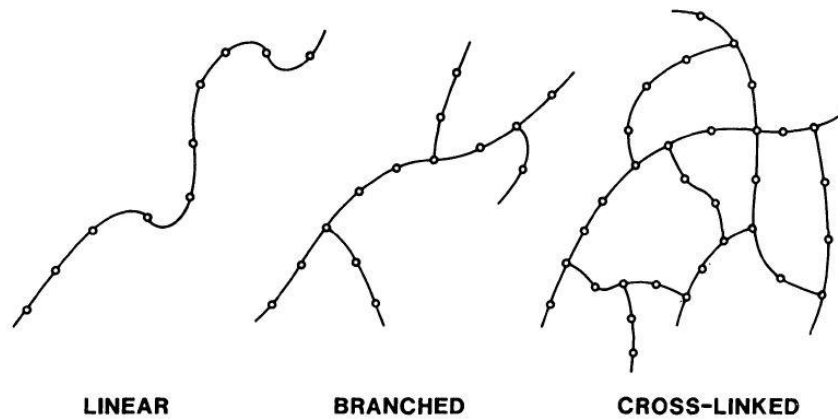


*Figure 2.1 - Types of polymers [1]*

Three main classes of cross-linked polymers can be considered: rubber, thermoplastic and thermoset.

The latter is the class of major interest in the present work. *Thermosets* are polymers chemically reacted until their molecules are irreversibly cross-linked in a three dimensional network. Thus, for example, once an epoxy is set, it cannot change its form anymore. They are usually stronger than *thermoplastic* materials because of their 3D form and so for this reason more conform to high temperature treatments. On the other hand they are more brittle and they cannot be recycled. Thermoset materials include epoxies, phenolics and polyimides. The firsts are the most interesting in relation to the present work because the material studied here is composed by it, as reported in the manufacturing chapter.

### 2.1.2 Laminate composite materials

A second type of composite materials is composed by layers of at least two different materials bonded together.

It is possible to distinguish three main types of laminate composites:

- *Bimetals*, formed by two different metals having significantly different coefficients of thermal expansion;
- *Clad metals*, obtained cladding or sheathing one metal to another, to achieve the best properties of both;
- *Laminated glass*, where the protection of one layer of material with another proposed with clad metals is extended to automotive safety glass: one layer of polyvinyl butryal is sandwiched between two layers of glass, which gives stiffness and protection from the scratches to the composite material;
- *Plastic-based laminates*: materials saturated with various plastics for a variety of purposes. They are made from kraft paper, resin and adhesives. Multiple layers of kraft paper are soaked in resin, then pressed together at high levels of temperature and pressure to form a single sheet. A protective urethane top coat, or wear coat is added to enhance strength and durability. Examples are materials sold under popular brand names like Formica® or WilsonArt®.

### 2.1.3 Particulate composite materials

A third type of composites is formed by particles of one or more materials suspended in a matrix of another material; both the particles and the matrix can be either metallic or non-metallic. Particles provide reinforcement to the matrix material thereby strengthening the material. The combination of particles and matrix can provide for very specific material properties.

The different configurations proposed are:

- Non-metallic particles in a non-metallic matrix
- Metallic particles in a non-metallic matrix
- Metallic particles in a metallic matrix
- Non-metallic particles in metallic matrix

A composite material of the first configuration is formed for example considering stones or gravel as the particles and cement as the matrix. Another example is given by the inclusion of conductive particles in a plastic which can produce plastics that are somewhat conductive. Glass reinforced plastics are used in many automotive applications; brakes are made of particulate composite, composed of carbon or ceramics particulates.

### 2.1.4 Combination of composite materials

Multiphase composite materials show several of the properties presented above for the various classes. For example a reinforced concrete is both particulate, because is composed by gravel in a cement paste binder, and fibrous, because of the steel reinforcement.

Moreover laminated fibre reinforced composites are a hybrid class, composed by layers of fibre-reinforced material bonded together with the fibre directions of each layer oriented in different directions, in order to guarantee strength and stiffness in various directions.

## 2.2 Material characterisation

### 2.2.1 Mechanical behaviour of composite materials

The most of the common engineering materials are both:

- *Homogeneous*, which means they present uniform properties, independently of the position in the body;
- *Isotropic*, i.e. properties are the same in every direction at a point of the body, independently from the orientation at that point.

In opposition, composite materials are both:

- *Inhomogeneous (heterogeneous)*, because they present non-uniform properties over the body, i.e. properties depend on the position in the body;
- *Non-isotropic*, which can result in being orthotropic, i.e. properties differ in three mutually perpendicular directions, in order to give three perpendicular planes of

symmetry, or being anisotropic, i.e. properties are different in all the directions at a point.

Because of their heterogeneous nature, composite materials are thus studied from two different points of view:

- *Micromechanical*, the interaction of the material is examined on a microscopic scale to determine the effects on composite properties.
- *Macromechanical*, the material is supposed to be homogeneous and the effects are considered only as averaged apparent macroscopic properties.

Anyway, composite material's mechanical behaviour is different from conventional materials due to their anisotropy or orthotropy. To explain the latter sentence it can be considered the single behaviour of each one of the following kinds of material:

- *Isotropic materials*: the application of normal stresses gives an extension in direction of the stresses, contraction in perpendicular direction and no shearing deformation; the application of shear stresses instead gives just a shearing deformation. For these reasons only two properties must be defined, i.e. the Young's modulus ( slope of the material's stress-strain curves) and the Poisson's ratio (negative ratio of lateral contraction strain to axial extensional strain).
- *Orthotropic materials*: the application of a normal stress in a principal material direction leads to the same behaviour described at the previous point. The extension in that direction has different magnitude from the extension in another principal direction; for this reason Young's moduli varies in the various principal directions. The contraction can be higher or lower compared with what described in the previous point, thus different Poisson's ratios are associated to different pairs of principal directions.

The application of a shear stress gives shearing deformation, which is independent from Young's modulus and Poisson ratio; so, being these parameters independent from other material properties, the shear modulus of an orthotropic material is independent from other material properties, unlike isotropic materials.

- *Anisotropic materials*: the application of normal stresses leads to the same behaviour visible when applying shear stresses, i.e. extension in the direction of the stress, contraction along the perpendicular direction and also shearing deformation. The "shear-extension coupling" is present in orthotropic materials too when subjected to normal stresses in a non-principal material direction.

### 2.2.2 Terminology of laminated fibre-reinforced composite materials

It is important to first introduce the right terminology used to described the type of composite materials studied in the present work. A main distinction has to be introduced between *lamina* and *laminate*.

A *lamina* is the basic building block of a *laminate*, consisting in a flat arrangement of unidirectional or woven fibres in a matrix. These two elements, the fibres and the matrix, represent respectively the principal reinforcing or load carrier and the support for fibres, necessary to protect them, distribute the loads and transmit loads between fibres. This latter aspect is very important when a fibre breaks; in this case the matrix redistributes the load thanks to the shearing stress present in the matrix, that resists the pulling out of broken fibres. The typical stress-strain behaviour classes which a lamina can exhibit is one of the four types displayed in figure 2.2.

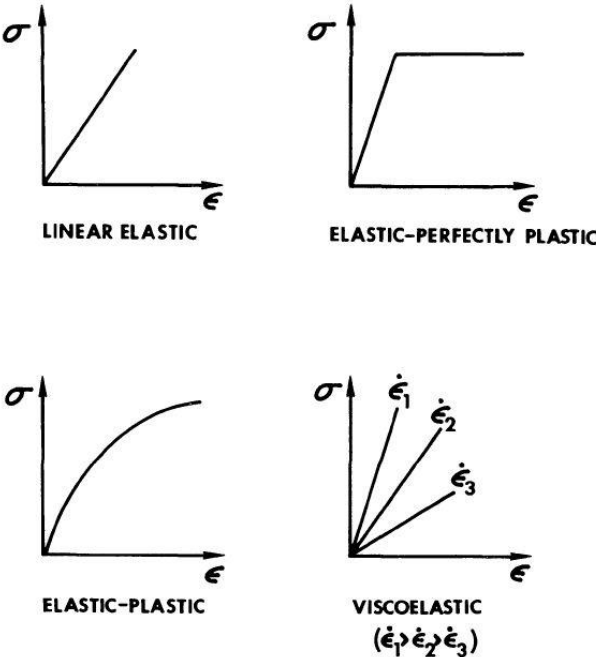


Figure 2.2 - Types of typical stress-strain behavior [1]

A *laminate* is a bonded pile of *laminae* with various orientations of the principal material directions. The layers are usually bonded together with the same matrix material of the individual *lamina*. Laminates can be composed of plates of different materials hybrid laminate (figure 2.3a) or plies of fibre-reinforced laminae (figure 2.3b). Its main propose is to tailor the direction dependence of strength and stiffness to match the loading environment of the structural element. The individual layers consist of high-modulus and high-strength fibres in a polymeric, ceramic or metallic matrix material. Depending upon the stacking sequence of the individual layers, the laminate may exhibit coupling between in-plane and out-of-plane response, like for example the bending-stretching coupling represented by the presence of curvature, developing as a result of in-plane loading.

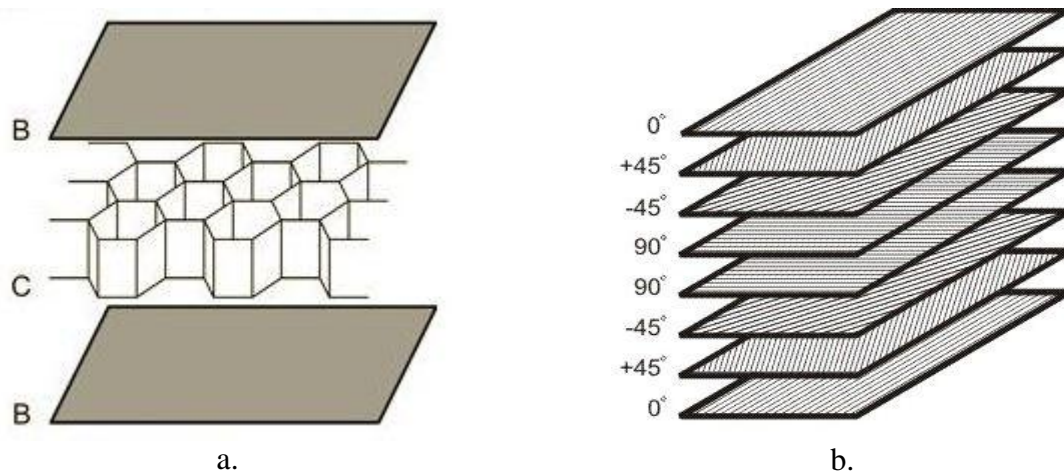


Figure 2.3 - Types of laminates

### 2.3 Laminate failure

The research on failure of composites and failure criteria is important. The most important point is the understanding of failure's physics. It has already been investigated extensively at *micromechanical* and *macromechanical* scale. In the first case, failure mechanisms vary with the type of loading and are closely related to the properties of constituents phases, reinforcement and interface. The micromechanical analysis are approximate with regard to global failure, even if they are accurate in predicting the local failure initiation at a critical point. A macromechanical approach to failure is thus necessary.

The study of the failure problem can be divided in two parts, the prediction of a single lamina failure and the prediction of first-ply-failure (*FPF*) within a multidirectional laminate and damage progression until ultimate failure of the laminate [3]. Within the latter category, which represents the one studied here, can be included the interlaminar fracture or delamination, intralaminar fracture or matrix cracking, matrix-fibre disbonding, fibre breaking (translaminar fracture) and fibre pull-out [4].

After presenting the different modes of loading, an introduction to the theories of adhesion and the different types of bonding between fibres and matrix is considered necessary to understand what happens in case of failure. The related sections follow the basic and linear explanation available in reference [5]. Then a summary of adhesive bonding between different *laminae*, disbonding mechanism and delamination propagation will be reported.

#### 2.3.1 Loading Modes

The three modes of loading are known as Mode I (*opening mode*), Mode II (*shear mode*), Mode III (*tearing mode*). Fracture mechanics concepts are the same for each mode (see 2.3.6). Figure 2.4 displays the representation of these three loading modes.

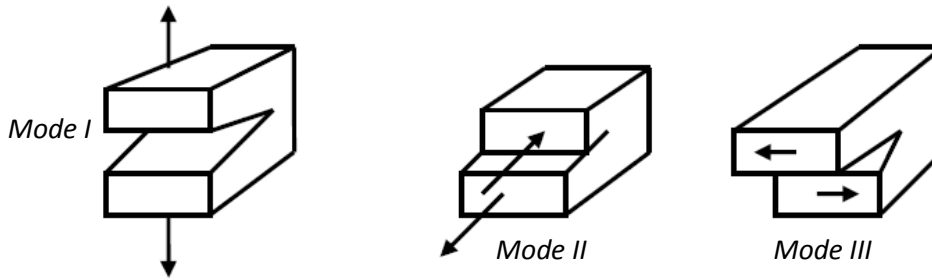


Figure 2.4 - Loading modes [4]

Each mode can be shortly described as [5]:

- I) Fracture mode in which delamination faces open away from each other and no relative crack face sliding occurs; the *Interlaminar Fracture Toughness (IFT)* is indicated by  $G_{IC}$ .
- II) Fracture mode in which the delamination faces slide over each other along the direction of delamination growth and no relative crack face opening occurs in the normal direction to the leading edge; the *IFT* is denoted by  $G_{IIc}$ .
- III) Fracture mode in which the delamination faces slide over each other in parallel to the leading edge.

Structures made of composites are often subjected to complex three dimensional load paths during service. In general, all three loading modes I, II and III, or a combination of them, can be present at the delamination front [6].

### 2.3.2 Theories of adhesion and nature of bonding

Each fibre-matrix system has a specific interface because the type of bonding depends on the morphological properties of the fibres and the diffusivity of elements in each constituent.

Adhesion can be obtained through different mechanisms, the most common of which are wetting and adsorption (molecular entanglement), electrostatic attraction, interdiffusion of elements, chemical reaction between groups A and B placed on different surfaces, chemical reaction following of forming new compounds and finally mechanical interlock.

Good wetting of fibres by matrix material during fabrication process is important to obtain a proper consolidation of composites, in particular for those based on polymer resins. For these materials is also remarkable the so called interdiffusion mechanism. Indeed if a thermodynamic equilibrium between the two constituents exists the bond can be performed by interdiffusion of atoms or molecules across the interface of the two surfaces.

The quality of the bond and its strength will depend on the number of molecules, their conformation and their motion, the amount of molecular entanglement and the strength of bonding between these molecules.

An example can be mentioned to understand the properties of the bonded materials, with regard to the goodness of the bonding, referred to the carbon fibre-epoxy matrix material. The average modulus of an interphase between the carbon fibres and the epoxy matrix is one quarter of that in the bulk material. This effect is however mitigated by the presence of a stiff fibre which compensates that of a soft interphase, through the increasing of the effective

modulus beyond that of the bulk around the fibre region. Undesirable effects are the formation of unwanted compounds. This can be avoided applying a diffusion barrier, i.e. a coat on the fibre; this solution is possible only having a good knowledge of the nature of the interaction in the interface region for that specific fibre-matrix system.

Bond quality at the fibre-matrix interface is measured in terms of various factors, for example interlaminar fracture toughness  $G_{Ic}$ , through a variety of test methods presented further in this report. Other tests also involve microcomposite structures, such as the single fibre compression test or the fibre pull out test, just to enunciate some. It must be noted that these tests on microcomposites give a large variation along the experimental data collected for identical fibre-matrix systems. This phenomenon can be due to lack of standardization in specimen manufacturing and preparation, loading methods and data reduction methods.

### *2.3.3 Adhesive bonding*

Adhesive bonding has become the preferred joining technique for many materials since it allows to make a better use of their mechanical properties; indeed technique traditionally used for metals as riveting or bolting have been proved to be damaging for mechanical properties of composite materials. Adhesive bonding has advantages in joining fibre reinforced composites since it avoids the cutting of fibres as well as holes and stress concentration deriving from them. These benefits join the major reason which makes composites very common for aerospace application, i.e. their remarkable weight saving compared with traditional metal materials.

Some aspects of the adhesive bonding process must be underlined to better understand it in its completeness. First of all great importance during the bonding process has to be given to surface treatments, which has been demonstrate can improve bond performance by eliminating weak boundary layers at the surface (contaminants, oxidized layers, low molecular weight species), by improving wetting of low energy surfaces or by increasing surfaces' roughness, which definitely improves mechanical interlocking and increases bondable area [7].

Treating the surfaces the chemistry and morphology of a surface layer can be modified without affecting the bulk properties of the material. But attention has to be paid during these processes because they can cause also defects on the material. Composites have very smooth and moulded surfaces because of the polymer matrix material, so surface energies tend to be low (in particular for thermoplastic matrix), which turns more difficult to wet the surface by an adhesive. Some treatments can also cause delamination defects below the surface or damage the brittle fibres, affecting so the mechanical properties of the material.

A common problem in composites bonding is represented by the great number of contaminants present on a surface, which lead to a weak boundary layer in the bond. Examples of these contaminants are silicones from release agent and bagging materials, machining oils etc.

Many different treatments can be found in literature, suitable both for composite material and metals or plastics. The most famous are the alumina gritblast, sodablast, detergent cleaning, peel ply and solvent cleaning. These two last methods are the most interesting in relation to the present thesis.

The peel ply is a mechanical treatment developed to store the material keeping its surfaces clean. It consists in a layer of nylon or polyester incorporated in the surface of the composite during its manufacture. It is then stripped off the surface just before the bonding. The benefits of this treatment has been proved in an approximately doubled surface energy for a carbon/epoxy composite [7]. The main problem with peel ply treatment is the cross transfer of contamination from the ply to the composite, in particular silicones, from which sometimes this treatment is not able to protect the material.

The solvent wipe is the simplest method to remove contaminants from composites surfaces. Its effectiveness depends on solvent used and type of contaminants; it can happen that the process just spreads the contamination over the surface. To avoid cross transfer of contamination fresh solvent and wipes can be adopted.

In adhesive bonding the temperatures adopted during the process are relatively low; even if thermosetting polymers present the good feature of being usually fully bonded, voids are often present at the bonding interface. These voids are filled by gas residues from the adjacent polymer, which may form gas bubbles as result. This phenomenon makes the material vulnerable since the bubbles cannot often be removed even after the curing process of the polymer, degrading in this way the mechanical properties of the material in terms of interlaminar shear and compression strength. Studies have demonstrated that during certain specific process condition these bubbles are led to shrink and explode, dispersing the gas contained into bulk form molecularly. Empirical methods have been carried on in order to reduce this phenomenon and optimize the bonding process, without finding an universal approach for all kind of thermosetting polymers; the complex nature of the bubbles formation involves in fact different parameters, such as temperature, pressure and time. An analytical approach to the problem has been found in order to predict and control the bubbles formation and successive deformation; since it is not an interest of this thesis to expose the solution to this problem, in reference [8] can be consulted the whole procedure.

#### 2.3.4 Disbonding

A disbond indicates “an area of separation within or between plies in a laminate or within a bonded joint, which can be caused by improper adhesion during processing, contamination or damaging interlaminar stresses” [9].

The disbonding mechanism of failure can assume two different aspects:

- *Cohesive failure*: represents the inability of the adhesive to resist to internal separation; the adhesive remains attached to both surfaces but cannot hold them together. In other words disbond growths within the adhesive.
- *Adhesive failure*: represents the inability of the adhesive to stick to a surface; it is not able to bind the surfaces together and so separates from the substrate. In other words disbond growths at or near the adherent-adhesive interface.

It has been experienced [10] during both static and fatigue tests on Double Cantilever Beam specimens bonded with a brittle adhesive (*FM 400*) that the disbond growths either in a cohesive or adhesive manner. Indeed once the disbond growths in an adhesive manner, then it keeps going on in the same manner until it represents the weakest link of the specimen.

Nevertheless if it starts in a cohesive manner it can possibly change to an adhesive manner of failure. The reason of this transition can be researched in the weak bond represented by the carrier and the adhesive, whose presence can so weaken the joint. For a ductile adhesive (*FM 300*) instead the specimens show cohesive, adhesive and mixed behaviour at the same time, resulting rather irregular.

### 2.3.5 Delamination

This mode of failure (*failure mechanism*), is considered the weakest one in laminated composites, and besides the most prevalent life-limiting crack growth mode. It consists of layer separation, causing a consistent loss in mechanical properties of the laminated material. Delamination can be introduced during manufacturing or caused by service conditions. Indeed the generally low interlaminar strength leads events such as cyclic stress or impact to give life to this failure mechanism, together with eccentricities along the structural load path or discontinuities in the structures themselves, like free edges, notches, ply terminations/drops, bonded or co-cured joints. In addition to mechanical loads, interlaminar stresses can be introduced by moisture and temperature, due to residual thermal stresses after the cooling process subsequent to the processing temperatures, or to residual stresses caused by the moisture absorption or also to the moisture through the thickness of the laminate [5].

For all just exposed delamination is one of the major problems for *FRP* composites, because it affects seriously the structural performance of the composite materials, causing a loss in the overall performance, in particular where geometrical or material discontinuities are present [4].

The delamination can cause significant reduction in structural integrity, i.e. loss of strength and stiffness, local stress concentration and local instability, that can be followed by catastrophic failure, without warning in advance because delamination is often invisible from the surface. It can also introduce a redistribution of stresses which leads to gross failure, causing so indirectly final failure of the material. For this reason in aerospace industries the past applications of composite materials were limited to secondary structural components with load path well defined [5].

### 2.3.6 Linear Elastic Fracture Mechanics approach

An accepted approach to the characterization of delamination growth in composites is the application of Linear Elastic Fracture Mechanics (*LEFM*) theory, which gives the possibility to deduce the value of the Strain Energy Release Rate (*SERR*)  $G$  and compare it to the critical value  $G_{Ic}$  and  $G_{IIc}$ , also referred as Interlaminar Fracture Toughness (*IFT*). Note that this refers just to mode I or mode II, but not to mixed modes. *IFT* is defined as the critical value of energy needed to create a unit of an interlaminar crack [6]. The value of  $G$  depends on the loadings, the geometry of the body and the constrains, while the value of  $G_c$  is a property of the material.

This approach is the one selected to carry on the present work. It can be resume as an approach to fracture analysis that assumes the material behaviour as elastic at regions away from the crack, except for a small non-elastic region ahead the crack tip. The fracture

resistance is expressed in terms of strain energy release rate  $G$ , in a manner analogous to crack growth in terms of stress intensity factor  $K$  for isotropic and homogeneous materials, this primarily because it is difficult to obtain the local crack tip stresses used to determine  $K$  for an inhomogeneous composite material; indeed the stress field around the crack tip often shows an oscillatory behaviour. Using  $G$  it is possible to avoid the need of crack tip stresses. In this way, the analogy leads to express the delamination growth rate as a Paris - type relation [11]:

$$\frac{da}{dN} = C(G_{eff})^n$$

Under cyclic loading more attention has to be given to the formulation of  $G_{eff}$ . The most common approaches utilize two formulations to replace  $G_{eff}$ , i.e.  $G_{max}$  and  $\Delta G = G_{max} - G_{min}$ . A third approach based on the *LEFM* has been studied and it led to define  $G_{eff}$  as  $\Delta G_{\sqrt{}} = (\sqrt{G_{max}} - \sqrt{G_{min}})^2$ .

This topic is not any longer explained here because for its deep comprehension a section is presented in *Chapter 4*.

## 2.4 Manufacturing process introduction

A general view of the manufacturing processes is here introduced; the manufacturing process carried on in the present work will be then presented in the next chapter.

The initial form of the constituents of a composite material can be variable. Fibres can be obtained commercially both individually and as roving, a continuous bundled but not twisted group of fibres. The matrix is a resinous material (for example epoxy), which is coated or saturated with the fibres. This process is known as preimpregnation, and the preimpregnated product obtained is often referred as *prepreg*. The material tested in the present research belongs to this latter group of composites. A prepreg consists of a reinforcement material preimpregnated with a resin matrix in controlled quantities. The resin is partially cured to a B-stage, and in this form is supplied to the fabricator, who lays up the finished part and completes the cure with heat and pressure. The required heat and pressure will vary with the resin system and the intended application [12].

The advantages of prepregs versus wet layup are to be resumed as:

- Low void content
- Control of fibre volume fraction
- Control of laminate thickness
- Lower labour cost
- Better quality and conformity
- Clean process

### 2.4.1 Layup processes

It is possible to distinguish different kind of layup processes for laminated fibre-reinforced composites. Those of principal interest are resumed in:

a. *Winding and laying:*

*a.1 Filament winding:* consists of passing a fibre through a liquid resin and winding it on a mandrel, with different orientations, in order to yield strength and stiffness in all of these directions.

*a.2 Tape laying/wrapping:* a tape of prepreg fibres is held together by a removable backing material, giving them in this way the desired shape and orientation.

*a.3 Cloth winding/wrapping:* this process is more inflexible and inefficient than the previous two presented above, because of the less efficient bidirectional character of fibres on the cloth.

b. *Moulding:* deposition of prepreg fibres in layers, by hand or automated. These layers are compressed under elevated temperatures to form the final laminate in a press. Three main types are listed:

*b.1 Resin transfer moulding (RTM):* dry fibres or textile sheets and solid resin are heated and formed in a mould or other tool.

*b.2 Sheet moulding compound (SMC):* randomly oriented and chopped fibres are stacked in a matrix of resin and filler.

*b.3 Pultrusion:* incoming unidirectional material is pulled through the pultrusion die.

To process prepreg materials several techniques are used:

- Vacuum bag moulding
- Autoclave moulding
- Press moulding
- Pressure bag moulding
- Thermal expansion moulding
- Tube rolling

### 2.4.2 Curing

The curing process leads to the solidification of polymer matrix materials.

Metal matrix materials are simply heated and cooled around the fibres to solidify.

Ceramic and carbon matrix materials are vapour deposited mixed in a slurry with fibres, and hardened; the carbon matrix is also subjected to repeated liquid infiltration followed by carbonization.

Thermoset-matrix materials see the addition of heat as a catalyst to speed the natural chemical reaction of polymerization. The higher is the temperature the shorter is the time to complete the process. A certain pressure is necessary to consolidate the fibre-matrix product.

A typical curing cycle starts gradually increasing the temperature under vacuum conditions in order to drive off the volatiles and the water (vapour). Then the temperature continues to increase until the maximum cure cycle temperature is reached; the latter is then held for the time needed to develop a high degree of cross-linking along with the right pressure to consolidate the laminae.

A temperature versus time general plot can be seen in the figure 2.5.

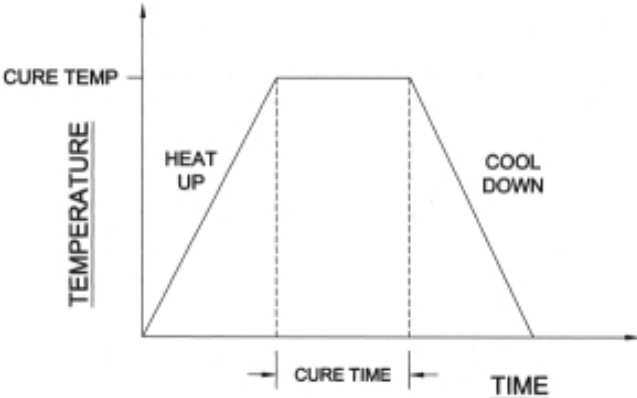


Figure 2.5 - General cure cycle [12]

Curing can be performed in several devices like heated mould, hot press, and autoclave [1]. The last device is the one utilized during the manufacturing of the specimens used for the tests performed in the present work.

## 3. Specimens Manufacturing

The material utilized for the present research is a thermoset composite material, the unidirectional (UD) carbon/epoxy prepreg *M30SC/TD120* produced by Delta-Tech.

The specimens used in the present work were manufactured in the *DASM Lab* at *TU Delft*. They were produced using the vacuum bag process presented later in the current chapter.

The configuration considered for all the tests is a symmetrical one, in particular  $[0^\circ/90^\circ/\pm 45^\circ/\pm 45^\circ/90^\circ/0^\circ]$ . Such a layup, being symmetric and balanced, avoids bending effects and extensional coupling. It also avoids in-plane coupling and distortions from shearing modes due to axial loads. The selected configuration is able to handle different types of load; in fact in addition to the ones in fibre  $0^\circ$  direction, the plies in  $90^\circ$  direction are able to handle transverse loadings while the ones with  $\pm 45^\circ$  orientation carry the shear loads.

### 3.1 Material Properties

The properties of the mentioned *M30SC* fibres are resumed in table 3.1.

Tensile Strength		Tensile Modulus		Elongation	Yield	Density	Standard Pool Size
ksi	MPa	Msi	GPa	%	g/1000m	g/cm <sup>3</sup>	kg
796	5,490	42.7	294	1.9	760	1.73	4.0

Table 3.1 - *M30SC* fibres properties

Concerning the matrix, for the used *DT120* epoxy matrix Delta-Tech provides its datasheet [13] containing the properties resumed in table 3.2.

<b>Chemical nature</b>	Toughened thermosetting epoxy
<b>Cure temperature</b>	110-145° C
<b>Gel Time</b>	8-13 min @ 120° C
<b>Tg after cure</b>	115-120° C after 90 min @ 120° C
<b>Viscosity</b>	High
<b>Transparency</b>	Fair
<b>Shelf life</b>	4 weeks @ 20° C 12 months @ -18° C
<b>Colour stability respect UV exposure</b>	Very good
<b>Adhesion on honeycomb core</b>	Very good

Table 3.2 - *DT120* epoxy properties [13]

### 3.2 Mode I Tests – DCB specimens

Mode I tests, both static and fatigue, were performed on two different qualities of the present material: the first one is referred as *good quality* while the second one as *poor quality*. *Good* indicates that the material doesn't present any defect both macroscopically and microscopically, so all the features required are retained to be good. It was obtained following

the exact instructions for the manufacturing process given by the manufacturer. In opposition the term *poor* indicates a material presenting several defects and anomalies, like voids in the adhesive epoxy used to bond the laminae. The material of this second quality was obtained hypothesizing a different process from the one suggested by the manufacturer.

### 3.2.1 Good quality material

Double Cantilever Beam (*DCB*) specimens were used to test the material under static and fatigue mode I loading. A *DCB* specimen is an uniform thickness laminated specimen of rectangular shape. A typical *DCB* specimen is shown in fig.3.1. The reasons of this choice will be further illustrated in the appropriate chapters of this report.

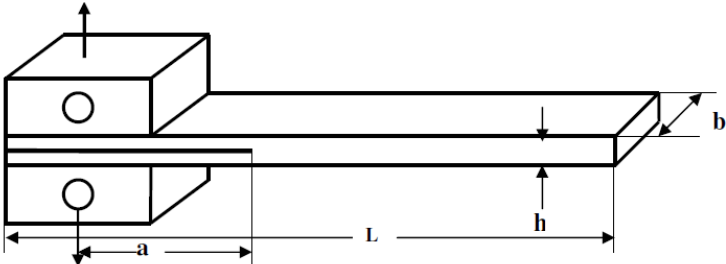
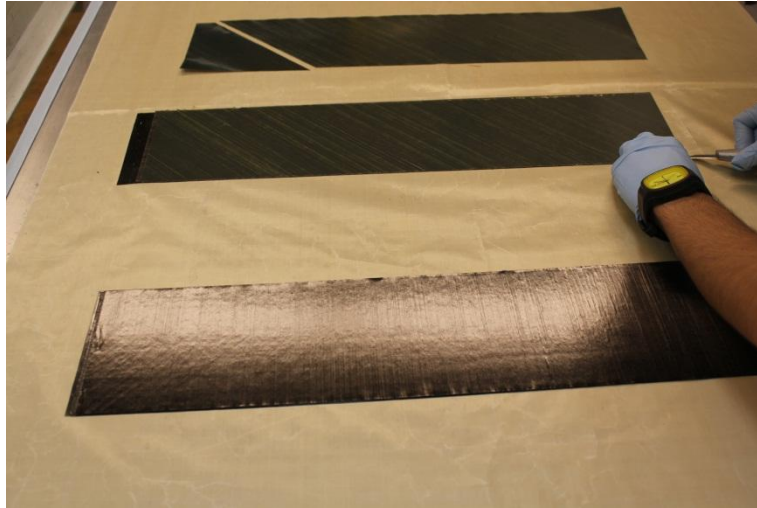


Figure 3.1 - Double Cantilever Beam specimen [4]

First of all the roll of the material (figure 3.2) was extracted from the fridge and left twelve hours in the laminating room to reach the room temperature. Then the necessary number of plies was cut from the roll. The plies were disposed on a large table in order to obtain the wanted symmetrical configuration (figure 3.3); the table was previously polished with a release agent, then covered with a Teflon film.



Figure 3.2 - M30SC/TD120 roll



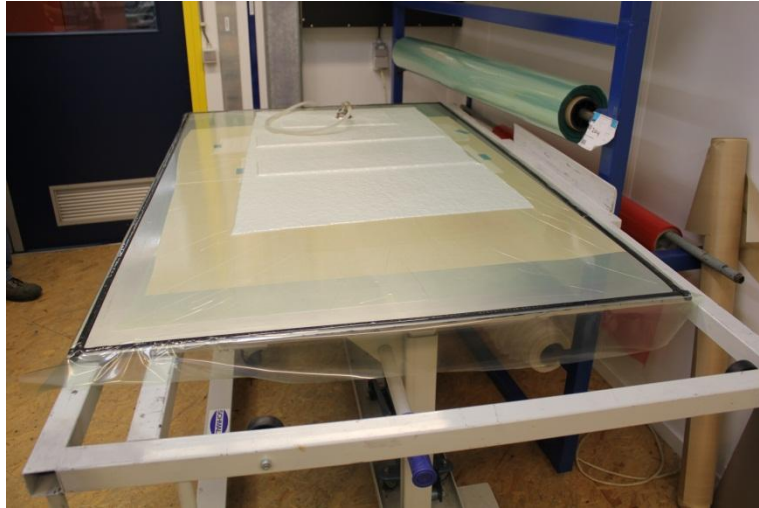
*Figure 3.3 - Mode I plates preparation*

The correct configuration was achieved increasing the number of plies to 16 in each lamina, from the 8 used initially, because more thickness was necessary to perform the tests, as it will be explained later in the present report.

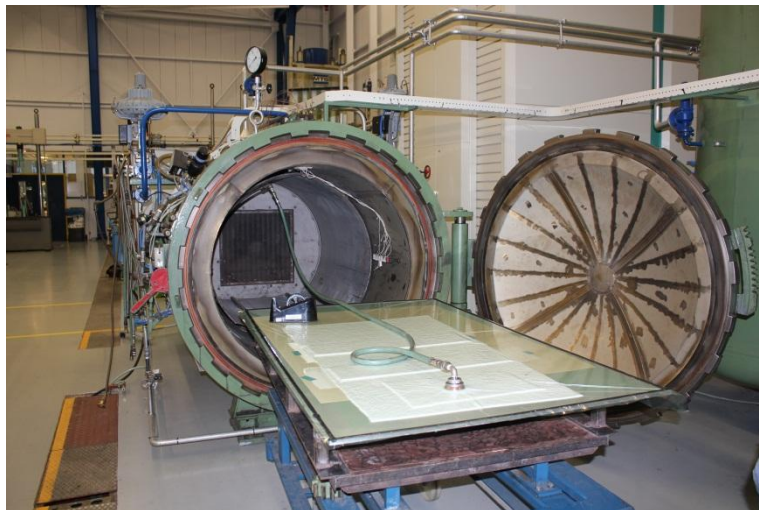
Each lamina was laid down separately on the Teflon film and covered on the top with an aluminium sheet (*caul plate*) of the same size and shape, and lastly a second Teflon film. This operations led to obtain a very smooth surface on the top of the lamina, and a row one on the bottom, which it is the one successively used to bond the laminae. A carbon cotton tissue was disposed to coat all the mentioned items; due to its pierced nature it fits a vacuum coupling which communicates with the outside through a hole in the ultimate film, the one used to cover the whole content of the table. This last nylon film was sealed to the table with a special insulating black tape, situated all around the edges, creating so the final vacuum bag. The vacuum coupling was then connected to a vacuum pump to primarily extract the air inside the system (figure 3.4).

The table was then conducted to the autoclave (*Autoclave Scholtz*), were it was again connected to the vacuum system. The first cure cycle was so performed at 6 bar of pressure as recommended by the manufacturer [13]; in order to obtain the *good quality* plate (fig. 3.5) the cycle was set as following:

- heating @+2°C/min from RT to 120°C
- constant cure for 90 min @120°C
- cooling @-4°C/min to 60°C

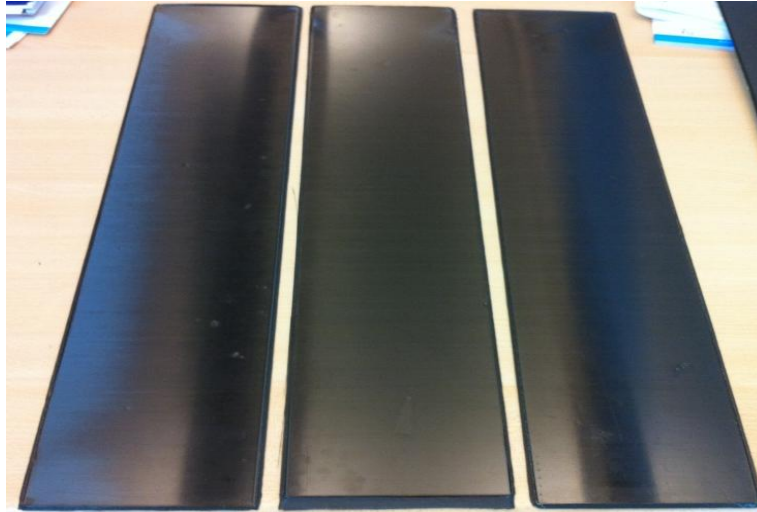


*Figure 3.4 - Vacuum bag*



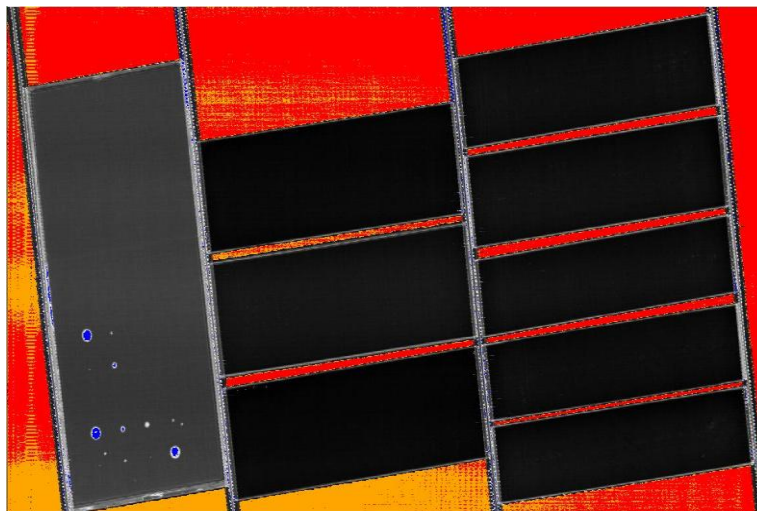
*Figure 3.5 - Autoclave for cure cycle*

Fig. 3.6 shows the final products obtained after the first curing cycle. It can be observed the perfect smoothness lent by the *caul plate* to the external surface of the plate, resulting in a bright lack look.



*Figure 3.6 - Laminae after first cure cycle*

After curing the plates were subjected to a ultrasonic *C-Scan* inspection, in order to verify accurately their quality. This technique represents a non-destructive inspection in which a short pulse of ultrasonic energy is incident on samples. Measurement of the transmitted pulse indicates the samples' attenuation of the incident pulse. The attenuation of the pulse is influenced by voids, delaminations, state of resin cure, the fibre volume fraction, the condition of the fibre/matrix interface and any foreign inclusions present, giving in this way a response about the quality of the samples. Fig . 3.7 shows the results; the *DCB* specimens plates were scanned together with the plates produced to obtain the specimens for the other tests described in the next paragraphs.



*Figure 3.7 - Good quality C-scan inspection results after first cure cycle*

Once received the confirmation about the good quality of the plates, they were bonded together in a second cure cycle, to obtain the final plate from where the tested specimens were cut.

The bonding process was realized using an epoxy adhesive film *FM94K*, produced by Cytec

Industries and distributed in rolls, from where was cut as done for the prepreg layers. The features of the adhesive are summarized in table 3.3 [14].

Adhesive bonding has become the primary method because of its advantages, such as the lower structural weight and the improved damage tolerance, in addition to its lower fabrication cost [2]. In particular *FM 94K* adhesive exhibits optimum elongation, toughness and shear strength properties, both in metal and composites bonding.

<b>Nominal thickness</b>	0,15 – 0,18 – 0,25 – 0,30 mm
<b>Colour</b>	Green
<b>Carrier</b>	Polyester knit

Table 3.3 - *FM94K* adhesive properties [14]

During this second cure cycle it was also inserted a Teflon film (13  $\mu\text{m}$ ) at one edge of the plate at the midplane, as crack initiator, in order to have a pre-crack of about 63 mm in each specimen.

It is not a propose of this thesis to discuss about the different methods of precracking a sample, such as insert films, wedge precracks and so on; but the choice made here can be easily justified explaining that an insert film gives an advantage in measuring the  $G_{Ic}$  since it forms an identical straight crack front, at least macroscopically as it will be discussed hereafter. Moreover, the formed crack front is independent on the loading history, which is an advantage for material systems with an increasing curve with the crack length since the value of  $G_{Ic}$  measured from a precrack is always higher than one measured from an insert film, and the difference between the two is a function of the crack length and the method used to precrack the sample [6].

The cycle performed in autoclave is again the one suggested by the manufacturer:

- heating at 1.7 – 2.8°C/min until 121°C;
- 2.8 bar of pressure;
- 121°C $\pm$ 3°C constant for 60 min.

Once the second cure cycle was completed the plates were scanned again; in fig. 3.8 can be seen the resultant picture, in which it is possible to distinguish the insert film giving the initial pre-crack in plates for mode I (first on the right) and mode II three-point bending tests, presented in the next paragraph.

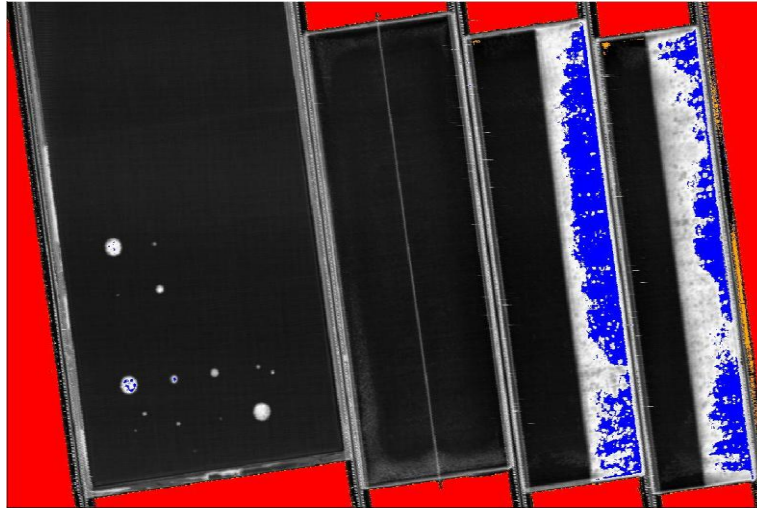


Figure 3.8 - Good quality C-scan inspection results after second cure cycle

To understand the planned use of the specimens' plate the preliminary sketch of the specimen and the plate can be seen in figures 3.9 - 3.10, realised in accordance with the *ASTM* standard procedures, as will be described successively.

The specimens whose name is written in red are those used for the quasi-static tests, while the ones in yellow are those for the fatigue tests. The purpose was to utilize specimens cut from different positions along the plate, in way of verifying that the quality of the plate is the same in each region of it, as suggested by the *C-Scan* results. The last *DCB* specimen tested was instead cut, with the required dimensions and sizes, from the mode II plate for *ENF* test; for this reason it has been denoted as E2.

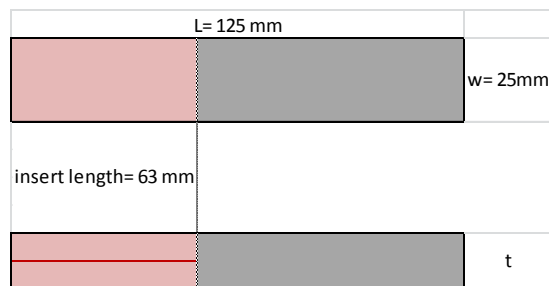


Figure 3.9 - Double Cantilever Beam specimen dimension

	<b>R1</b>	Specimen Width, 25 mm	Total Specimen Number, 20
	<b>R2</b>	Total Plate Width, 600 mm	
	<b>R3</b>		
	R4		
	<b>R5</b>		
	<b>R6</b>		
	R7		
	<b>R8</b>		
	R9		
	R10		
	<b>L1</b>		
	L2		
	<b>L3</b>		
	<b>L4</b>		
	L5		
	L6		
	L7		
	L8		
	L9		
	L10		
Insert Film, 63 mm			
Specimen Length, 125 mm			
Total Plate Length, 140 mm	75 mm Insert Film		
	6.5 mm specimen + margins		

Figure 3.10 – Good quality Double Cantilever Beam plate layout

Aside, a mention for the total thickness ( $2h$ ) of the specimens. During the first cure cycle the presence of the caul plate forced a certain quantity of material from the edges to come out. This resulted in a change of thickness along the specimen length. In particular the thickness is constant to the value of 5 mm for the region along which the delamination propagates, while decreases to 4,2 mm at the edge of the specimen (fig. 3.12). The change in thickness was thus accepted, since it did not affect the propagation region. A solution to avoid this situation could have been to manufacture a plate larger than the caul plate, which instead had the right dimensions, in order to cut the come out material and use just the constant thickness region of the plate below the caul plate.

Finally, can be highlighted the difference between the surfaces of the specimens, obtained thanks to the process described. Indeed, as previously described, in the first cure cycle the employment of a Teflon film beneath and the caul plate over the plate, provided a very smooth surface on the top (fig. 3.6) and a coarse one on the bottom. The caul plate suggested

by the producer in the data sheet of the material is an aluminium sheet of the same size and shape of the material which has to cover, laid in immediate contact with it to provide a smooth surface and to transmit the normal pressure during the autoclave cycle, even if this prejudices the specimen thickness as just exposed.

The other surface assumed the Teflon film shape; this solution in particular permitted to perform a better bonding between the two plates in the second cure cycle, since the adhesive film fits more accurately on a rough surface.

After bonding, the plates were accurately cut using two different types of machines, the *Carat Wet diamond* machine first and then the *Unitom Cutting* machine (fig. 3.11).

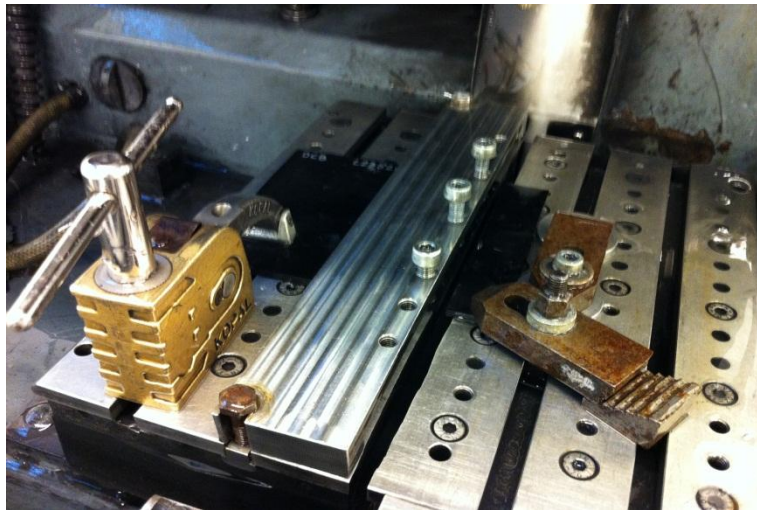


Figure 3.11 - Cut process, *Unitom* machine

Each specimen has been then marked to be identified; the best of them were chosen to be employed in the mode I tests. They were first superficially sanded with 240 grit sandpaper at the pre-cracked edge, then wiped clean with a solvent and bonded to the load blocks with the glue previously prepared (*3M 9193*). The load blocks were cured then in the oven (*Heraeus 0913*) with a cycle of two hours at 66°C of temperature. Lastly the edges were scratched again with sandpaper to eliminate the redundant glue, painted with corrector fluid and completed with a thin strip of graph paper, used as measurement scale to study the delamination length (see section 4.1.1).

The final *DCB* specimen ready to be tested, already anticipated in fig. 3.1, can be seen in fig. 3.12.

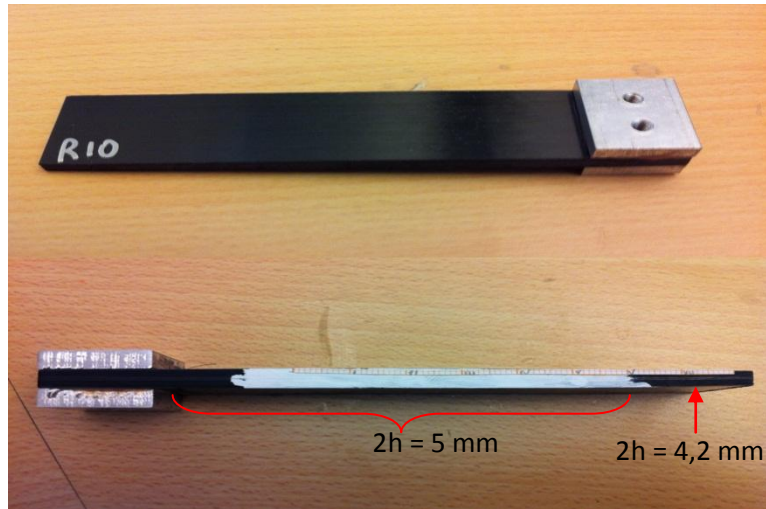


Figure 3.12 - DCB specimen ready to be tested

### 3.2.2 Poor quality material

As anticipated before the *poor quality* material was obtained using a different process from the one proposed by the manufacturer. In particular the process differs from the one just presented for the *good quality* plate just in the cycle used for the second cure. The adhesive bonding was performed using the *Heraeus 0914* oven instead of the autoclave; the propose was to avoid the use of a vacuum bag in the way to preserve the material from the leakage of the air bubbles which takes place when the cure is carried out in a vacuum bag. In this way the quality of the material was supposed to be inferior since the presence of voids is the first indication of structural imperfections, easily identifiable with the *C-scan* inspection. The temperature and the heating rate employed were however those suggested and so for the duration time, being retained these factors not influent for the wanted goal.

The quality of each lamina was again perfect, as demonstrated by figure 3.13 which shows the plates during the *C-scan* inspection.

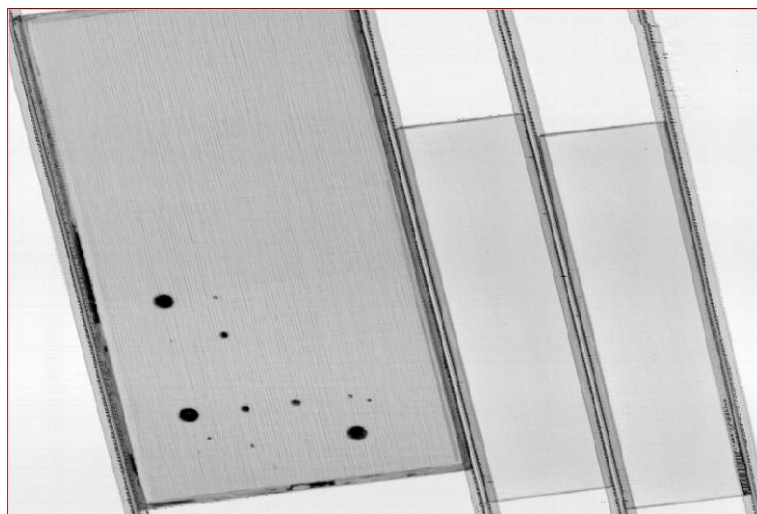


Figure 3.13 - Poor quality C-scan inspection results after first cure cycle

Figure 3.14 shows the *C-scan* results after the bonding through the “modified” cure cycle. As was predicted the scansion evidenced the defects present along the laminate. The extended red region confirms the presence of voids between the bonding surfaces, which can be related for example to ongoing delamination. The material presented so all the characteristic to be defined of *poor quality*.

Finally figure 3.15 shows the planned use of the *poor quality* plate, showing in red specimens used for static test and in yellow the ones for fatigue test.

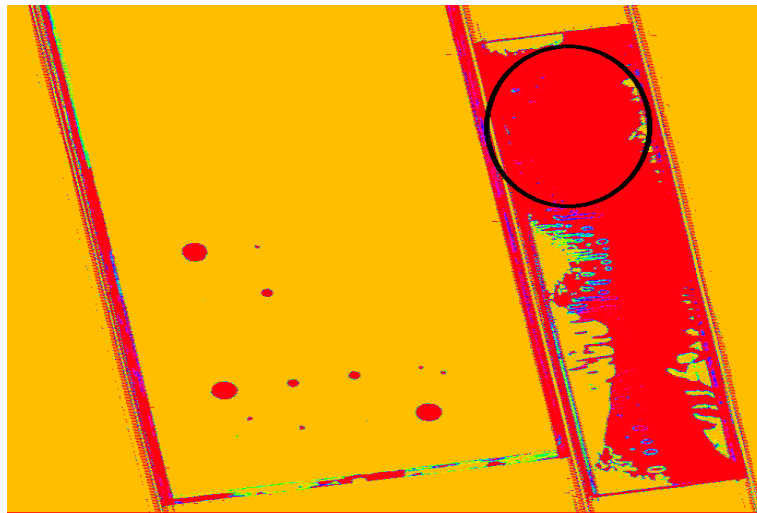


Figure 3.14 – Good quality C-scan inspection results after second cure cycle

Due to a problem during the cutting process the specimens resulted shorter than what required in the *ASTM* procedure. This was considered not affecting the results, since the region for the delamination propagation was enough long as the standard procedure requires (50 mm for quasi-static test).

The poorness of the plate was indeed confirmed during the cutting process. The last region of the plate corresponding to the specimens from S7 to S10 came up to be almost unbonded; the specimens separated again in the two laminae, revealing that the adhesive was intact and so it did not manage to bond the two surfaces (fig. 3.16). Comparing the sketch of the plate shown in figure 3.15 and the results of the *C-scan* inspection, it can be noted that the region in question matches with the region circled in black in figure 3.14, where the delamination appears to be more consistent than anywhere else, since it goes from one edge to the other along the width of the plate.

According to this revelation the mentioned part of the plate was considered not apt to be tested.

	D1	Specimen Width, 25 mm	Total Specimen Number, 20
	D2	Total Plate Width, 600 mm	
	D3		
	D4		
	D5		
	D6		
	D7		
	D8		
	D9		
	D10		
	S1		
	S2		
	S3		
	S4		
	S5		
	S6		
	S7		
	S8		
	S9		
	S10		
Insert Film, 63 mm			
Specimen Length, 125 mm			
Total Plate Length, 140 mm	75 mm Insert Film		
	6.5 mm specimen + margins		

Figure 3.15 - Poor quality Double Cantilever Beam plate layout

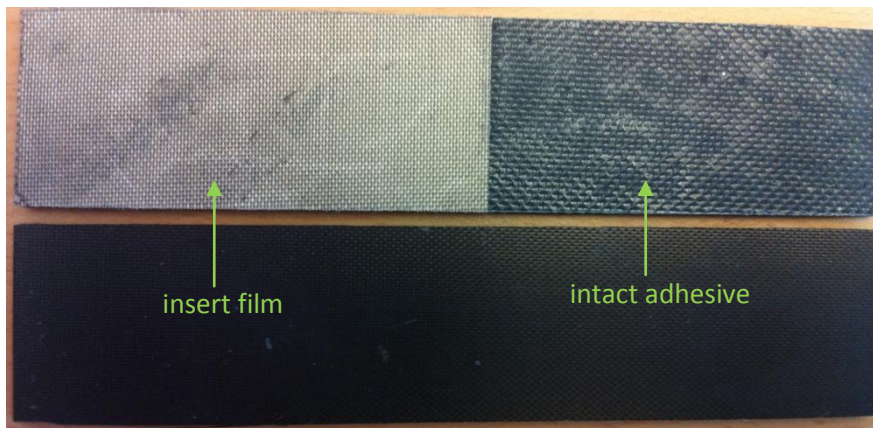


Figure 3.16 - Poor quality DCB specimen separated while cutting

### 3.3 Mode II tests

Tests for mode II are not regulated by standard procedure methods as it happens for mode I tests. Indeed even if a large variety of tests on different kinds of specimens have been performed, an international consensus has not been reached [15].

The present research identified two different kind of tests to determine the interlaminar fracture toughness for mode II loading. The first one is based on the most used type of specimen for this propose, the End Notched Flexure (*ENF*) specimen. The second one consists in a new model to study the delamination growth, based on Central Cut Ply (*CCP*) specimens.

In the following two paragraphs the manufacturing process of these two different samples will be described.

#### 3.3.1 *ENF* specimens

Although the *ENF* specimens are the most used to characterize the mode II interlaminar toughness, they are not considered the standard ones yet. This is due to several factors; the first is that *ENF* test just lead to find initiation values but not the resistance curve, because generally they show an unstable behaviour. A second motivation is given by the presence of friction contributions [4].

A typical example of *ENF* specimen is shown in fig. 3.17.

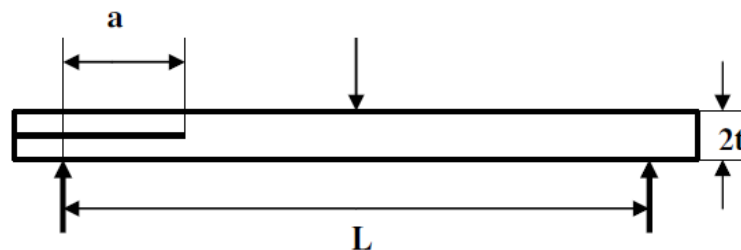


Figure 3.17 - End-Notched Flexure specimen [4]

The plates were manufactured in a way completely similar with that used for manufacturing *DCB* specimens (section 3.2). Two laminae were cured in a first cycle and then cured once again to be bonded together using the same *FM 94* adhesive and the same Teflon insert film at the midplane as delamination starter; its length in this case is suggested to be of 65 mm.

The dimension suggested for this kind of specimens are different; in particular the length is 160 mm, while the width is still the same (25 mm) of a *DCB* specimen, as well as the thickness (3-5 mm). Since the configuration is the same reported previously, once again 16 layers have been used to reach the wanted thickness.

In the fig. 3.7-3.8 are presented the scan results respectively between the two curing cycles and after the second one; moreover they help to visualize the mentioned similarity between *DCB* and *ENF* plates.

The preliminary plan for the mode II *ENF* plate is shown in fig. 3.18.

		Specimen Width, 10 mm	Total Specimen Number, ca. 55	
		Total Plate Width, 600 mm		
Insert Film, 65 mm				
Specimen Length, 160 mm				
Total Plate Length, 165 mm		75 mm insert film		
		95 mm specimen + cut margins		

Figure 3.18 - End-Notched Flexure plate layout

### 3.3.2 CCP specimens

The third type of specimens consists of three bonded laminae, where the middle one presents an interruption (figure 3.19). They have been prepared manufacturing three different laminae first. The outer laminae have been designed to be 1 mm thick, which means that 8 layers have been used. Between them a central plate of 2 mm of thickness (16 layers) has been cut in the middle, in order to obtain the wanted specimens with the interrupted central plies. The distance between this central plies along the fibres direction is about 2 mm. In fig. 3.8 this is easily visible. The interruption has been obtained during the second cure cycle inserting a 20 mm long aluminium stick for each edge, 2 mm thick and wide. To avoid the pressure to bend them, two smaller pieces of the same aluminium stick have been inserted below them. What just described can be better understood through fig. 3.20.

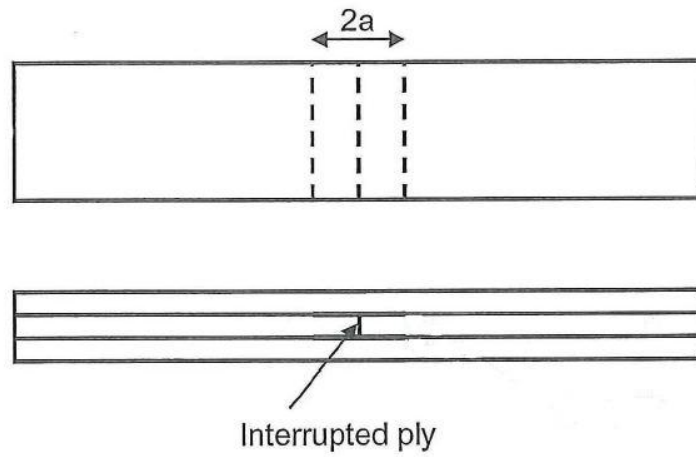


Figure 3.19 - Central Cut Ply specimen

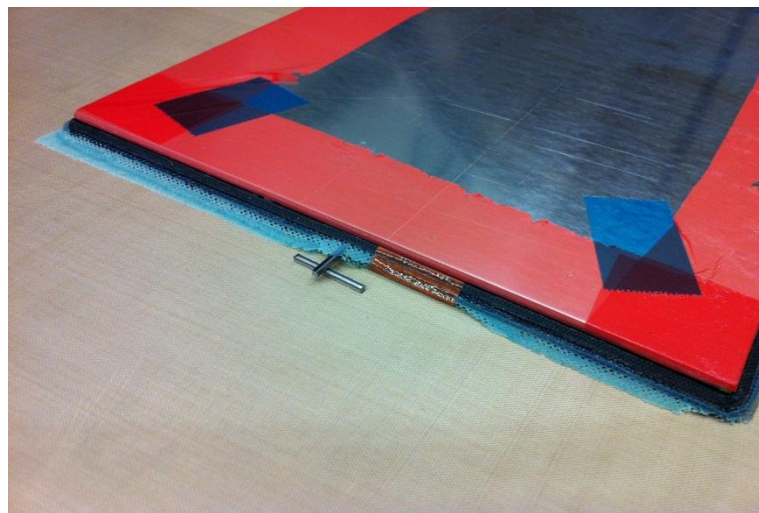


Figure 3.20 - CCP plate solution adopted against cure cycle pressure

This interruption is without any doubt the most sensible point, because it is the point where the onset and growth of four different delaminations takes place (fig. 3.21).

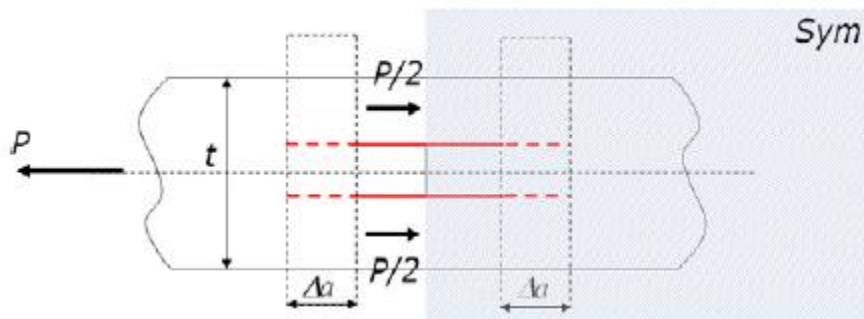


Figure 3.21 - CCP specimen: unloaded central plies [36]

A problem could be given by the different growth of the four delaminations, due to various causes as material inhomogeneity or imperfect manufacturing. This causes different levels of *SERR* for each delamination, complicating the study of the phenomenon.

Next figure 3.22 displays the preliminary sketch of the plate for the *CCP* specimens.

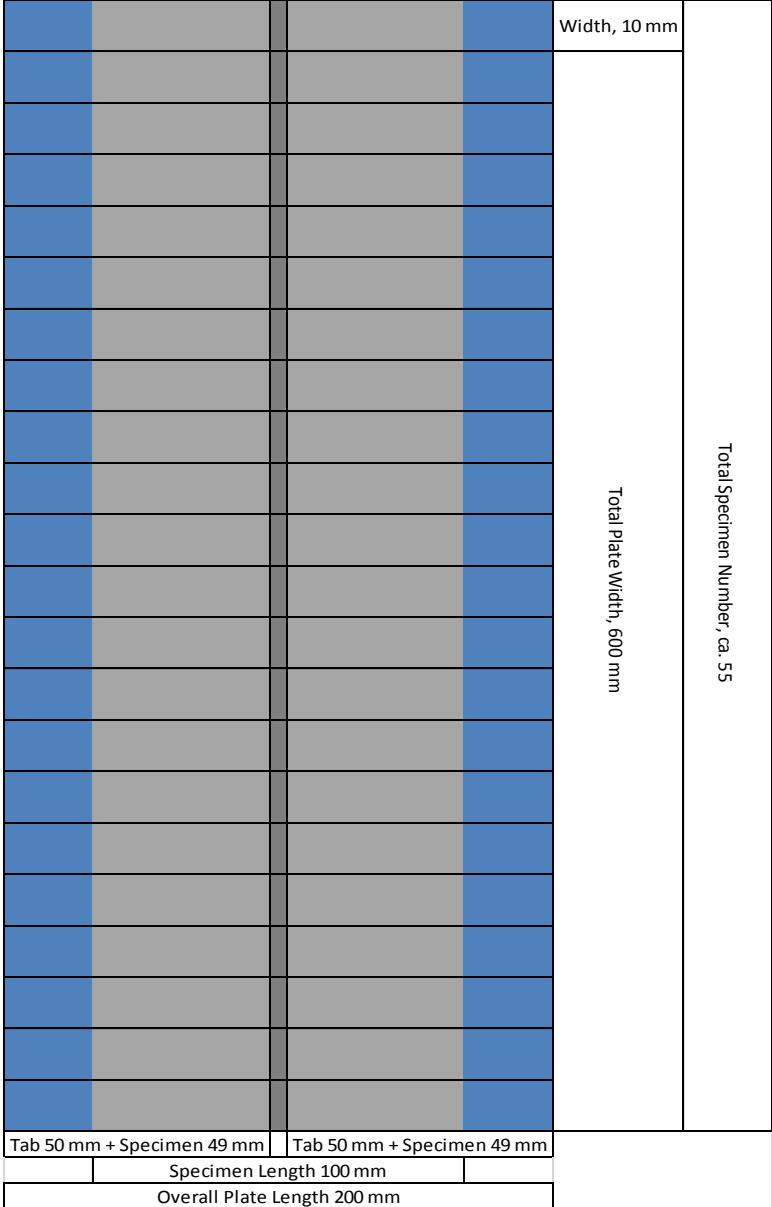


Figure 3.22 - Central Cut Ply plate layout

At the edges of each specimen a tab of 50 mm has to be bonded, after the surface has been prepared sanding it with sandpaper (240 grit), in order to mount the specimen in the grips of the loading machine.

## 4. Mode I Interlaminar Fracture Toughness Tests

---

Mode I Interlaminar fracture captures more attention and interest from the researchers since its delamination initiation energy is lower than the one evaluable for shearing mode [16]. In this chapter the procedures for the tests to evaluate the interlaminar fracture toughness will be exposed, both for quasi-static and fatigue loading mode. The reported procedures are extrapolated from the *ASTM* standard methods, *D5528-01* [17] and *D6115-97* [18], respectively for quasi-static and fatigue tests.

The same document [17] also provides the calculation methods to process the data collected from quasi-static tests, here reported in the second paragraph. The calculation methods used for fatigue loading test are instead provided by *ASTM E647* [19].

### 4.1 Quasi-static test

#### 4.1.1 Procedure

Mode I interlaminar fracture toughness tests are first carried out to obtain basic static parameters. For example, the methods now described allow to find the *R curve*, the plot of  $G_{Ic}$  versus the delamination length  $a$ , which gives the possibility to compare different specimens and find also an average value for the tested batch.

The *ASTM* standard [17] suggests to perform the test on at least 5 specimens, *DBC* type.

This method is based on two simply hypothesis:

- laminates have an even number of plies, unidirectional;
- delamination growths in the  $0^\circ$  direction.

The suggested dimensions for the specimen are those anticipated previously in fig. 3.9, i.e. specimens 125 mm long and 25 mm wide, with a thickness ( $2h$ ) between 3 and 5 mm.

Before to start, must be considered first of all that the nonadhesive insert film used in the second cure cycle has already formed an initial delamination site; its length must be of approximately 63 mm, that correspond to a 50 mm length from the load line to the end of the insert film. To be sure of the exact position of the edge of the insert point, a mark should be done on the graph paper, in order to be able to calculate accurately the length of the delamination from that point.

The specimen must be then mounted in the grips of the testing machine (*MTS 10* kN) through the loading blocks (or piano hinges), at a room temperature.

After these two initial steps, the procedure can be performed as resumed in the following points:

1. Measure width and thickness of each specimen to the nearest 0.05 mm at the midpoint and at 25 mm from either end; variation in thickness must not exceed 0.1 mm. Report any variation which move away from the mentioned value (see *Chapter 3*).
2. As load is applied measure then the delamination length  $a$ ; the initial delamination  $a_0$  is the distance from the load line to the end of the insert.
3. Set an optical microscope to see the delamination growth along one edge.
4. *Initial Loading:*
  - 4.1. Load at a constant crosshead rate between 1-5 mm/min;
  - 4.2. Record (continuously) the load and the displacement values; record delamination position;
  - 4.3. During loading record the point of the visual onset of delamination observed on the edge;
  - 4.4. Stop the loading after an increment of delamination crack growth of 3-5 mm (note if it is unstable);
  - 4.5. Unload at constant crosshead rate of up to 25 mm/min;
  - 4.6. Mark the position of the tip of the precrack on both edges of specimen (note if they differ by more than 2 mm);
  - 4.7. Check if initial loading process must be replaced by wedge precracking.
5. *Reloading:*
  - 5.1 Reload at the same constant crosshead speed of 1-5 mm/min as the initial loading, without stopping or unloading until final delamination increment has been reached;
  - 5.2 Record the load and displacement at which the onset of delamination moves from the precrack;
  - 5.3 On the continuation record load and displacement every 1 mm (ideally) in the first 5 mm. After that record data every 5 mm until delamination has propagated at least 45 mm from the precrack tip; record then every 1 mm for the last 5 mm of delamination propagation, up to total 50 mm of length beyond the tip of precrack;
  - 5.4 Unload at a constant crosshead rate of 25 mm/min;
  - 5.5 Mark the position of the tip of the delamination on both edges; note if it differs more than 2 mm;
  - 5.6 Note permanent deformation and deviations of delamination from the midplane of the laminate, which invalid the results; in this case it is advisable to test then a replacement specimen.
6. *Interpretation of the results:* Determine several initiation  $G_{Ic}$  values from the load-displacement plots and use them with subsequent propagation values to obtain the R curve.  $G_{Ic}$  values corresponding to the following points should be calculated, for each one of them the initial delamination length  $a_0$  must be used.

6.1 *Deviation from Linearity:* Calculate an initiation value for  $G_{Ic}$  at the point of deviation from linearity (*NL*, or *onset of nonlinearity*) from  $P$ - $\delta$  plots. This value is the lowest (ca. 20% lower) of the three initiation values and it is recommended in durability and damage tolerance analysis for laminated structures as delamination failure criteria. Furthermore this value corresponds to the physical onset of

delamination, starting from the insert in the interior of the specimen width. It is considered the most accurate onset value.

6.2 *Visual Observation*: Record a visual observation (*VIS*) value for  $G_{Ic}$  from  $P$ - $\delta$  plot in the first point at which the delamination is visually observed to grow from the insert on either edges using the microscope/mirror.

6.3 *5% Offset/Maximum Load*: another value of  $G_{Ic}$  from  $P$ - $\delta$  plot, calculated as the intersection between the nonlinear part of the curve and a line starting from the origin and offset by a 5% increase in compliance from the linear part of the curve.

Concluding this section, it is important to emphasize a few adaptations made on the procedure described above during the tests performed in the lab. In particular, the recording of load and displacement values was automatically conducted by the software employed, and not manually as suggested by the reference.

Concerning point 3 a digital camera has been used instead of the proposed optical microscope in order to obtain pictures of the delamination length growing. A second camera has been placed in way of recording the values of the current load and displacement, which introduces so a modification to point 4.2. The cameras were programmed to capture a picture every 5 seconds. These pictures were successively used to visually study the delamination growth during the data elaboration.

With regard to point 4.6 the end of the precrack was marked just on the side exposed to the camera, since the onset point was symmetric on both edges. Point 5.4 suggests to unload the specimen after recording the last delamination growth value; this was not included in the procedure used because was considered not necessary.

Finally, a clarification concerning the values used among those proposed in points 4.1 and 4.6. For both the loading phases the value of the rate imposed by the procedure used in the machine was 1mm/min.

#### 4.1.2 Data Calculation method

Once the procedure has been carried on, several steps must be followed to calculate the interlaminar fracture toughness.

Three different methods of data reduction are reported in reference [17]:

1. *Modified Beam Theory (MBT)*: with this method the strain energy release rate for a perfect built-in *DCB* specimen is given by

$$G_I = \frac{3P\delta}{2ba} \quad (4.1)$$

The above formula overestimates  $G_I$  because the specimen is not perfect built-in and rotation may occur at the delamination front. To correct it the beam is treated as it has a slightly longer delamination kept in account through the correction factor  $|\Delta|$ , determined experimentally from the plot of  $C^{1/3}$  versus  $a$ , where  $C$  is the compliance, i.e. the ratio of the load point displacement to the applied load,  $C=P/\delta$ . The absolute

value of the x-axis intercept of the  $C^{1/3}$  versus  $a$  plot is equal to  $\Delta$ . The resultant delamination length is considered to be  $a+|\Delta|$ .

The mode I interlaminar fracture toughness can be so calculated modifying (4.1) as follows:

$$G_I = \frac{3P\delta}{2b(a+|\Delta|)} \quad (4.2)$$

Can also be determined the lamina modulus of elasticity  $E_I$ , which is independent from the delamination length, although it may increase with the fibre bridging:

$$E_I = \frac{64(a+|\Delta|)^3 P}{\delta b h^3} \quad (4.3)$$

2. *Compliance Calibration Method (CCM)*: this method provides a least squares plot of  $\log C$  versus  $\log a$ , where the delamination length values are those obtained visually and the values of  $C$  are obtained by the data furnished by the testing machine. The straight line through the data is the best least squares fit.

The exponent  $n$  is obtained as the slope of this line according to  $n = \Delta y / \Delta x$ ; these two values can be easily visualized in fig. 4.1 used as an example.

The formula provided by this method to calculate the mode I interlaminar fracture toughness is:

$$G_I = \frac{nP\delta}{2ba} \quad (4.4)$$

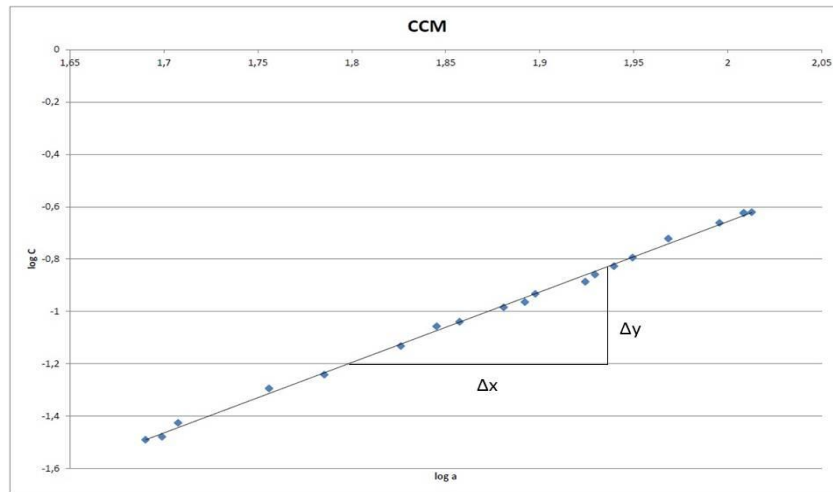


Figure 4.1 - Log C versus log a example plot

3. *Modified Compliance Calibration (MCC) Method*: the delamination length is normalized by the specimen thickness  $a/h$  and plotted in a least squares plot as a function of the cube root of the compliance  $C^{1/3}$ . The plot is once again obtained using the values of delamination length visually observed and the load and displacement values given by the machine. The slope of this plot is indicated as  $A_I$  and is used in the formula proposed by this method to calculate the fracture toughness:

$$G_I = \frac{3P^2C^{2/3}}{2A_1bh} \quad (4.5)$$

The *MBT* method yields the most conservative value of  $G_{Ic}$  and it is so recommended. Nevertheless in the present work also the results obtained with the *CCM* method are taken in account, since the two theories seem to agree rather well in terms of values provided, as will be shown in the appropriate chapter.

## 4.2 Fatigue test

### 4.2.1 Procedure

The purpose of this kind of test is to evaluate the number of cycles  $N$  for the onset of delamination growth, based on the value of  $G$ , under the hypothesis of linear elastic behaviour.

Each specimen is cycled under displacement control, between a minimum and a maximum displacement at a specified frequency. The displacement ratio  $\delta_{min}/\delta_{max}$  is here identical to the R-ratio for linear elasticity and small deflections.

The number of displacement cycles at which the onset of the delamination growth occurs,  $N_a$ , is recorded. After calculate  $G_{Ic}$  this value will be necessary using the *MBT* to find the relation between  $G_{I_{max}}$  and  $N_a$ .

The *ASTM* standards [18] suggest to perform the test on at least 6 specimens of DBC type.

Two preliminary steps have to be followed before to start with the standard procedure.

1. First of all a method to calculate  $N_a$  must be chosen between the three available:
  - a.  $N_a^{vis}$ : visual method which records the number of cycles until the delamination was observed to grow on the edge;
  - b.  $N_a^{1\%}$ : records the number of cycles until the compliance has increased by 1%;
  - c.  $N_a^{5\%}$ : records the number of cycles until the compliance has increased by 5%.

The first method is the one which gives the lowest values, so it is the recommended method.

2. The maximum load  $P_{max}$  must be estimate. If the quasi-static test has been performed, it may be assumed that the lowest value of peak cyclic energy release rate will be 10% of  $G_{Ic}$ . So it is recommended to test the specimen statically first, and then to test it under fatigue.

Once completed these starting steps, the following procedure can be performed; notice that some points are the same of those inherent to the procedure presented in the previous section for quasi-static test, so they will not be repeated:

1. *Quasi-static test*: Determine the relation between compliance and delamination length using the test described above in section 4.1.1.

Using specimen from the same batch, note the average value of all the constants in the compliance expression in order to aid in determining parameters for the successive fatigue test:

- $|A|_{av}$ , the average value of the correction factor already presented for *MBT* method.
  - $[G_{Ic}]_{av}$ , the average value of the critical interlaminar fracture toughness.
  - $[\delta_{cr}]_{av}$ , the average value of the critical displacement for quasi-static delamination growth from the end of the insert film obtained during the quasi-static test.
2. See point 1. in quasi-static procedure.
  3. See point 3. in quasi-static procedure.
  4. Determine the initial delamination length  $a_0$ .
  5. Determine various  $G_{I_{max}}$  values in order to elaborate a complete  $G-N$  curve. Start then the test at a  $G_{I_{max}}=0.5[G_{Ic}]_{av}$ .  
Obtain  $\delta_{max}$  as:  $\frac{\delta_{max}^2}{[\delta_{cr}]^2 av} = \frac{G_{I_{max}}}{G_{Ic}} = 0.5$
  - 5.1 Calculate  $\delta_{min}$  and  $\delta_{mean}$  from the chosen displacement ratio and  $\delta_{max}$ .  
Start the fatigue test and record  $P_{max}$  as soon as possible.  
Set the frequency between 1-10 Hz.
  6. *Compliance Monitoring*: the onset of delamination growth is studied by monitoring the decrease in the compliance.
    - 6.1 Record the compliance (slope of the load-displacement curve) and the number of cycles elapsed, using a data acquisition system from the available ones.
  7. Plot the values mentioned above, i.e. the compliance versus the elapsed cycles (fig. 4.2).

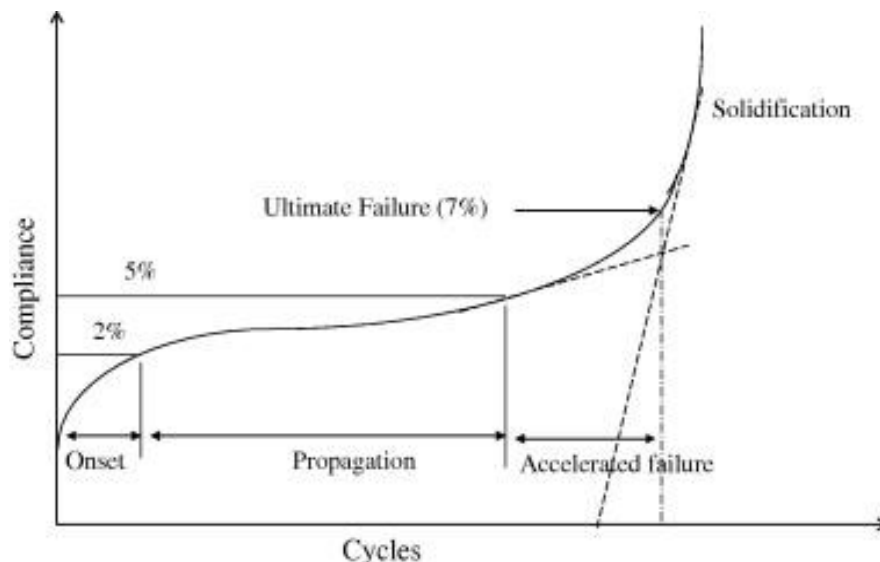


Figure 4.2 - C versus N general plot

8. Stop the test after one of the following events:
  - The compliance has increased by 105% of its value at  $N=I$ ;
  - The number of cycles has exceeded the maximum one desired.

As done for the static test procedure, an adaptation to the suggested procedure was employed. In particular to record the delamination growth length was again adopted a digital camera in the way of the optical microscope.

#### 4.2.2 Data calculation method

Once the procedure to acquire the data is complete, the maximum cyclic strain energy release rate can be calculated using the values of  $\delta_{max}$ ,  $P_{max}$ ,  $a$  and the average values of  $n_{av}$  and  $|\Delta|_{av}$ ; thus the actual test  $G_{I_{max}}$  is, considering the CCM:

$$G_{I_{max}} = \frac{n_{av} P_{max} \delta_{max}}{2ba} \quad (4.6)$$

In alternative one of the other expressions presented above for the reduction methods in static tests can be used, considering again the maximum values of  $P$  and  $\delta$ .

If it is necessary correction factors suggested in reference [18] must be applied.

The crack growth rate can be estimated using different approaches. Two methods can be used following the indications of the *ASTM E647* Standard [19]: the first one is identified as *secant method* while the second one is the *polynomial method*.

1. *Secant method*: the crack propagation rate is calculate using the slope between two adjacent points:

$$\frac{da}{dN} = \frac{a_{i+1} - a_i}{N_{i+1} - N_i} \quad (4.7)$$

This method is simple but allows an accurate representation of the data. On the other hand it affected by scatter in the experimental data, even magnified in the calculation of the  $da/dN$  rate.

2. *Incremental Polynomial method*: based on incremental fitting a second order polynomial to sets of  $(2n+1)$  data points throughout the entire data range. The  $n$  parameter can be chosen in order to have sufficient data points to obtain a good fitting. The polynomial fitting is expressed by the equation:

$$a = b_0 + b_1 \left( \frac{N - C_1}{C_2} \right) + b_2 \left( \frac{N - C_1}{C_2} \right)^2 \quad (4.8)$$

The regression parameters  $b_0, b_1$  and  $b_2$  are obtained by applying the least squares method to the data set.  $C_1 = 1/2(N_{i-n} + N_{i+n})$  and  $C_2 = 1/2(N_{i-n} - N_{i+n})$  with  $i = (n+1)$ , are terms used to set the scale on input data so that numerical difficulties can be avoided during the process.

Differentiating previous equation (4.8) with respect to the number of cycles  $N$  the crack growth rate is then obtained:

$$\frac{da}{dN} = \frac{b_1}{C_2} + 2b_2 \left( \frac{N - C_1}{C_2} \right) \quad (4.9)$$

The whole process can be easily carried on using the computer program for data reduction reported in reference [19]. It can be implemented in an Excel file which exploits the macro function of the software, giving as output the wanted values of the crack growth rate.

The convenience of this method is its capacity to reduce the scatter in the determination of the crack growth rate, but it can mask real effects, especially for small data set; by a comparison between the results obtained with the two different methods (figure 4.3) can be noted a good agreement between them but also a major scatter presented by the *secant method* [20].

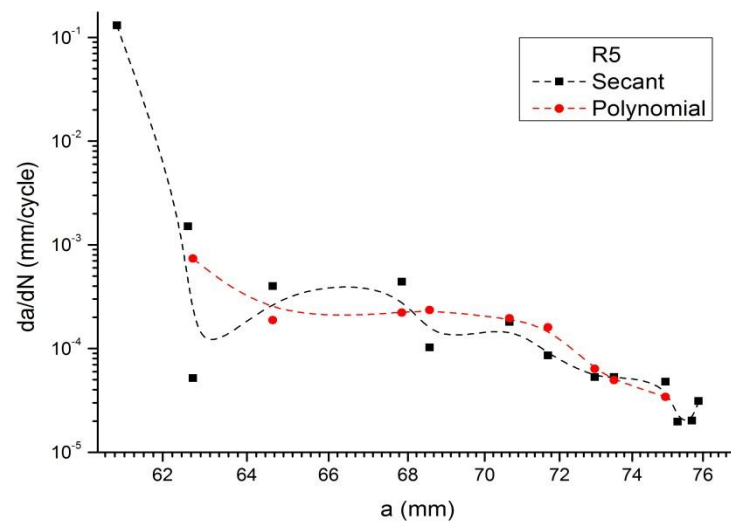


Figure 4.3 -  $da/dN$  vs.  $a$  plot: comparison secant vs. polynomial method

The approach chosen to develop the present research is based on *LEFM* theory, as already reported. It provides the way to identify a function to relate one fracture parameter, in this case the *SERR*  $G$ , with the fatigue crack growth rate.  $G$  is used in the way of the *stress intensity factor*  $K$  in crack growth study. The correlation between the crack growth rate per cycle  $da/dN$  and the fracture parameter  $G$ , when plotted in a logarithm scale presents a sigmoidal shape and for a large range it follows a power law. This plots have three zones, identifiable in figure 4.5 which represents an example of generic curve [21]:

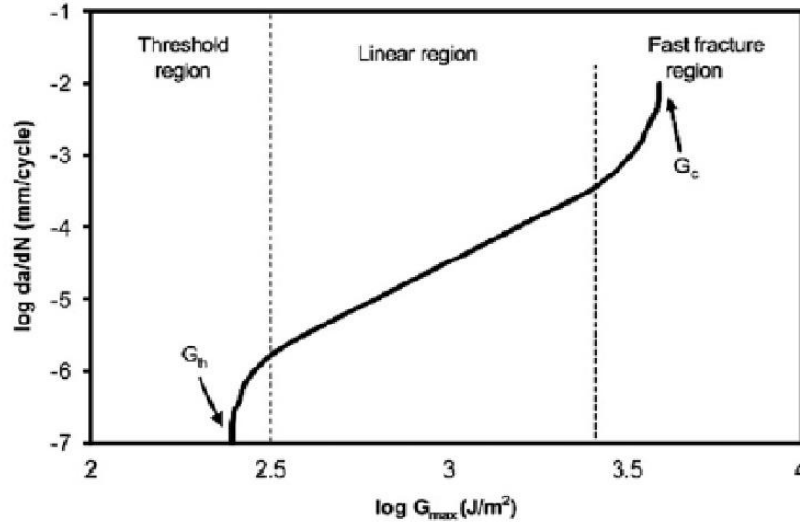


Figure 4.4 - Crack growth rate general plot [21]

1. *Threshold region*: region below the fatigue threshold value  $G_{th}$  where the crack growth tends to zero.
2. *Linear region*: region in which the curve evolves with a linear behaviour, described by the *Paris* equation or an adaptation of it, generally indicated by

$$\frac{da}{dN} = C_d (G_{eff})^{n_d} \quad (4.10)$$

3. *Fast Fracture region*: region characterized by the instability of the crack which conducts to catastrophic growth and final failure.

The linear region is the only one studied in the kind of test here presented.

According with reference [11], the use of  $G$  rather than  $K$  as fracture parameter originates from the difficulty for inhomogeneous materials in evaluating the local crack tip stresses used to determine  $K$ . Using this analogy, the *Paris* equation expressed by (4.10) can be used to describe the behaviour under cyclic load. Nevertheless a common formulation for  $G_{eff}$  is still object of discussion.

Two different formulations of  $G_{eff}$  are those usually used: the first one proposes the use of  $G_{max}$ , the second the difference between the maximum and the minimum value of *SERR*  $\Delta G = G_{max} - G_{min}$ . Both theories have benefits and disadvantages.  $G_{max}$  is considered useful because it represents the parameter which defines the static failure limit but on the other hand it does not contain information about the minimum applied load, resulting in a dependency on the load *R-ratio*.  $\Delta G = G_{max} - G_{min}$  use the *SERR* range to avoid this phenomenon, but it does not respect the rules of superposition for  $G$ ; thus it does not eliminate the *R-ratio* dependency. A third formulation based on a review of the Linear Elastic Fracture Mechanics theory is found able to remove the mentioned dependency and the residual stress effects. According to *LEFM* assumptions  $G$  can be related to  $K$ , but compared with this second it is easier to be determined ahead of the crack tip. The relationship between the two parameters is  $G \propto K^2$ . Thus it seems less reasonable to assume a direct analogy with  $K$  choosing  $\Delta G = G_{max} - G_{min}$ ,

because an arithmetic difference in *SERR* does not correspond to a difference in *SIF*. In addition considering the rules of superposition for *SERR*, for a linear system there is no interaction between the loading modes so that the total *SERR* is an arithmetic sum of *SERR* for each mode, while the *SERR* from the same loading mode is the square of the sum of the square root of the various terms:

$$G_T = G_I + G_{II} + G_{III}$$

$$G_I = \left[ \sqrt{G_{I1}} + \sqrt{G_{I2}} + \dots \right]^2$$

The presented demonstration confirms that for a given loading mode  $\Delta G$  should not be the arithmetic difference of  $G_{max}$  and  $G_{min}$ .

Assuming these starting points the formulation of  $G_{eff}$  results in  $\Delta G_{\sqrt{}} = \left( \sqrt{G_{max}} - \sqrt{G_{min}} \right)^2$ , since  $\Delta K \propto \left( \sqrt{G_{max}} - \sqrt{G_{min}} \right)^2$ .

This similitude parameter preserves the same delamination growth behaviour for different stress ratio, solving so the issue mentioned concerning the other two parameters.

Reference [22] conducted some experiments on the same material studied here, comparing the results under fatigue loading for  $\Delta G_{\sqrt{}}$  and  $\Delta G$  for different *R-ratios*. The authors found that the scatter using  $\Delta G$  is higher and validate it saying that this is due to the violation of similitude; if it was respected it was expected to see the same delamination growth behaviour for a given value of the fracture parameter. Using  $\Delta G_{\sqrt{}}$  instead makes the curves collapse in a single trend line as the similitude is preserved.

Furthermore it solves the problem related to the residual stresses and/or strains after curing, which afflicts the fatigue loading as a variation in the mean stress or stress ratio. Indeed using  $\Delta G_{\sqrt{}}$  instead of  $\Delta G$  the residual stress component does not affect the value of *SERR*. Calling this component  $G_r$  and the component due to applied loads  $G_{appl}$ :

$$\Delta G_{\sqrt{}} = \left( \sqrt{G_{max}} - \sqrt{G_{min}} \right)^2 = \left[ \left( \sqrt{G_{applmax}} + \sqrt{G_r} \right) - \left( \sqrt{G_{applmin}} + \sqrt{G_r} \right) \right]^2$$

$$= \left( \sqrt{G_{applmax}} - \sqrt{G_{applmin}} \right)^2$$

To distinguish the two different fracture terms a differentiated notation has been selected in order to not create any misunderstanding during the description of the results.

For the reasons here presented the third approach is the one used to process the data collected during fatigue tests (see *Chapter 6*).

## 5. Mode II Interlaminar Fracture Toughness Tests

---

The procedures for mode II tests are here presented for the sake of completeness. At the beginning of the study these tests were included in the preliminary plan, but the relatively limited time and the continuous activity carried on in the lab did not allow to reach the aim. It still propose of this thesis to report the general approach which was meant to be utilized to carry on the tests, in case the reader would want to continue the road undertaken.

Previously was anticipated that a standard procedure for this type of tests does not exist yet. A school of thought asserts that it is impossible to design a mode II test, since the failure mode is always dominated by mode I (tension). This can be rebutted considering that an heterogeneous material on a microscopic scale cannot involve pure loading, like for example for mode I, where however *DCB* specimen are not prevented from supplying information on a macroscopic scale. For mode II samples, crack initiation is given by relative sliding of the two surfaces, which is a pure mode II load, and the following rotation and opening of these cracks are not taken in account in the data analysis. Some practical difficulties represent a problem to the standardization of mode II test for measuring  $G_{IIc}$  in composite materials. These factors are essentially the type of crack starter, the definition of onset, the stability, the friction and last the data analysis methods. Concerning the precracking, has been pointed out that the onset value provided by starter films results in higher values of  $G_{IIc}$  than the ones furnished by precracks. Considering a precracking procedure involving a mode I test prior to the mode II test minimizes errors deriving from wedge precrack methods. A valid alternative is a mode II precrack, even if the problem in this case is connected to the determination of the precrack length, solvable with a compliance calibration. Defined the type of starting defect, the issue is related to the visual determination of onset value, since it must be obtained as for mode I test, but the visual observation results more difficult and thus less reliable. The propagation can represent an issue at the time that it is unstable, since it makes difficult to evaluate the reliability of the tests from inserts and to evaluate the *R-curve* for the material. Friction issues between the crack surfaces have been solved using films between them, but more work has to be carried on this sense to eliminate the undesired effects. Finally the data analysis is considered in some ways less reliable than the previous mode I study since the small variations of compliance during crack propagation make more difficult the validation of the data. Various methods have been proposed which include correction factors; they can be examined in depth referring to reference [23], which has been followed to summarize what just exposed.

Since the road to standardization has not been concluded yet, in the present work tests were planned following previous experiments conducted by other authors and pre-standardization studies, both for three-point bending test [24 - 30] and *CCP* test [31 - 36].

## 5.1 Three-point bending test

Greater attention in all works has been given to static strength assessing, while fatigue tests the *ENF* test (fig. 5.1) is less convenient and reliable in results. A line of action has been traced based on a review of the available procedures and data calculation methods in order to have an overall view of the problem.

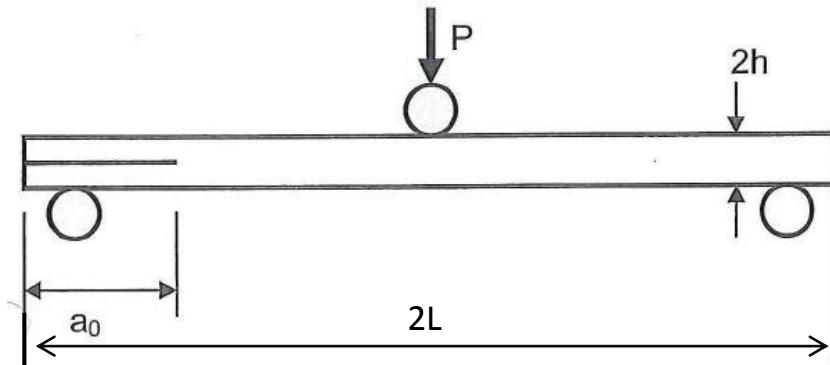


Figure 5.1 - Three-point bending test setup example

The *ASTM D790* [24] standard method proposes a procedure to determine the flexural properties of unreinforced and reinforced plastics and composites, utilizing a three-point bending loading system applied on rectangular samples, denoted as *ENF* specimens. It is thus possible to determinate stresses and strains from load versus displacement plots. Unfortunately the equations proposed by this method are only valid in the linear elastic region of the curves, giving so inaccurate results concerning the non-linear region.

Airbus Industrie Test Method (*AITM*) [25] reports a procedure to be followed for testing *ENF* specimens with three-point bending test method to determine mode II *IFT* energy  $G_{IIc}$ . The procedure must be applied on specimens where the initial crack has been introduced according to the mode I procedure, during which did not occurred either fibre bridging or moving of the crack to plies adjacent to the midplane. The specimens have to be tested after an ageing procedure to condition them at  $(23\pm 2)^{\circ}\text{C}$  and a white ink layer on the side edges is applied. The procedure to record a continuous load and displacement data should be then performed:

1. Set the load cell to zero;
2. Looseness between the specimen and the load nose must be removed adjusting the displacement;
3. Set the displacement to zero if necessary;
4. Applied load in displacement control with a crosshead speed of 1 mm/min;
5. Visually observe the crack tip to evaluate the crack propagation onset;
6. After recording the critical load at delamination onset, stop the loading when a load drop takes place confirming the starting of delamination propagation;
7. Unload the specimen to zero at the end of the test.

The data calculation proposed to evaluate  $G_{IIc}$  is based on the formula:

$$G_{IIc} = \frac{9Pa^2\delta}{2b\left(\frac{1}{4}L^3+3a^3\right)} \quad (5.1)$$

Another procedure to evaluate mode II toughness was deduced using as reference a pre-standardization work on *CFRP* carried out by the *JIS Committee* [26]. The *ENF* samples are again suggested to be employed because of their simplicity and sufficient given information.

The test aims to record the load, the load point displacement and the crack shear displacement (*CSD*), recorded using a *CSD* gauge. Its main body is placed on the upper sprit lower part.

The compliance is calculated applying an unload procedure, in order to determine the crack propagation length. To stabilize the crack extension a control method is applied.

It is so possible to measure the fracture toughness  $G_{II}$  during propagation. Three different methods can be considered:

1. *Conventional method*: the load point displacement speed is constant and controlled. An unstable fracture takes place, unless the  $G_{II}$  growths immediately after the crack initiation.
2. *CSD control method*: the *CSD* output is used as input in the feedback circuit of the servo-controlled test machine utilized. It is controlled in order to increase at a constant rate.
3. *Coordinate conversion control (CCC) method*: the same servo-controlled machine is used. The load point displacement and the load output give a simple circuit used as feedback for the test machine.

The *conventional method* is the most applied, although the second and third ones can be applied to prevent unstable fracture propagation.

The data analysis method provides for several equation to calculate mode II interlaminar fracture toughness  $G_{IIc}$ .

$$G_{IIc} = \frac{9P^2Ca^2}{2b(2L^3+3a^3)} \quad (5.2)$$

where:

$P$ = load;

$C$ = load point compliance;

$a$ = crack length;

$b$ = specimen width;

$L$ = half-span of the bending support.

The compliance can be obtained from the following expression:

$$C = \frac{2L^3+3a^3}{8E_Lbh^3} \quad (5.3)$$

where  $E_L$  is the longitudinal elastic modulus of the sample and  $h$  half its thickness.

The calculation of the collected data can be done using two different values of  $a$ , i.e. the initial value  $a_0$  and the propagation value  $a_p$ , whose expression is derived from equation (5.3).

$G_{IIc}$  can also be calculated using the following expression, which does not require the crack length value:

$$G_{IIc}^* = \frac{3P\delta}{8bh} \quad (5.4)$$

Here  $\delta$  takes into account automatically the effect of crack length increase. This method is used when the unloading process is not applied. On the other hand, when this method is applied the *CSD* compliance can be estimated from the unloading trace or also from the slope of a line drawn in the way to connect the starting point of the *CSD* versus load curve and a point of interest on the plot.

Equations can be combined to obtain three different method of calculation of  $G_{IIc}$ :

- *Method 1*: equation (5.2) considering initial  $a$ , i.e.  $a_0$ ;
- *Method 2*: equation (5.2) with  $a_p$  expression (see equation 5.9 below);
- *Method 3*: equation (5.4), which automatically considers the crack length.

The most used method is the first one; the other two methods are used to consider if it is possible to ignore the effects of crack growth, in particular in case of a tough matrix.

Two different plots can be obtained, one displaying the load versus *CSD* output and one the load versus load point displacement. Six points are considered “critical” in calculating the toughness:

1. *VDNL*: the point where the non-linearity starts in the load versus vertical load displacement plot;
2. *VD5%*: the point where the compliance has increased of 5% in the same graph as above;
3. *CSDNL*: the corresponding of 1. for load versus *CSD* displacement plot;
4. *CSD5%*: the corresponding of 2. for load versus *CSD* displacement plot;
5.  $P_{max}$ : the maximum load point;
6. *PROP*: points in the crack propagation region, using an average of 5 or more toughness values, calculated in the region where the crack length increased by 5-20 mm and the overall crack length is less than 45 mm.

Several data reduction methods can be distinguished in literature, both analytical and experimental. Some of them are based on delamination length knowledge while some others reach the evaluation of mode II toughness without delamination length measurements, because they are not easy to obtain.

Reference [27] divides the data reduction schemes in two categories:

- a. *Classical methods*: schemes based on Compliance Calibration Method or Beam Theory. *CCM* based on Irwin-Kies equation leads to calculate fracture toughness as:

$$G_{IIc} = \frac{3P^2 a^2 C_1}{2b} \quad (5.5)$$

where  $C_1$  is fitted using a cube polynomial.

*MBT* based on Wang-Williams proposal gives fracture toughness as:

$$G_{IIc} = \frac{9(a+0,42\Delta_I)^2 P^2}{16b^2 h^3 E_1} \quad (5.6)$$

where  $h$  is half thickness of the specimen,  $E_1$  is the axial modulus and  $\Delta_I$  a crack correction to account for the shear deformation, described as follows:

$$\Delta_I = h \sqrt{\frac{E_3}{11G_{13}} \left[ 3 - 2 \left( \frac{\gamma}{1+\gamma} \right)^2 \right]} \quad (5.7)$$

where  $E_3$  and  $G_{13}$  are the transverse and shear moduli and  $\gamma = 1,18 \frac{\sqrt{E_1 E_3}}{G_{13}}$ .

- b. *Compliance Based Beam Method (CBBM)*: data reduction method which calculates  $G_{IIc}$  using just the  $P$ - $\delta$  curves and takes in account some details neglected by the other methods, such as the dissipation of a non-negligible amount of energy ahead the crack tip, due to the Fracture Process Zone (*FPZ*), and the variability of the material properties between different specimens. It introduces a correction in compliance and a correction in crack length to obtain the equivalent crack length, i.e.:

$$C_{0corr} = C_0 - \frac{3L}{10G_{13}bh} \quad (5.9)$$

$$a_e = a + \Delta a_{FPZ} = \left[ \frac{C_{corr}}{C_{0corr}} a_0^3 + \frac{2}{3} \left( \frac{C_{corr}}{C_{0corr}} - 1 \right) L^3 \right]^{1/3} \quad (5.10)$$

so that the interlaminar fracture toughness can be expressed again by the Irwing-Kies relation:

$$G_{IIc} = \frac{9P^2 a_e^2}{16b^2 h^3 E_f} \quad (5.11)$$

where  $E_f = \frac{3a_0^3 + 2L^3}{8bh^3 C_{0corr}}$  is the flexural modulus calculated from the initial compliance and initial crack length.

In reference [6] was previously demonstrated how the shear deformation can influence the compliance and the strain energy release rate in *ENF* specimens depending on the material properties and samples geometry. It resulted, following the equations above, that the contribution of shear deformation for compliance increases with  $E/G_{13}$  and  $h/L$ , while for energy release rate increases with  $E/G_{13}$  and  $h/a$ . Therefore the author sustained that it is not appropriate to assess the accuracy of a model to calculate the *SERR* with mode II *ENF* tests by using the specimen compliance. The author reached the final conclusion that the expression for compliance based on the shear deformation beam theory gives an accurate prediction of the compliance value but could cause some errors if used to calculate  $G_{II}$ . The work was carried out several years before the others just presented and it is reported for completeness;

further investigation has been carried out on the subject throughout the years, so that the methods mentioned are retained still trustable for determining mode II fracture toughness.

Reference [28] proposes to perform tests on *ENF* specimens presenting an initial crack length, i.e. from the support at the cracked region to the end of the insert film, of 100 mm. This solution is adopted to avoid the instability of the *R-curve*, possible maintaining the initial crack length  $a_0$  lower than  $0,7L$ , where  $L$  is the half span length of the specimen. Specimens are supported by spans and a steel platen is placed between the specimen and the supports in order to reduce the indentation of the supporting point without limiting the rotation of this point. The load is then applied to midspan until the crack tip reaches the midspan or a bending failure is induced. The crosshead speed is set to 2 mm/min. A displacement gauge is placed below the midspan in order to record the loading line displacement and the  $P$ - $\delta$  plots, while a strain gauge of 2 mm bonded at the bottom of the midspan allows to obtain the longitudinal strain  $\varepsilon_x$  and so the  $P$ - $\varepsilon_x$  plots. The set up described is visible in figure 5.2 while a general example of the mentioned two plots is displayed in figure 5.3. The mode II *R-curves* are determined without measuring the delamination length. A few parameters are evaluated, i.e. the compliance of initiation point  $C_{L0}$  and the compliance during propagation  $C_{LP}$ , the load at the onset of nonlinearity  $P_{NL}$  and the load-longitudinal strain compliance  $C_S$ . The latter give the possibility to calculate the value of mode II initiation fracture toughness from the following expression:

$$G_{IIc} = \frac{3P^2 C_S}{4bLh} \left( \frac{6hl}{\frac{I}{2I'} - 1} \frac{C_L}{C_S} - \frac{2L^3}{\frac{I}{2I'} - 1} \right)^{\frac{2}{3}} \quad (5.12)$$

Equation (5.12) does not depend explicitly from delamination length, so its measure is not needed. Thus the propagation crack length is furnished by the calculation (5.13) using the equivalent initial crack length  $a_{eq0}$ :

$$a + \Delta_{II} = \left( \frac{6hl}{\frac{I}{2I'} - 1} \frac{C_L}{C_S} - \frac{2L^3}{\frac{I}{2I'} - 1} \right)^{\frac{1}{3}} \quad (5.13)$$

where:

$h$  = half-height of the crack-free portion of the specimen

$l$  = distance between the supporting point at the cracked portion and the strain gauge

$I$  = second moment of cross-sectional area in the crack free portion of the specimen

$I'$  = second moment of cross-sectional area in the cracked portion of the specimen

The additional crack length  $\Delta_{II} = a_{eq0} - a_0$  permits to calculate the propagation crack length  $\Delta a$  and so to the *R-curves* are obtained as the  $G_{II}$ - $\Delta a$  relationship. These curves are valid until the onset of nonlinearity so are reliable just for a restricted range of length. Figure 5.4 shows a generic example of mode II *R-curves* for two different types of *ENF* specimens used by the author during the tests.

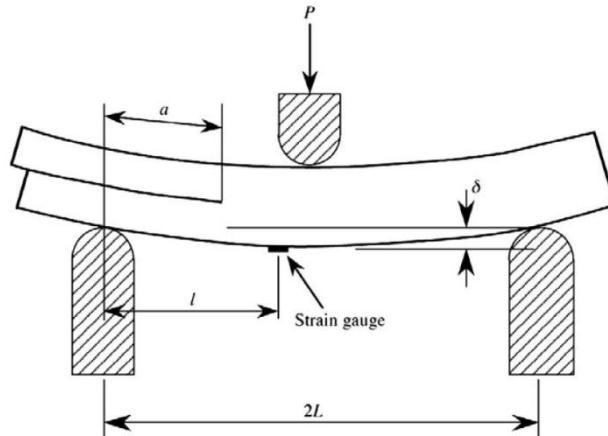


Figure 5.2 - Three-point bending test, strain gauge [22]

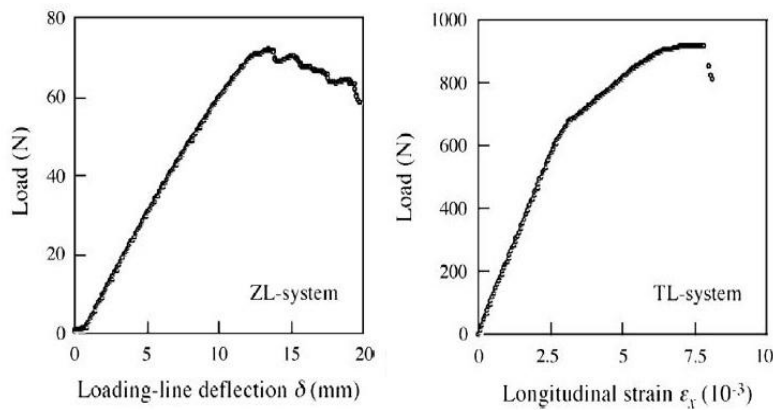


Figure 5.3 -  $P$  vs.  $\delta$  and  $P$  vs.  $\epsilon_x$  general plots [22]

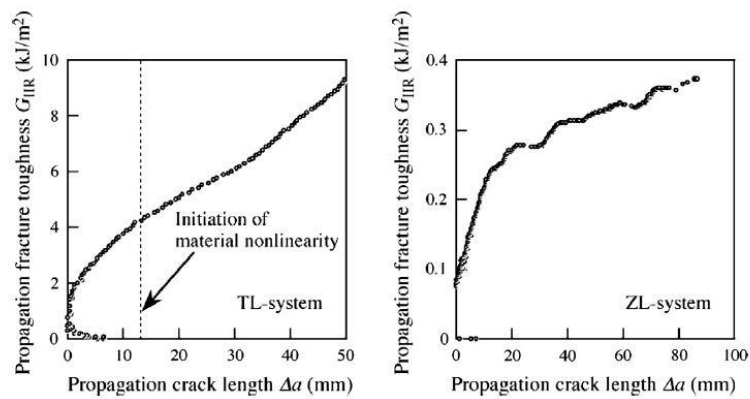


Figure 5.4 -  $G_{IIIR}$  vs.  $\Delta a$  general plots [22]

In reference [29] the author presents the test performed at the same manner just described with two minimal corrections, i.e. the crosshead speed set to 5 mm/min and an unloading process at 50 mm/min. The critical toughness is given by:

$$G_{IIc} = \frac{9Pa^2\delta}{2b\left(\frac{1}{4}L^3 + 3a^3\right)} \quad (5.14)$$

where  $b$  is the crack width. The load-deflection curve is obtained using the highest load  $P$  and deflection level.

NASA reference [30] presents tests performed on two kinds of *ENF* specimens, one non-precracked with a Teflon insert film and one precracked. Quasi-static tests are performed on both kinds to determine the fracture toughness, while fatigue tests are performed only on precracked specimens to study delamination onset and growth. Fatigue test is conducted applying a sinusoidal cyclic loading at a frequency of 5 Hz and setting the stress ratio at  $R = 0.1$  under loading control. Tests run at the maximum cyclic load  $P_{max}$  gave values of a  $G_{II_{max}}$  corresponding to 50%, 40%, 30% and 20% of the average value of  $G_{IIc}$  obtained from static tests. During the test the compliance has been measured with constant intervals of cycles (every 2 or 10 cycles) to calculate the corresponding crack length. The tests were stopped after the crack reached 50 mm of length. The data reduction in this reference is conducted using the compliance calibration to determine the  $G$  levels in static tests and the crack length in fatigue tests to evaluate the delamination onset and the crack growth curves. For each length the compliance was obtained by a least-squares linear regression analysis using equation (5.15) and (5.16) to determine the coefficients  $m$  and  $A$  respectively as the slope and the intercept of the plot of  $C$  versus  $a^3$ :

$$C = A + ma^3 \quad (5.15)$$

$$a = \left( \frac{C-A}{m} \right)^{\frac{1}{3}} \quad (5.16)$$

The static fracture toughness, using as  $P$  the maximum load from the fracture tests, is given by (5.17):

$$G_{II} = \frac{3mP^2a^2}{2b} \quad (5.17)$$

For fatigue study the above mentioned maximum cyclic load is determined solving (5.17) for  $P$  (equation (5.18)) and then substituting the correct value of  $G_{II_{max}}$ .

$$P_{max} = \frac{1}{a_0} \left( \frac{2bG_{II_{max}}}{3m} \right)^{1/2} \quad (5.18)$$

## 5.2 Central Cut Ply test

Also known as Ply Interrupt (*PI*) test, the *CCP* test has been widely used to characterize mode II fatigue delamination growth [31].

The specimens present several advantages compared with the *ENF* type for characterizing fatigue delamination growth. In particular they loaded in tension so the effects of friction along the delamination interfaces are minimized. Second, the direct connection between the strain energy release rate and the applied load eliminate the source of scatter visible in *ENF* specimens.

The disadvantages observable are the instability of delamination growth during static tests and the already mentioned (*paragraph 3.3.2*) issue related to the interruption, where four delamination take place at the same time. If the length of these delamination is not the same, problems in data analysis can be observed. In particular any difference in the length of the present delaminations will be magnified during delamination growth, as demonstrated by a numerical analysis in reference [32].

In reference [33] the author presents a procedure to conduct the tests, based on previous static tests of the same specimens. The maximum fatigue loads are chosen as a percentage of the Ultimate Tensile Strength (*UTS*) of the specimen calculated through the static tests. The static failure occurs at the interrupted central section. There the delamination growth was monitored in each one of the four edges of the gap determined by the interruption (figure 5.5).

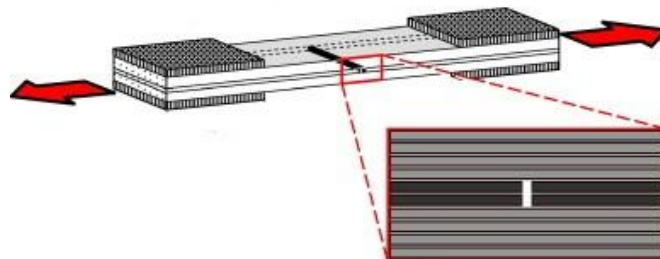


Figure 5.5 - Central Cut Ply test setup example [40]

Measurements of crack length and number of cycles for each specimen are collected after a number of cycles under static load equal to the maximum fatigue load. An example of a typical plot is visible in figure 5.6.

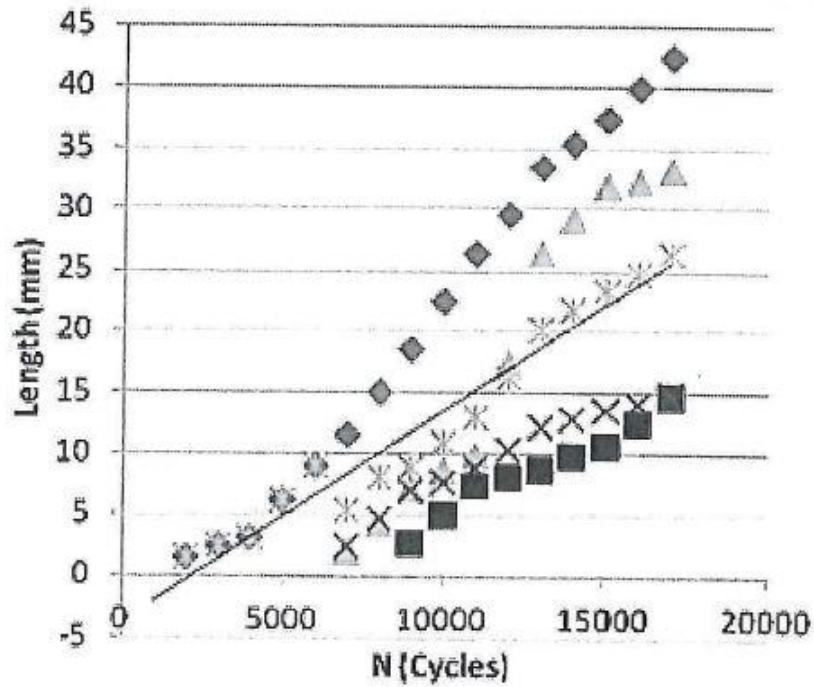


Figure 5.6 - a vs. N example plot [33]

Such plot allows for each specimen to calculate the average crack growth rate  $da/dN$  and the strain energy release rate, since it remains constant in this kind of geometry during the delamination propagation. Its value is evaluated using:

$$G_{II} = \frac{P^2}{b^2} \left( \frac{1}{2Eh_{out}} - \frac{1}{E(h_{in}+h_{out})} \right) \quad (5.19)$$

where  $h_{out}$  and  $h_{in}$  are respectively the thickness of the outer and inner layers. The calculation is repeated for each specimen tested at different load levels in the way to obtain a curve displaying the relationship between the crack growth rate  $da/dN$  and the energy release rate  $G_{II}$ . The curve is showed in figure 5.7 for different specimens in log-log scale in order to achieve a good linear trend.

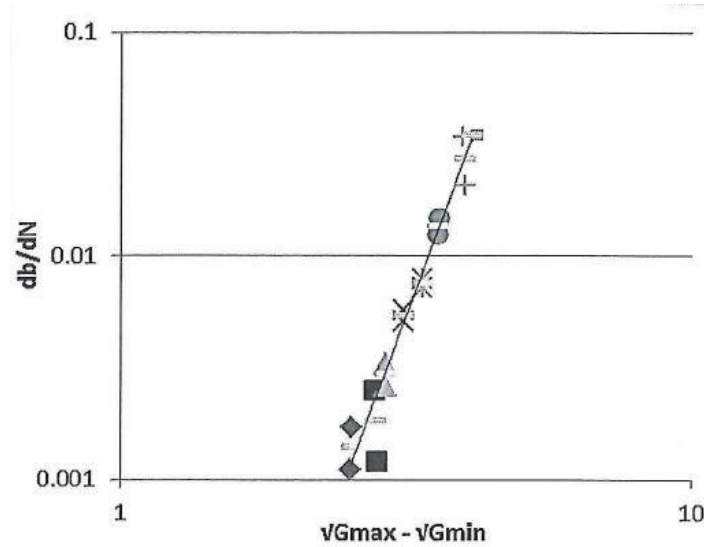


Figure 5.7 -  $da/dN$  vs.  $\Delta G\sqrt{}$  example plot [33]

Reference [34] presents a very extensive research on the subject. Concerning the present work, the attention is pointed on several factors examined which can be considered during the test preparation, for example the effect of specimen width, which does not affect the delamination stresses, and the effects of test rate, which show how a slow loading is not suitable from a design point of view. More interesting appear the results on the effects of specimens thickness, i.e. the significant decrease with increasing thickness, and the difference between the initiation and propagation stresses, resulting in a more subjective initiation stress than the propagation one ( $P_{init}=87-97\%P_{prop}$ ). The effect of the ratio of cut plies to continuous plies results to be very significant, and it determines also that the strength is more closely related to the number of cut plies than to the number of continuous ones. The tests are conducted by the author both in tension and compression, finding a delamination stress in compression much lower than the one in tension; finally, the effect of the presence of the gap between the cut plies is investigated: the specimen with the gap result stronger than the ones without gap (increase of 6-8%). It is remarkable the close form solution given to calculate the energy release rate in unidirectional laminates:

$$G = \frac{\sigma_{net}(h-t)t}{4E_{11}h} \quad (5.20)$$

where  $E_{11}$  is the longitudinal modulus,  $h$  is the specimen thickness,  $t$  is the cut plies thickness and  $\sigma_{net}$  is the average net section stress.

Equation (5.20) has been considered also by reference [35] to calculate the strain energy release rate for static tests. Going on it focus its attention also on fatigue analysis. To record strains in loading direction a clip gauge extensometer is placed; tests severity is defined in terms of ratio of the maximum net section stress to the average failure stress during static test. Using the recorded strains data the dynamics modulus is obtained as:

$$K = \frac{1}{A} \frac{\Delta P}{\Delta \varepsilon} \quad (5.21)$$

where  $A$  is the gross cross sectional area,  $\Delta P$  and  $\Delta \varepsilon$  are respectively the load and strain amplitude. The delamination length is then evaluated as directly proportional to the loss in stiffness:

$$a = L \left( 1 - \frac{K}{K_{initial}} \right) \left( 1 - \frac{t}{h} \right)^{-1} \quad (5.22)$$

where  $K_{initial}$  is the initial dynamic stiffness of the undamaged specimen. The crack growth rate is finally estimated linear fitting the curve of crack length versus the number of cycles and the  $SERR$  amplitude from equation (5.20) and the following (5.23) and then presented in the form of normalised Paris Law graphs (figure 5.8).

$$\Delta G = (1 - R^2)G_{IImax} \quad (5.23)$$

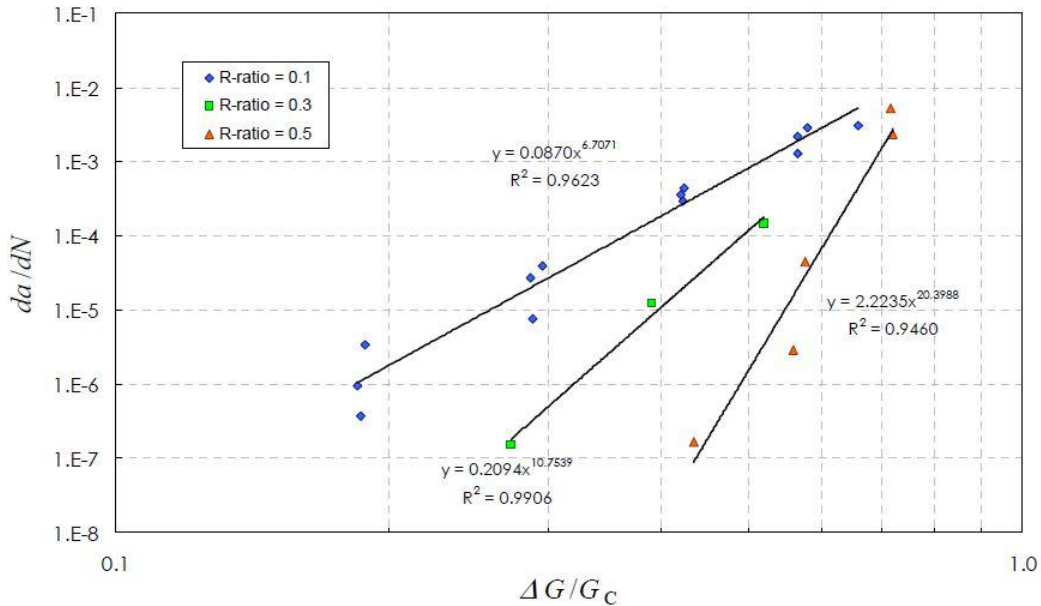


Figure 5.8 -  $da/dN$  vs.  $\Delta G/G_c$  example plot [35]

The last reference mentioned [36] presents a formulation of a new empirical law to predict mode II fatigue delamination growth rate in intermediate toughness fibre reinforced epoxies. The material used is a carbon/toughened-epoxy, tested under positive stress ratios related to an axial force  $P$  corresponding to a pure shear field for the four delaminations present at the interruption, since interlaminar compression avoids mode I opening. Defining  $\chi$  as the ratio of the number of cut plies to the number of total layers in the specimen, the mode II  $SERR$  can be evaluated by:

$$\bar{G}_{II} = \frac{1}{2} \frac{P^2}{Eb^2t} \left( \frac{\chi}{1-\chi} \right) \quad (5.24)$$

The value then associated to each single delamination is just half of the total value, so:

$$G_{II} = \frac{P^2}{4Eb^2t} \left( \frac{\chi}{1-\chi} \right) \quad (5.25)$$

It is remarkable how the value of *SERR* does not depend on delamination length so it is constant during the tests. Nevertheless equation (5.25) is not valid in a boundary layer region when  $a \rightarrow 0$  because the method is based on simple beam theory and it assumes that the central cut is unloaded during the test. This makes impossible to define a fatigue threshold performing the *CCP* test.

The characteristics of the specimens tested are the ones presented in the current work in *Chapter 3*. The delamination length is monitored “in situ” using a standard clip extensometer, which gives the value of strains  $\varepsilon^*$  substituted in:

$$a = L \frac{1-\chi}{\chi} \left( \frac{Ebt}{P} \varepsilon^* - 1 \right) \quad (5.26)$$

After fatigue tests in which the initial delamination length is zero. the interlaminar delamination propagation rate is found out from:

$$\frac{da}{dN} = L \frac{1-\chi}{\chi} \frac{E}{S\sigma_{IIc}} \frac{d\varepsilon^*}{dN} \quad (5.27)$$

where  $S$  is the load severity and  $\sigma_{IIc}$  is the nominal delamination stress, i.e. the ratio of the static initiation load to the nominal gross cross sectional area of the specimen.

A new fatigue delamination growth law is proposed assuming that under constant amplitude loading the delamination rate is constant:

$$\frac{da}{dN} = C \left( \frac{G_{IImax}}{G_{IIc}} \right)^{\frac{b}{(1-R)^2}} \quad (5.28)$$

It is introduced then a relationship between the mode II *SERR* and the Stress Intensity Factor (*SIF*)  $K$ , proportional to a parameter  $\alpha_{II}$  which depend on material properties and through-thickness Poisson’s ratio:

$$G_{IIc} = \alpha_{II} K_{II}^2 \quad (5.29)$$

which leads to:

$$\frac{G_{II}}{G_{IIc}} = \left( \frac{K_{II}}{K_{IIc}} \right)^2 \quad (5.30)$$

where  $K_{IIc}$  indicates the mode II toughness in terms of *SIF*. The delamination growth rate is finally given by:

$$\frac{da}{dN} = C \left( \frac{K_{IImax}}{K_{IIc}} \right)^{\frac{2b}{(1-R)^2}} \quad (5.31)$$

The results are plotted as a function of the ratio  $G_{II\max}/G_{IIc}$  in a double logarithmic scale; an example for different  $R$ -ratios is showed in figure 5.9.

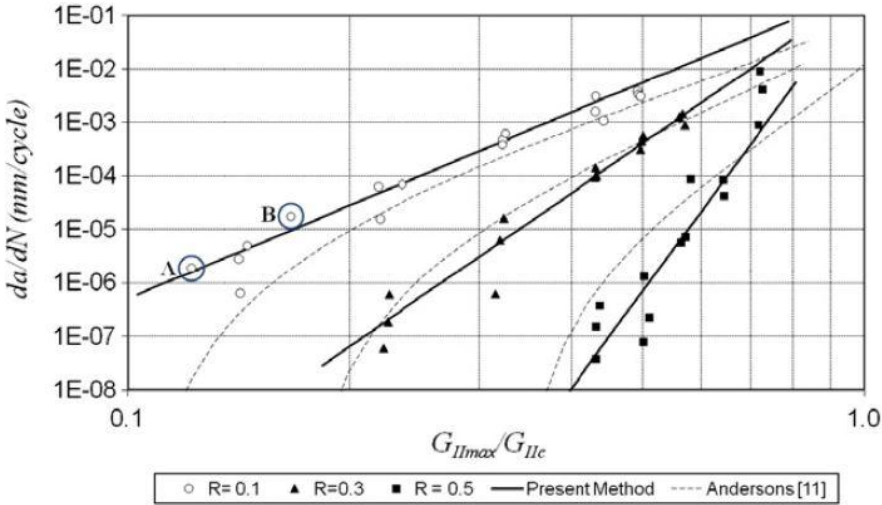


Figure 5.9 -  $da/dN$  vs.  $G_{II\max}/G_{IIc}$  [36]

The picture illustrates also a comparison with another method (Anderson, [37]). The final consideration of the author is that the semi-empirical model proposed in the paper is valid to describe the effects of stress ratio on fatigue delamination growth for materials whose toughness values range from 0,8 to 1,2  $\text{kJ/m}^2$ .

## 6. Tests Results

---

This chapter reports the data collected and the results reached through the methods previously described.

A brief reference to the procedures, the machine and the data reduction methods used will be presented where it is considered necessary to be sure that the reader follows the process in its entirety.

### 6.1 Quasi-Static Mode I Interlaminar Fracture Toughness Test

Mode I tests were performed on two different qualities of the same material, already described in *Chapter 3*.

The aim was to obtain the data for both *good* and *poor* qualities, in order to compare them to verify which behaviour belongs to each one and furnish so a reference for further employs of the present material. The present chapter will show thus the results found out during the whole experimental part of the research and they will be then compared and commented in the next chapter.

#### 6.1.1 Good Quality Material

The quasi-static test has been performed on five different specimens, indicated with R1, R2, R3, R6 and R8 (see figure 3.10 in *Chapter 3*).

The machine used to carry on the test is the *MTS 10 kN Elastomer*, a computer-controlled servohydraulic testing system with the *DAMSL Timelogger* software. In fig. 6.1 can be seen a picture of the machine during the test.

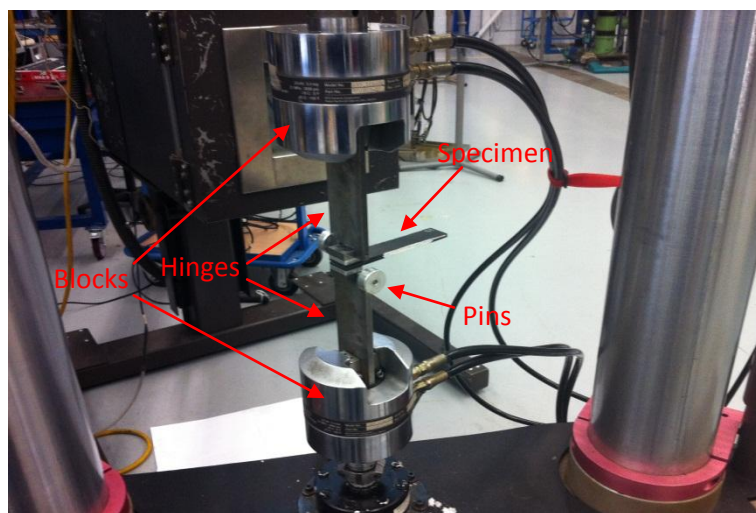


Figure 6.1- DCB test setup example

The crosshead speed was set to be 1 mm/min.

The machine gave as output the values of the applied load  $P$  and the vertical displacement  $\delta$  throughout the test duration (*sec*). Starting from this data a  $P$ - $\delta$  plot can be obtained. In figure 6.2 the plots of the specimens tested are shown.

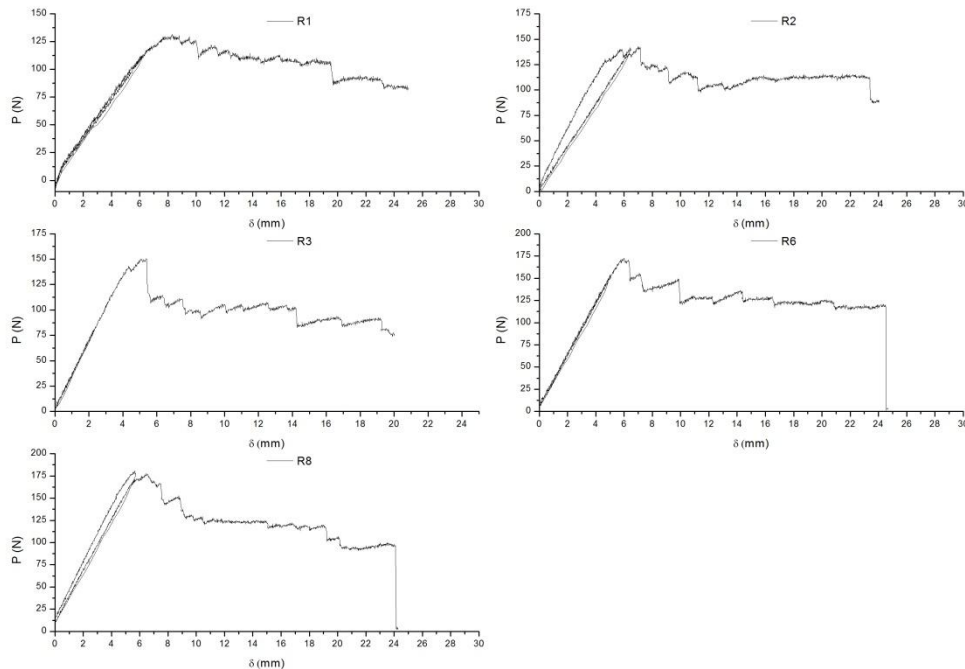


Figure 6.2 -  $P$  vs.  $\delta$  plots, good quality specimens

Each load versus displacement plot consists of two parts:

- a) A first linear part where the load is linearly proportional to the displacement and there is no crack extension during loading proceeds.
- b) A non-linear part during which the crack extends locally or globally and a non-linear material behaviour can be observed.

This behaviour and a local crack growth are responsible for the curve slight deviation from the initial straight line associated to the linear part. It usually happens at the visual crack onset point, which is the point of maximum load as well.

The  $P$ - $\delta$  plots obtained from the tested samples show two different behaviours after they reach the maximum load value. The first one observed is a small load drop after the critical onset point, visible in the load versus displacement plot shown in fig. 6.3 for the R8 specimen. The second behaviour is a large load drop, associable with an unstable crack growth of about 3-7 mm in one step, as happened for example in the load versus displacement plot of the R3 specimen shown in fig. 6.4. In fact in the first case can be observed a load drop of around 17 N, while in the second case the load drop is the double, around 34 N. The corresponding delamination length increased instantly by 4 mm, giving birth to a phenomenon that can be referred as *crack jump*. About the R8 specimen, the increment in delamination length

corresponding to the starting and the ending point of the load drop on the curve is instead of 2 mm.

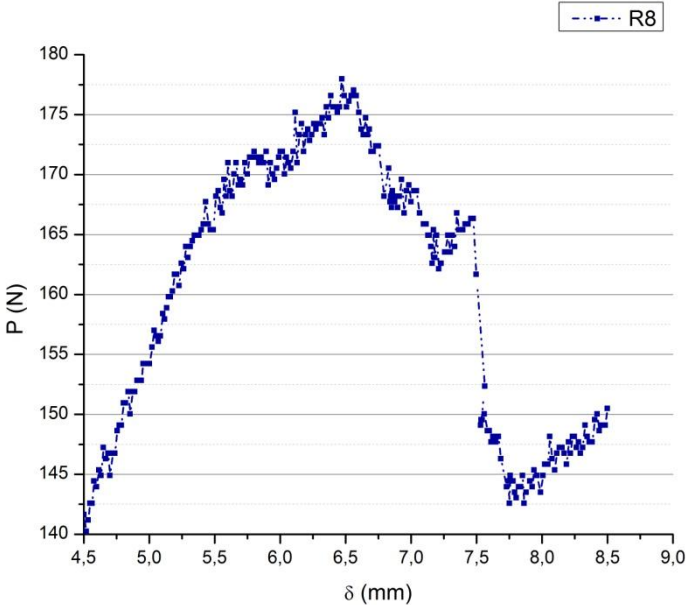


Figure 6.3 - R8 specimen: P vs.  $\delta$  plot, load drop

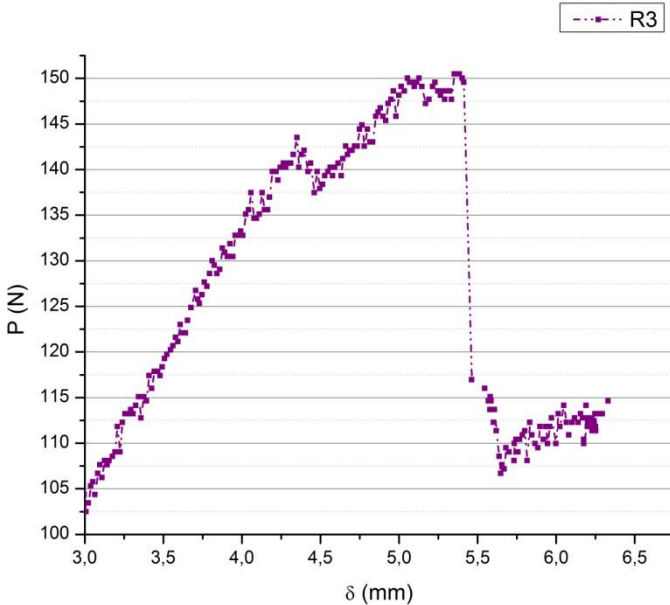


Figure 6.4 - R3 specimen: P vs.  $\delta$  plot, load drop

During the test, a camera placed in front of the specimen recorded the delamination length growth, while a second camera recorded at the same time a picture of the manometer, which

shows the values of load and displacement. In the following figure 6.5 an example of the pictures collected can be seen.

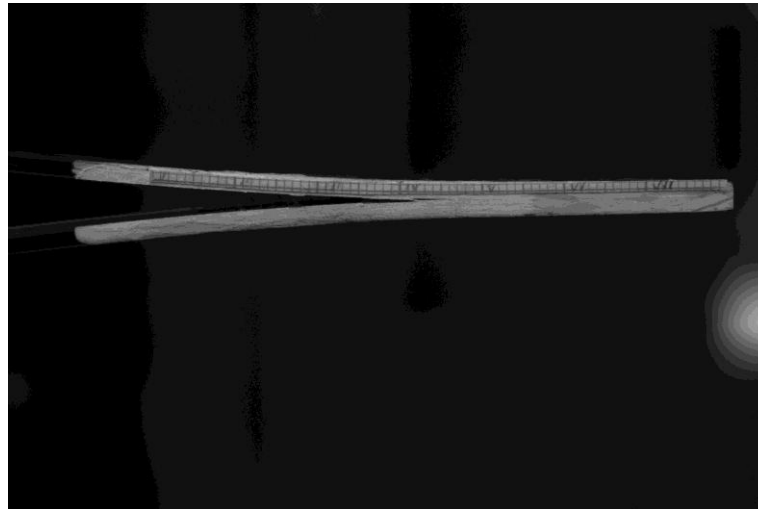


Figure 6.5 - Mode I good quality tests, example picture

Several points (around twenty) were chosen for each specimen among these data, for each of whom a value of delamination length, displacement and load was reported in a table. In table 6.1 an example of the data collected for the R1 specimen.

Pics	Load P	Displ. d	Δa	Length a	Log a	C=d/P	log C	C <sup>1/3</sup>	n	b	G_I_CCM	Δ	12,57521	G_I_MBT
644	118,8	6,586	0	49	1,690196	0,055438	-1,25619	0,381301	2,53	25	807,9651			762,4011
651	126,06	7,166	1,945	50,945	1,707102	0,056846	-1,2453	0,384503		25	897,2285			853,2837
663	129,05	8,165	4,173	53,173	1,725691	0,06327	-1,1988	0,398473		25	1002,706			961,5714
675	126,72	9,166	8,891	57,891	1,762611	0,072333	-1,14067	0,416657		25	1015,23			988,9979
686	111,35	10,144	13,309	62,309	1,794551	0,0911	-1,04048	0,449959		25	917,2742			905,0248
699	120,67	11,171	13,555	62,555	1,796262	0,092575	-1,03351	0,452374		25	1090,385			1076,535
711	116,01	12,18	16,009	65,009	1,812973	0,104991	-0,97885	0,471756		25	1099,815			1092,75
723	109,95	13,182	19,527	68,527	1,835862	0,119891	-0,92121	0,493093		25	1070,201			1072,248
734	109,48	14,117	21,927	70,927	1,850812	0,128946	-0,88959	0,505207		25	1102,595			1110,531
747	108,55	15,117	24,552	73,552	1,866594	0,139263	-0,85616	0,518337		25	1128,89			1143,158
759	106,69	16,178	25,57	74,57	1,872564	0,151636	-0,8192	0,533253		25	1171,21			1188,383
771	106,22	17,192	28,527	77,527	1,889453	0,161853	-0,79088	0,544971		25	1191,874			1216,042
783	105,29	18,194	30,655	79,655	1,901213	0,172799	-0,76246	0,55699		25	1216,894			1246,216
795	106,22	19,213	31,773	80,773	1,907266	0,180879	-0,74261	0,56554		25	1278,456			1311,737
807	89,92	20,2	39,545	88,545	1,947164	0,224644	-0,6485	0,607899		25	1037,992			1077,757
819	91,78	21,215	40,145	89,145	1,950097	0,231151	-0,63611	0,613713		25	1105,21			1148,511
831	92,71	22,218	41,509	90,509	1,956692	0,239651	-0,62042	0,621145		25	1151,57			1198,921
843	88,05	23,214	44,127	93,127	1,969076	0,263646	-0,57898	0,64122		25	1110,591			1160,237
855	83,86	24,219	47,291	96,291	1,983586	0,288803	-0,5394	0,660998		25	1067,274			1119,359
865	83,39	25,023	48,382	97,382	1,988479	0,300072	-0,52277	0,669486		25	1084,239			1138,625
	117,4	6,428		49	1,690196	0,054753	-1,26159	0,379725	2,53	25	779,2887	NL		
	118,8	6,586		49	1,690196	0,055438	-1,25619	0,381301	2,53	25	807,9651	VIS		

Table 6.1 - Good quality quasi-static test collected data: R1 specimen

Through the values of delamination length, displacement and load chosen was possible to obtain the parameters necessary for the data calculation methods used.

First of all the compliance  $C$  was calculated, i.e. the ratio of the displacement and the corresponding load, used in the *Compliance Calibration Method*.

The logarithm of this value together with the one of the delamination length allowed to obtain the  $\log a$ - $\log C$  plot, which gives the value of the  $n$  parameter, used in equation (4.4) in

Chapter 4, i.e. the slope of this plot  $n = \Delta y / \Delta x$ . In table 6.2 are reported the values of  $n$  for each specimen tested.

The following figure 6.6 shows the resultant  $\log a$ - $\log C$  plots for the five specimens. The values were first plotted in a scatter graph, and then a linear trendline was used to obtain a linear fit. The slope of the linear line gave the values of  $n$ .

	<i>R1</i>	<i>R2</i>	<i>R3</i>	<i>R6</i>	<i>R8</i>
<i>n value</i>	2,53	2,45	2,69	2,41	2,67

Table 6.2 - Good quality  $n$  values

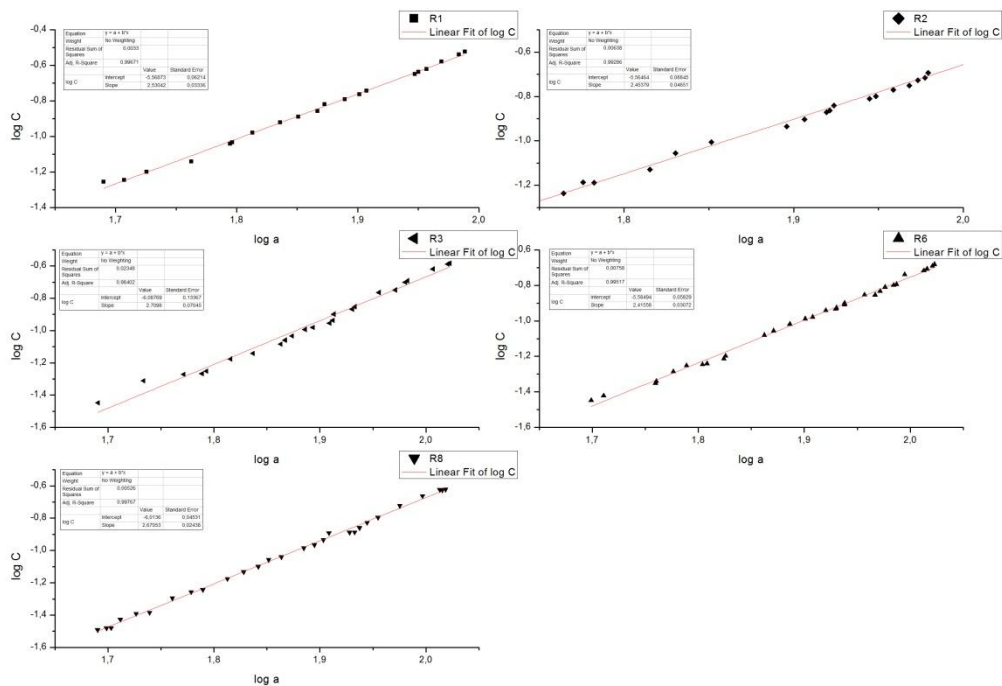


Figure 6.6 - Log C vs. log a good quality plots

The cube root of the compliance was also calculated and plotted versus the delamination length, obtaining so the  $C^{1/3}$ - $a$  plot; it allows to calculate the  $\Delta$  parameter used in equation (4.1) in Chapter 4 as a correction of the overestimate values obtained with the *Modified Beam Theory*.

Table 6.3 shows the values used in the analysis of the five specimens. The following picture 6.7 shows then the plots above mentioned.

	<i>R1</i>	<i>R2</i>	<i>R3</i>	<i>R6</i>	<i>R8</i>
$\Delta$ value	12,58	15,62	6	17,55	8,56

Table 6.3 - Good quality  $\Delta$  values

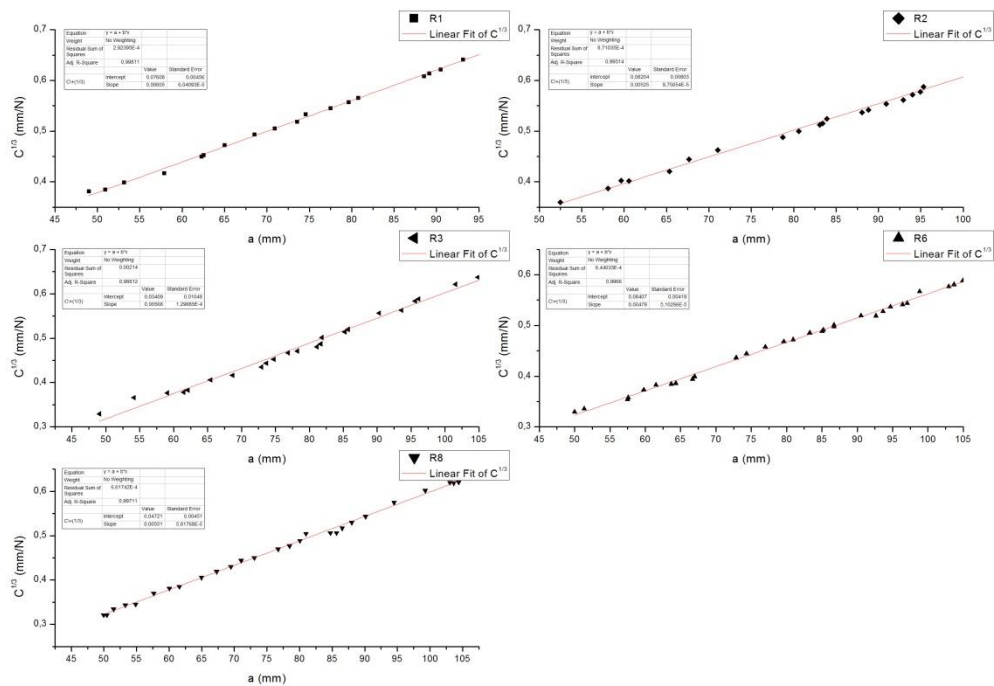


Figure 6.7 -  $C^{1/3}$  vs.  $a$  good quality plots

The next step was to calculate the value of the strain release energy  $G_{Ic}$  using equations 4.4 and 4.1 respectively for the *Compliance Calibration Method* and the *Modified Beam Theory*, using in the specimens' width in addition to the already mentioned data. The obtained values were then used to calculate the *R curve* (resistance curve), i.e. the plot of  $a$  versus  $G_{Ic}$ , which characterizes the onset and propagation values of delamination mechanism.

Below are shown the data given by each method, respectively the *CCM* and the *MBT*, with the related total plots.

Compliance Calibration Method									
R1		R2		R3		R6		R8	
Glc	a	Glc	a	Glc	a	Glc	a	Glc	a
807,9651	49	43,05211	48	852,3913	49,063	984,2223	50	970,9783	49,963
897,2285	50,945	65,61886	49,311	620,2863	54,156	1005,453	51,36	1016,771	50,463
1002,706	53,173	128,1343	51	533,9951	59,094	864,8607	57,499	1194,483	51,481
1015,23	57,891	496,3746	52,5	609,6671	61,5	904,8303	57,598	1153,34	53,296
917,2742	62,309	957,4669	58,111	599,4941	62,083	827,6087	59,778	1118,415	54,87
1090,385	62,555	939,7653	59,667	602,0451	65,437	790,7987	61,518	1046,4	57,648
1099,815	65,009	989,2737	60,578	614,302	68,688	806,1026	63,677	1024,558	60,056
1070,201	68,527	1018,501	65,333	575,0099	72,969	840,6083	64,307	1134,326	61,574
1102,595	70,927	1025,261	67,667	604,1847	73,672	859,3029	66,697	992,6201	64,981
1128,89	73,552	1054,35	71,044	691,8489	74,781	923,0192	66,977	984,4865	67,296
1171,21	74,57	963,2393	78,7	687,3292	76,906	800,4939	72,855	963,7514	69,472
1191,874	77,527	1022,075	80,6	747,533	78,25	901,0798	74,325	955,5924	71,056
1216,894	79,655	1070,214	83,067	744,6834	81,125	948,8152	76,995	1058,823	73,056
1278,456	80,773	1202,051	83,4	813,2292	81,688	1005,099	79,604	1061,997	76,722
1037,992	88,545	1293,102	83,9	870,3749	81,875	1119,107	80,924	1154,869	78,472
1105,21	89,145	1287,472	88,067	858,6012	85,25	1040,387	83,263	1216,797	80,056
1151,57	90,509	1402,006	88,8	876,3393	85,719	1077,612	85,033	1162,776	81
1110,591	93,127	1426,262	90,933	772,0637	90,313	1084,051	85,213	1113,726	84,722
1067,274	96,291	1481,539	92,933	821,0414	93,594	1111,253	86,713	1164,616	85,667
1084,239	97,382	1522,469	94	814,7001	95,625	1139,468	86,713	1238,227	86,556
		1614,73	94,933	885,426	96,125	1094,487	90,552	1260,354	88
		1665,869	95,333	801,9075	101,563	1083,365	92,651	1275,221	90,111
		1224,231	104,067	759,7265	104,875	1142,892	93,671	1152,354	94,5
		1206,431	105,8	771,8435	105,375	1165,032	94,691	1045,022	99,278
						1146,039	96,431	1014,331	103,056
						1244,425	97,091	1109,284	103,667
						1186,835	98,83	1189,398	104,389
						1188,682	102,969		
						1264,327	103,689		
						1309,239	104,949		
						1320,682	105,429		

Tab 6.4 - Good quality SERR values, Compliance Calibration Method

Modified Beam Theory									
R1		R2		R3		R6		R8	
Glc	a	Glc	a	Glc	a	Glc	a	Glc	a
762,4011	49	53,55111	48	847,9967	49,063	906,8483	50	934,0599	49,963
853,2837	50,945	81,70385	49,311	624,4012	54,156	932,8276	51,36	979,539	50,463
961,5714	53,173	159,7398	51	542,7148	59,094	824,8198	57,499	1154,071	51,481
988,9979	57,891	593,8487	52,5	622,1936	61,5	863,286	57,598	1119,785	53,296
905,0248	62,309	917,9729	58,111	612,3978	62,083	796,393	59,778	1090,228	54,87
1076,535	62,555	901,7461	59,667	618,2058	65,437	765,8881	61,518	1026,74	57,648
1092,75	65,009	949,6923	60,578	633,6824	68,688	786,6301	63,677	1010,577	60,056
1072,248	68,527	979,9188	65,333	596,378	72,969	822,0424	64,307	1122,317	61,574
1110,531	70,927	1127,906	67,667	627,1594	73,672	846,8303	66,697	988,4714	64,981
1143,158	73,552	1179,071	71,044	719,0799	74,781	910,4148	66,977	984,3349	67,296
1188,383	74,57	1105,396	78,7	716,0713	76,906	803,0149	72,855	967,04	69,472
1216,042	77,527	1134,403	80,6	779,9071	78,25	907,4018	74,325	961,2168	71,056
1246,216	79,655	1207,398	83,067	779,1954	81,125	961,8438	76,995	1068,216	73,056
1311,737	80,773	1343,146	83,4	851,3828	81,688	1025,138	79,604	1076,846	76,722
1077,757	88,545	1434,14	83,9	911,3734	81,875	1144,792	80,924	1173,658	78,472
1148,511	89,145	1441,093	88,067	901,8495	85,25	1069,62	83,263	1239,018	80,056
1198,921	90,509	1562,3	88,8	920,8623	85,719	1111,921	85,033	1185,353	81
1160,237	93,127	1587,27	90,933	814,408	90,313	1118,969	85,213	1140,164	84,722
1119,359	96,291	1664,477	92,933	868,2554	93,594	1150,447	86,713	1193,478	85,667
1138,625	97,382	1709,229	94	862,8211	95,625	1179,657	86,713	1270,105	86,556
		1808,98	94,933	938,0565	96,125	1141,233	90,552	1294,724	88
		1874,135	95,333	852,664	101,563	1133,807	92,651	1312,739	90,111
		1403,121	104,067	809,4568	104,875	1198,184	93,671	1191,083	94,5
		1360,351	105,8	822,6106	105,375	1223,474	94,691	1084,504	99,278
						1206,934	96,431	1055,743	103,056
						1311,92	97,091	1155,098	103,667
						1254,586	98,83	1239,178	104,389
						1264,203	102,969		
						1346,015	103,689		
						1396,256	104,949		
						1409,378	105,429		

Tab 6.5 - Good quality SERR values, Modified Beam Theory

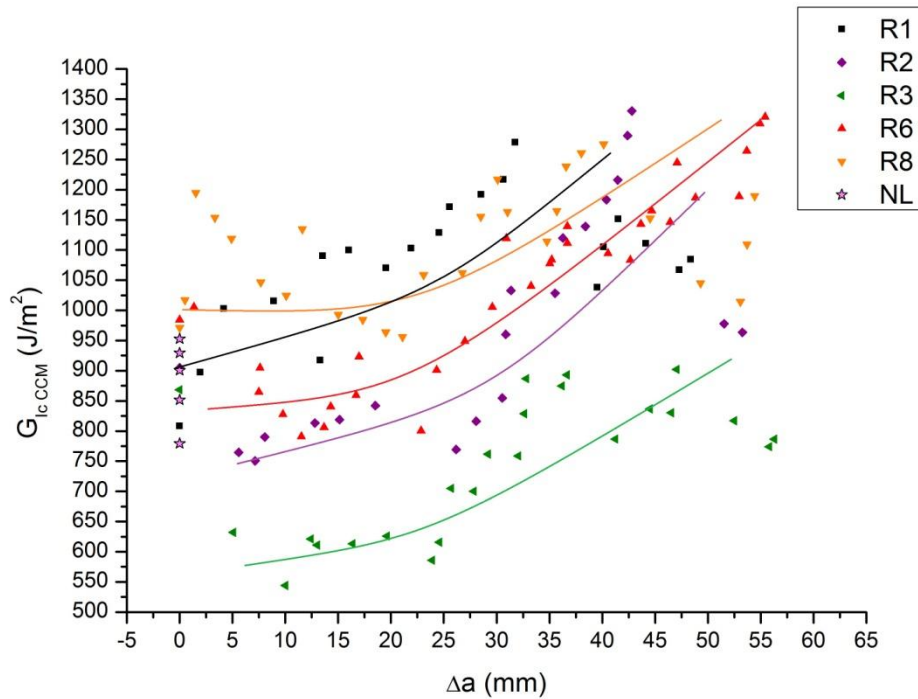


Figure 6.8 -  $G_{Ic\_CCM}$  vs.  $\Delta a$  good quality plots

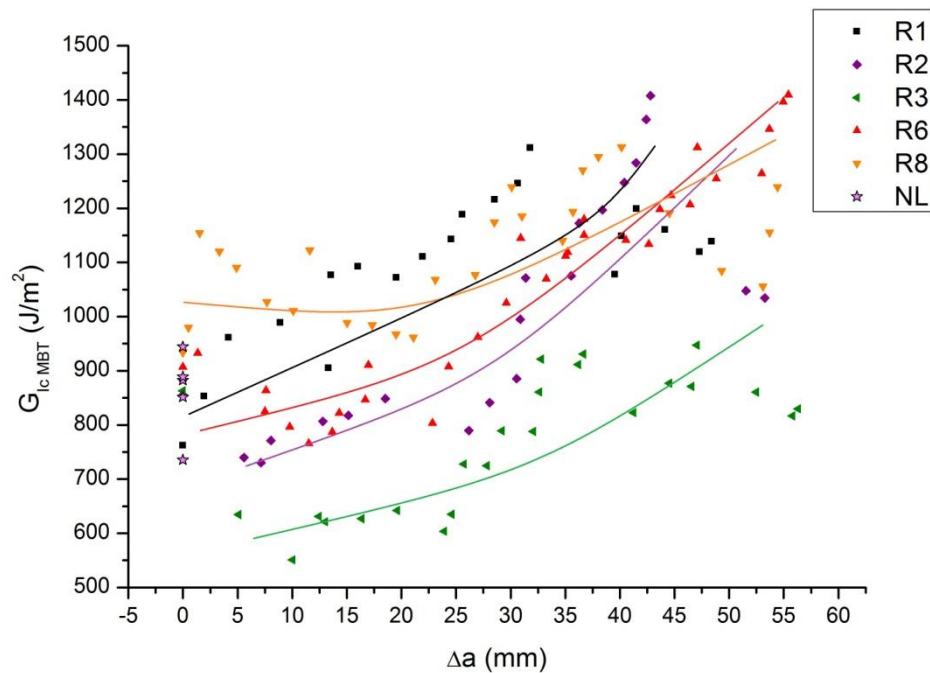


Figure 6.9 -  $G_{Ic\_MBT}$  vs.  $\Delta a$  good quality plots

From a comparison between the values of the two methods of data reduction it can be easily noted that the  $G_{Ic}$  values are more conservative for the *MBT* method; in particular the onset values are smaller, as it is suggested to be by the *ASTM* standard. Figure 6.10 displays the comparison between the onset values deduced respectively with the *CCM* and the *MBT*. A mention about R2 specimen behaviour must be introduced; the first four values showed in

tables 6.4 and 6.5 are calculated after the visual onset of the delamination ahead the insert film, as done for all the specimen tested. But in this case the values obtained are not in agreement as the remaining specimens with the *NL point theory*, whose value is considered the most accurate to define the delamination onset. This value, as previously reported, correspond to the maximum load and recorded in the linear part of the  $P-\delta$  plot, just before the non-linear behaviour is observed. R2 specimen's values just mentioned result substantially lower than the *NL* value, so they were considered inaccurate; the value calculated with the visual method and taken in account as the initial value in this study is then the fifth one, which is higher than the *NL* value, as wanted. What happened ahead the insert film is not clear, because the specimen showed the common aspect shown by all the specimens during the delamination ongoing; the delay in the delamination initiation can be related to material behaviour and properties, such as its micromechanical structure. Figure 6.11 shows the region ahead the insert film which was initially assumed already delaminating. Table 6.6 resumes then all the onset values evaluated with *CCM* and *MBT* data reduction methods, both for visual and *NL* methods.

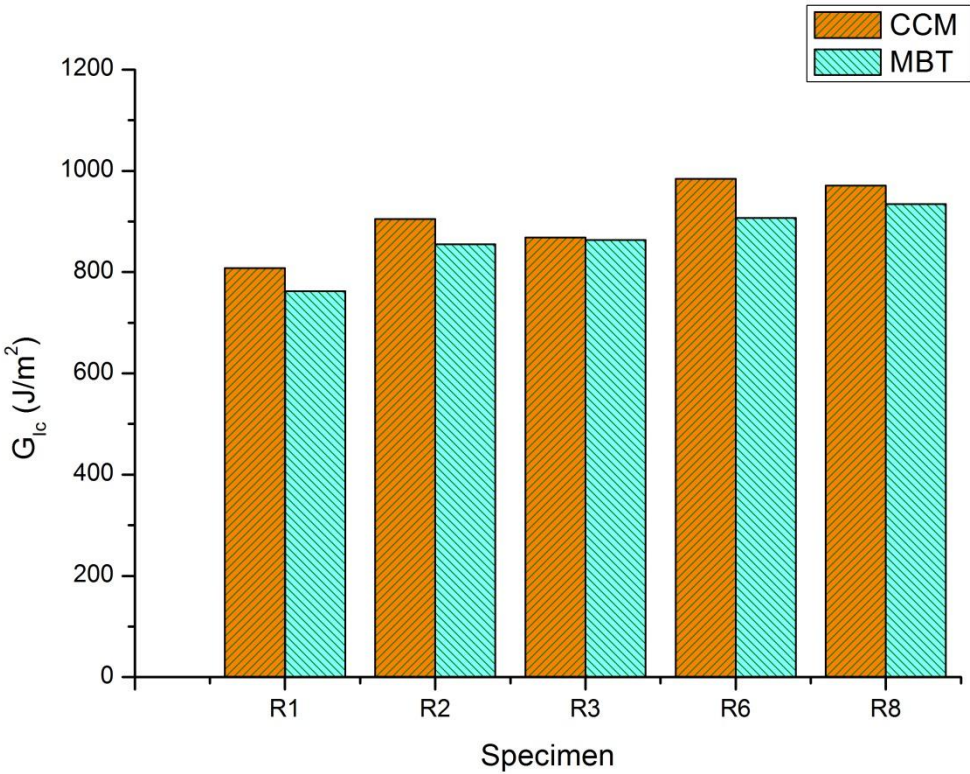


Figure 6.10 -  $G_{1c}$  good quality onset values

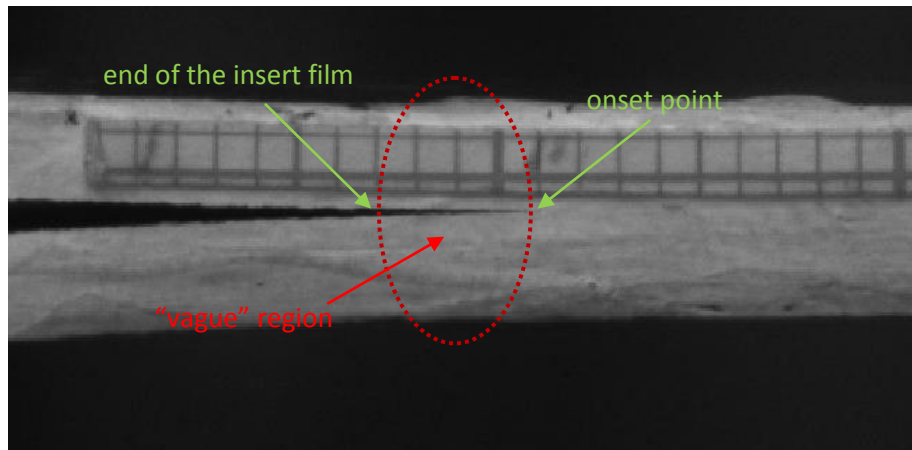


Figure 6.11 - “Vague” region ahead the crack tip

	<i>Visual (J/m<sup>2</sup>)</i>		<i>NL (J/m<sup>2</sup>)</i>	
	<i>CCM</i>	<i>MBT</i>	<i>CCM</i>	<i>MBT</i>
<i>R1</i>	807,97	762,4	779,29	735,34
<i>R2</i>	904,72	855,22	900,69	851,3
<i>R3</i>	868,53	863,1	851,56	844,15
<i>R6</i>	984,22	906,85	952,72	882,32
<i>R8</i>	970,98	934,1	929,36	888,81

Table 6.6 - Good quality  $G_I$  onset values: comparison between Visual and NL

The difference between the results acquired with the two methods can be related to different reasons; the most commonly used to explain the phenomenon is the mutation which occurs at the crack front shape at the crack onset and during the subsequent delamination growth. Indeed just after the end of the insert film the shape of the crack front was perfectly straight but as it started to propagate its shape became undefined; it can be observed in figure 6.12, where in the last part of the delamination region the crack front shape is clearly not straight anymore (before the final failure described further below). This behaviour allows to think that just after the crack started the delamination growth was not homogeneous along the specimen width, resulting in different values of compliance. This introduced a small inaccuracy in the prediction methods used, even in the onset values. In reference [38] an analysis of the theoretical and practical evolution of the crack growth conducts the author to find that the correlation between the cube root of the compliance  $C^{1/3}$  and the crack length is still linear, so that the *SERR* values for crack propagation are accurate both for *CCM* and *MBT* method (fig. 6.13). The comparison between *CCM* and *MBT* method for each specimen confirm the good agreement of the analysis with what the theory suggests. Indeed the initial value evaluated with the *MBT* has to be lower than the one given by the *CCM* method, while during the propagation the second part of the curve furnishes higher values for the *MBT* method, due to the faster decrease in compliance with the delamination length increase.

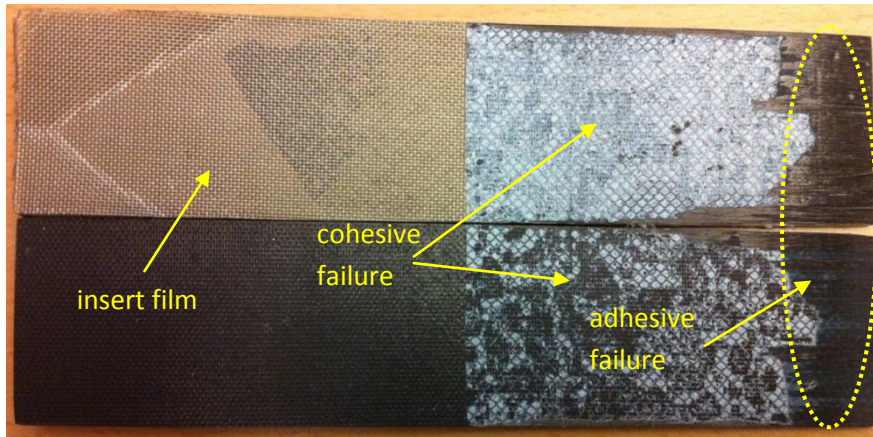


Figure 6.12 - Good quality specimen failure, cohesive vs. adhesive

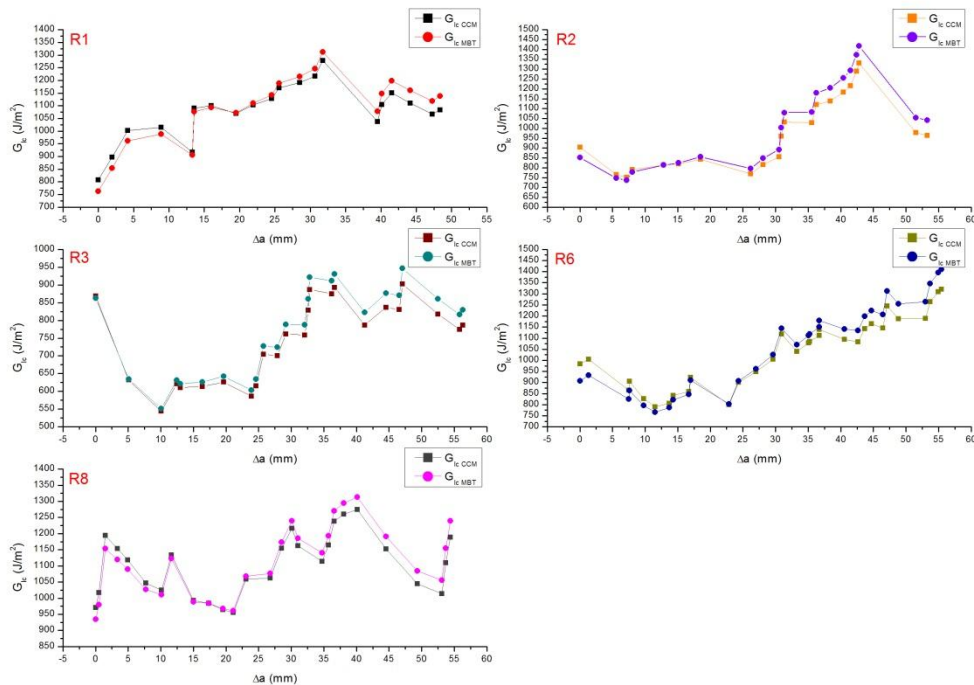


Figure 6.13 -  $G_{Ic}$  vs.  $\Delta a$ : comparison between CCM and MBT, good quality

To verify the validity of the data collected an important step is to evaluate some precision parameters. In particular the *Standard Deviation*, a parameter which permits to judge the goodness of the average values obtained for each batch of specimens.

These average onset values of  $G_I$  are respectively for *CCM* and *MBT*:

$$G_{IcAV(CCM)} = 914,6 \text{ J/m}^2$$

$$G_{IcAV(MBT)} = 873,9 \text{ J/m}^2$$

The value of the *Standard Deviation* of the onset values has been then obtained, resulting respectively for each method:

$$S_{R(CCM)} = 119,99$$

$$S_{R(MBT)} = 119,73$$

Using these previous values, the coefficient of variation can be calculated, which were used later to compare the acceptability of the results with the reference values furnished by the literature. Their percentage values are respectively as above:

$$(CV)_{R(CCM)} = 13,1 \%$$

$$(CV)_{R(MBT)} = 13,3 \%$$

obtained from the ratio of the standard deviation and its corresponding average value of  $G_{Ic}$ . Considering the reference value of 16,5 % furnished by the *ASTM* Standard for a Kapton insert of 13  $\mu\text{m}$  it can be seen that the values obtained are well comparable, considering that the insert film used here is slightly different, being a Teflon one.

The reliability of the data it has been also checked evaluating the ratio of the vertical displacement of the loading point and the delamination length at the delamination onset, also indicated as *opening displacement* ( $\delta/a$ ). The standard procedure previously reported suggests it to be minor than 0,4. The values obtained for each specimen result to be sufficiently below this value, being them around 0,13÷0,3.

Another important phenomenon to remark is the so called *fibre bridging*. To explain this phenomenon it has to be considered that delamination cracks often interact with misaligned or inclined fibres. This interaction leads to the *fibre bridging*, which provokes an increase of the nominal delamination resistance as the crack extends. In fact, in general delamination cracks present trajectories dominated by the matrix, but crack path instabilities and imperfect fibres alignment cause the referred interactions. They have a good effect since they lead to suppress delamination, but on the other hand they also cause a dependence of delamination resistance on the geometry of the specimen and on its loading mix. Considering this lack of uniqueness it results complicate to design the delamination resistance of the material. One of the direct consequences is indeed the previously called *crack jump*, which is of main interest in this report since it took place in several specimens during the tests. It can be described as an instantaneous increase of the crack length, due to a progress of the crack tip faster than the usual. In fig. 6.14 can be seen from one side the detail of the presence of a *crack bridging* along the delamination path, which led successively to a *crack jump*. The phenomenon can be explained considering that the fibres that interact with the crack exert bridging tractions, which represent the major source of non-linear behaviour of the delamination growth, visible in particular through the significant non-linearity of the  $P-\delta$  curve prior to first crack propagation. In reference [39] an analytical method to estimate such behaviour is furnished, based on a traction law for three different bridging responses: linear elastic, “perfectly plastic” and strain softening bridging. Each case reaches the same maximum traction and the same steady-state resistance. Each mechanism has the double effect to affect the shape of the R-curve and to result in different magnitudes of bridging traction. For example fibres deforming elastically have a strain to failure smaller than 1%, which results in a high closure force over a small displacement, while fibres coming off from a crack face give smaller closure forces, but act over a greater displacement range.

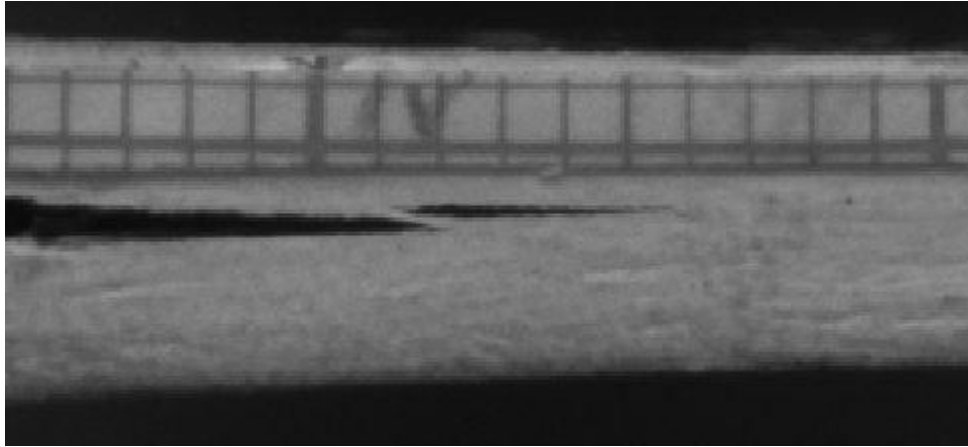
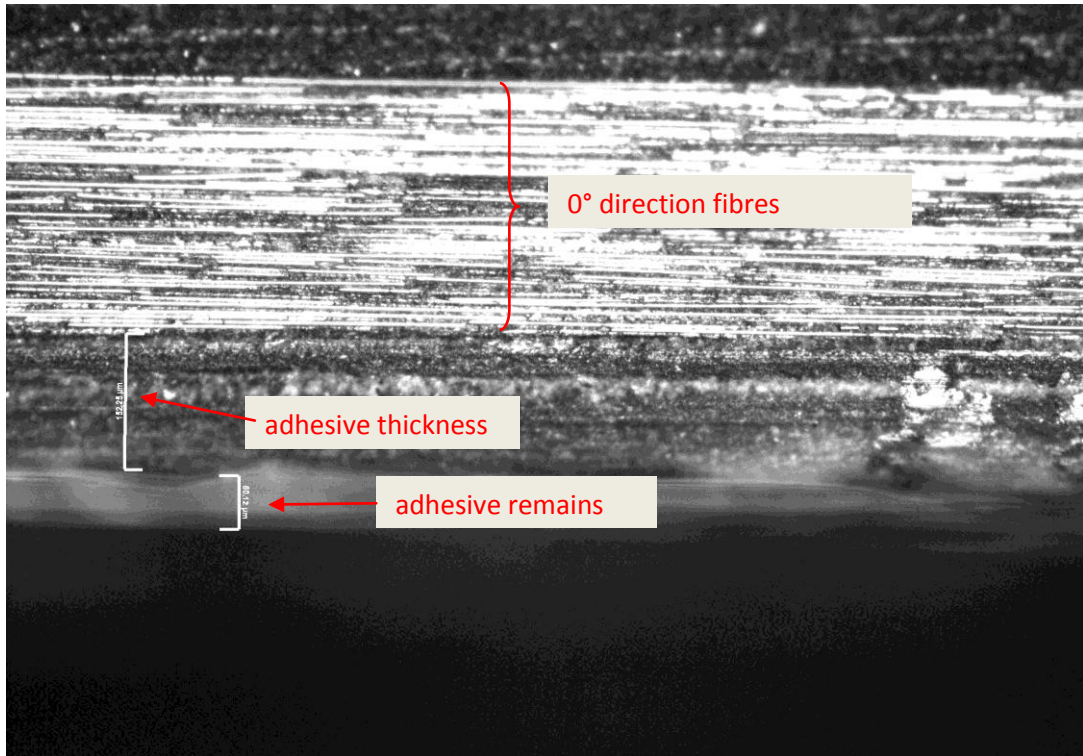


Figure 6.14 - Good quality specimen, fibre bridging example

Some specimens reached the final failure during the test, in particular R6 and R9 specimens broke. From a visual inspection of R6 specimen (figure 6.12) can be noted a white region, corresponding to the standard delamination growth, until a certain point at the end of the specimen, where the aspect changes. Indeed since that point a *cohesive failure* can be visualized, while in the final region the adhesive seems not able anymore to stick to the upper surface, giving life to an *adhesive failure* which led to the final fracture of the specimen.

After have verified the effective presence of the carrier in the adhesive used, to understand the reason of this event an inspection with the optical microscope was carried on. It showed that the thickness of the adhesive was correct, i.e. around 0,15 mm, as can be seen in figure 6.15. The brighter region seen from one side of the specimen represents the outer layers of the analysed lamina since can be easily identified the fibres oriented in  $0^\circ$  direction. The region just below represents the adhesive, whose thickness measured by the microscope is around 0.15 mm, so it stays within the range of thickness for this adhesive reported in *Chapter 3* (0,15 – 0,30 mm), considering that here the adhesive thickness is affected by the pressure applied during the cure cycle. Finally, the lower region shown in the picture represents the remains of the adhesive epoxy along the crack path which was observed from another point of view (the white region) in the previous figure 6.12.



*Figure 6.15* - Optical microscope inspection of adhesive, good quality material

### 6.1.2 Poor Quality Material

Proceeding with the layout already followed previously describing the results for the *good quality* material, the plots of  $P$ - $\delta$  data are illustrated in figure 6.16.

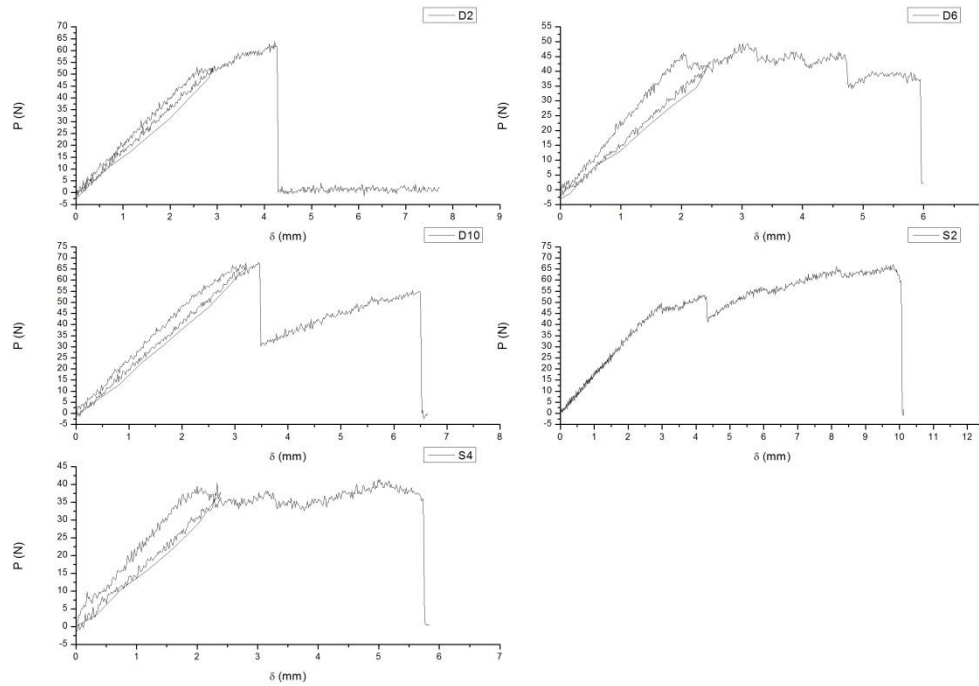


Figure 6.16 -  $P$  vs.  $\delta$  plots, poor quality specimens

Some considerations can easily be appointed.

It is visible that the crack length increased during the loading/unloading/reloading process; in particular in specimens D6 and S4 this behaviour is visually clear.

Related to the load drops, for each specimen tested this phenomenon can be noted during the delamination propagation. In specimens D2 and D10 the drop results to be rather evident; in the first case the load applied following the drop seems to stabilize around a constant value, while in the second case the load starts to increase again until the ultimate fracture drop, as happens after the smaller drops visible in specimens D6 and S2 curves.

The reason of the final drops in the load of the curves is found in the ultimate fracture occurred to all the specimens tested. In particular the D2 and D10 ended on separating in the two composing laminae, while the others stopped just a few millimetres before that. In figure 6.17 the final state of the specimens is exhibited clockwise.

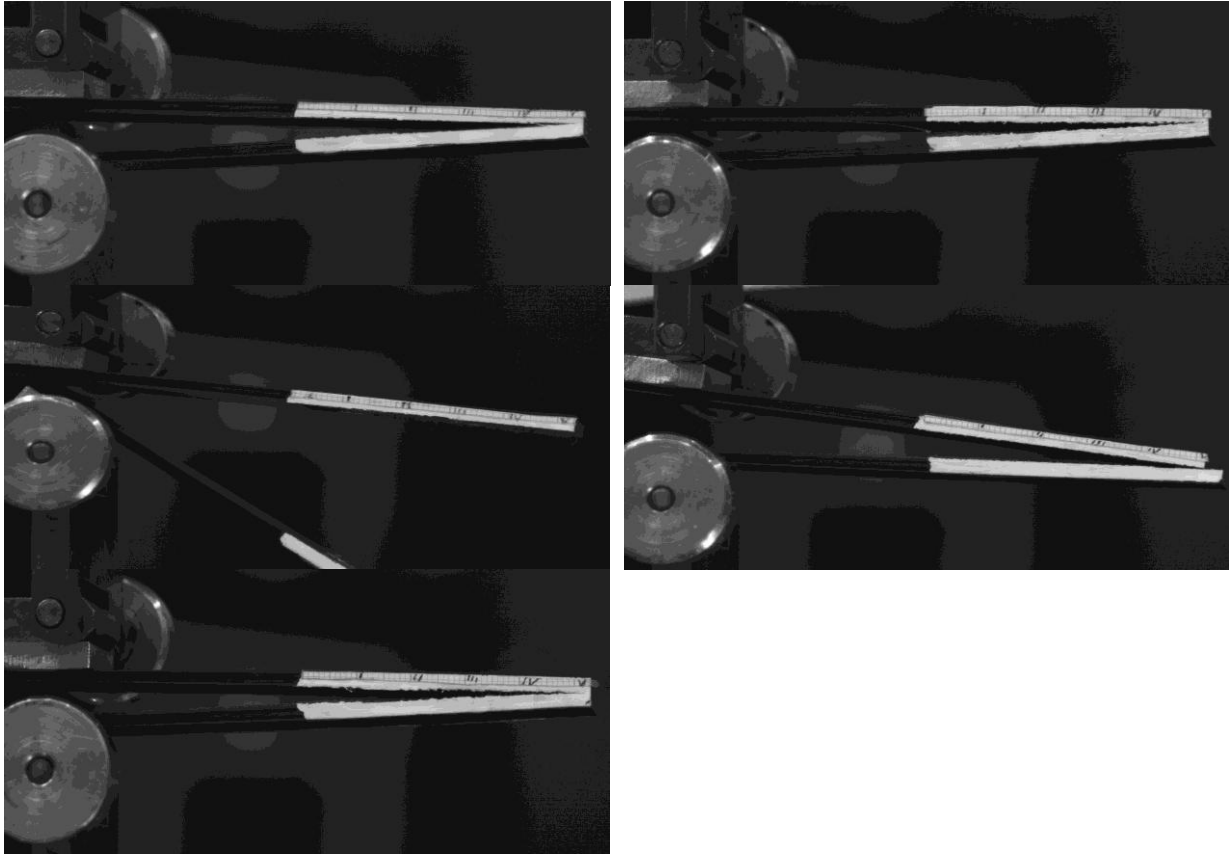


Figure 6.17 - Poor quality specimens, mode I test final state

For each specimen a table was filled choosing a variable number of relevant points in the delamination growth study. The variability of the number of points is due to the duration of the test; in fact four of them were very quick, reaching the final fracture or a final load drop after a vertical displacement of 4 – 6 mm. Just specimen S2 reached a displacement of around 10 mm during the test, so it represents the one which allowed to collect more points, while specimen D10 for example allowed to collect just a few points. Table 6.7 shows the data for S2 specimen.

Pics	Load P	Displ. d	Increm Δa	Length a	Log a	C=d/P	log C	C <sup>1/3</sup>	n	b	G_I_CCM	Δ	45,12596	G_I_MBT
279	10,25	0,553	0	47,558	1,677224	0,053951	-1,268	0,377862	1,69	25	4,028488			3,669405
280	11,18	0,636	1,404	48,962	1,689859	0,056887	-1,24498	0,384596		25	4,908587			4,534361
285	18,17	1,061	2,44	49,998	1,698953	0,058393	-1,23364	0,38796		25	13,0327			12,15995
287	21,43	1,227	5,391	52,949	1,723858	0,057256	-1,24218	0,385426		25	16,78517			16,08644
291	27,02	1,561	10,509	58,067	1,763929	0,057772	-1,23828	0,38658		25	24,55136			24,52389
298	37,27	2,146	12,532	60,09	1,778802	0,05758	-1,23973	0,386151		25	44,98872			45,60986
309	44,73	3,061	14,204	61,762	1,790721	0,068433	-1,16474	0,40903		25	74,93032			76,85722
319	51,25	3,902	19,822	67,38	1,828531	0,076137	-1,11841	0,423836		25	100,3152			106,649
322	54,04	4,153	23,44	70,998	1,851246	0,07685	-1,11435	0,425157		25	106,8434			115,9596
324	41,93	4,32	28,724	76,282	1,882422	0,103029	-0,98704	0,468799		25	80,26075			89,51848
330	47,52	4,818	33,675	81,233	1,909732	0,101389	-0,99401	0,466298		25	95,2637			108,7147
370	64,76	8,16	35,341	82,899	1,918549	0,126004	-0,89962	0,501335		25	215,4589			247,6587
380	62,9	9,003	37,103	84,661	1,927683	0,143132	-0,84426	0,523093		25	226,0847			261,793
391	64,29	9,918	39,989	87,547	1,942241	0,15427	-0,81172	0,536324		25	246,1744			288,3609
392	61,5	10,001	42,863	90,421	1,956269	0,162618	-0,78883	0,545828		25	229,9143			272,2576

Table 6.7 - Poor quality quasi-static test collected data: S2 specimen

From the data collected the usual parameters were obtained, in order to calculate the values of the toughness using again both *CCM* and *MBT* methods.

The plots of  $\log a$  versus  $\log C$  permitted to calculate the values of the  $n$  parameter used in *CCM* data reduction method. Fig. 6.18 displays the plots while in the following table 6.8 the values of  $n$  for each specimen are reported.

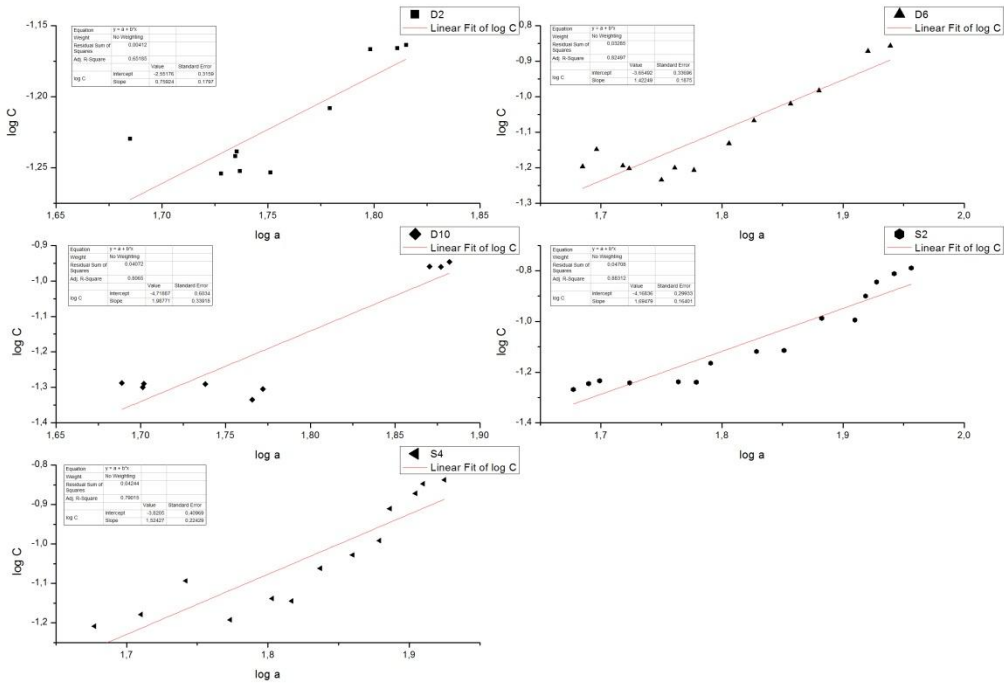


Figure 6.18 - Log C vs. log a poor quality plots

	D2	D6	D10	S2	S4
<i>n</i> value	0,75	1,42	1,96	1,69	1,52

Table 6.8 - Poor quality  $n$  values

The range appears rather acceptable, except for the value in specimen D2, where the data points were affected by the load drop occurred after 4 mm of applied displacement, causing a large scatter in the plot which carried to a value of  $n$  slightly minor.

The plots of  $a$  versus  $C^{1/3}$  are exhibited in figure 6.19. The linear fitting of the points allowed to calculate the  $\Delta$  parameters used to estimate the *IFT* with the *MBT* method, reported in table 6.9.

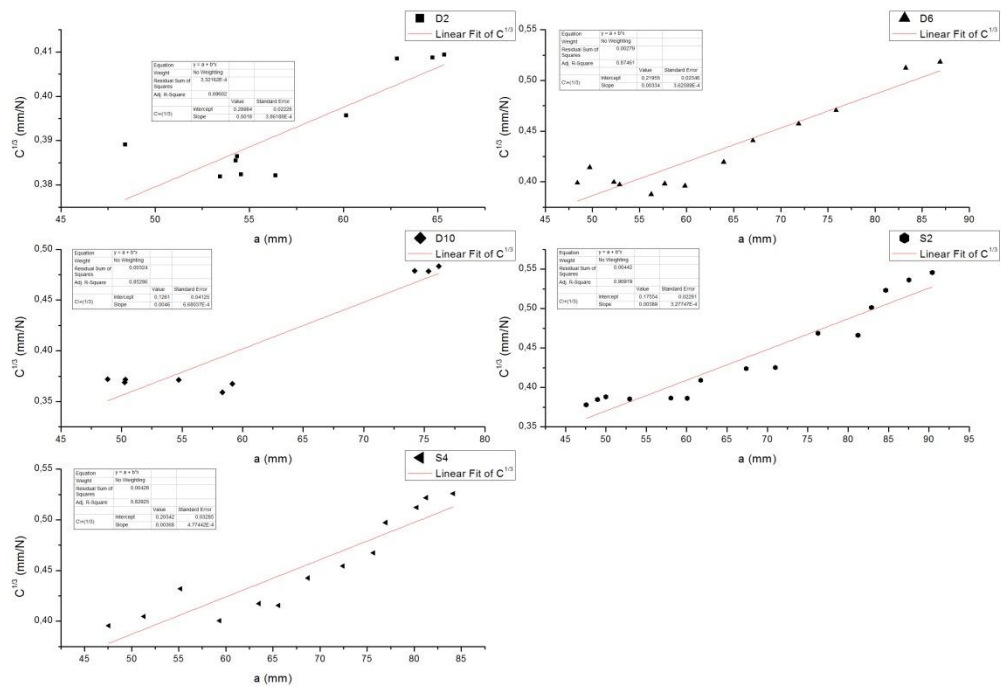


Figure 6.19 -  $C^{1/3}$  vs. a poor quality plots

	D2	D6	D10	S2	S4
$\Delta$ value	161,02	65,73	26,8	45,12	55,27

Table 6.9 - Poor quality  $\Delta$  values

The motivation just adducted above to explain the behaviour of D2 in the plots used to find  $n$  can be also readopted here to explain the value of  $\Delta$  obtained for the same specimens, which results one order bigger than the  $\Delta$  values for the other four specimens.

Even presenting a so large scatter, the acquired values of  $\Delta$  permitted to find out results very close to those found out with the *CCM* method. For each specimen tested the results found seem to agree, as can be checked in tables 6.10 and 6.11 and confirmed in figures 6.20 and 6.21. A comparison between the values deduced with the two methods will be later presented (fig. 6.22).

Compliance Calibration Method									
D2		D6		D10		S2		S4	
G <sub>I</sub>	a	G <sub>I</sub>	a	G <sub>I</sub>	a	G <sub>I</sub>	a	G <sub>I</sub>	a
7,67242	48,415	5,05704	48,415	2,295386	48,856	4,02849	47,558	3,78172	47,564
9,52885	53,441	5,50945	49,724	3,402015	50,248	4,90859	48,962	5,32872	51,309
14,07573	54,277	11,46158	52,271	11,8817	50,32	13,0327	49,998	6,02574	55,201
19,97334	54,356	26,30925	52,89	15,43718	54,711	16,78517	52,949	27,45197	59,346
34,03714	54,553	43,99082	56,246	31,23912	58,318	24,55136	58,067	39,14563	63,528
39,68416	56,389	52,20963	57,674	99,27758	59,157	44,98872	60,09	43,86947	65,6
53,23497	60,139	65,25066	59,817	145,8061	61,164	74,93032	61,762	46,82798	68,728
55,1743	62,843	66,96608	63,934	58,26954	74,188	100,3152	67,38	50,64079	72,437
58,0496	64,718	66,60395	67,053	102,4074	75,34	106,8434	70,998	51,39567	75,673
59,55757	65,349	69,34037	71,885	158,4104	76,196	80,26075	76,282	70,85464	76,982
		73,15354	75,883			95,2637	81,233	76,11054	80,255
		57,50368	83,262			215,4589	82,899	75,70717	81,273
		71,34471	86,904			226,0847	84,661	78,55654	84,146
						246,1744	87,547		
						229,9143	90,421		

Table 6.10 - Poor quality SERR values, Compliance Calibration Method

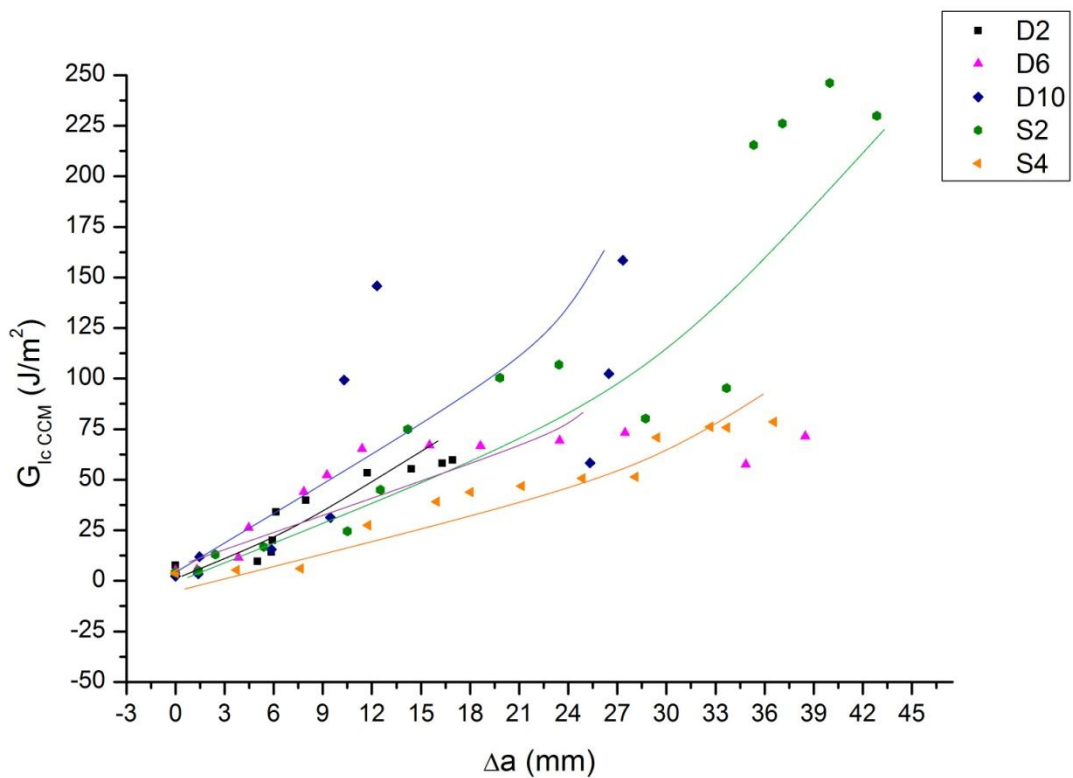


Figure 6.20 -  $G_{Ic\_CCM}$  vs.  $\Delta a$  poor quality plots

Modified Beam Theory									
D2		D6		D10		S2		S4	
G <sub>I</sub>	a	G <sub>I</sub>	a	G <sub>I</sub>	a	G <sub>I</sub>	a	G <sub>I</sub>	a
7,09444	48,415	4,53146	48,415	2,268613	48,856	3,6694	47,558	3,45206	47,564
9,49778	53,441	5,01286	49,724	3,395662	50,248	4,53436	48,962	5,06283	51,309
14,19398	54,277	10,72605	52,271	11,86542	50,32	12,15995	49,998	5,94236	55,201
20,16305	54,356	24,78244	52,89	15,85839	54,711	16,08644	52,949	28,05242	59,346
34,45346	54,553	42,85482	56,246	32,75775	58,318	24,52389	58,067	41,31338	63,528
41,17083	56,389	51,5492	57,674	104,5708	59,157	45,60986	60,09	46,98937	65,6
57,90342	60,139	65,6786	59,817	155,1679	61,164	76,85722	61,762	51,22441	68,728
61,95368	62,843	69,75709	63,934	65,51556	74,188	106,649	67,38	56,68909	72,437
66,56951	64,718	71,0554	67,053	115,6113	75,34	115,9596	70,998	58,61909	75,673
68,77248	65,349	76,52096	71,885	179,3638	76,196	89,51848	76,282	81,39718	76,982
		82,81306	75,883			108,7147	81,233	88,95127	80,255
		67,88942	83,262			247,6587	82,899	88,93418	81,273
		85,81695	86,904			261,793	84,661	93,57472	84,146
						288,3609	87,547		
						272,2576	90,421		

Table 6.11 - Poor quality *SERR* values, Modified Beam Theory

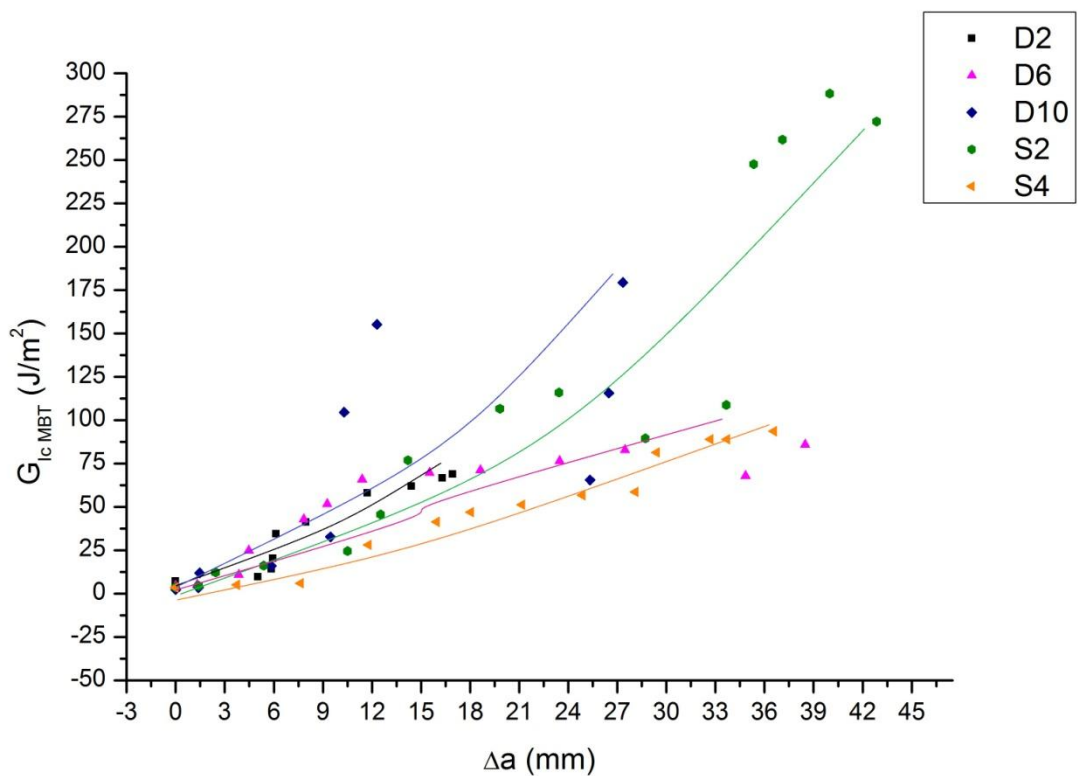


Figure 6.21 -  $G_{Ic\_MBT}$  vs.  $\Delta a$  poor quality plots

The results respect moreover what suggested in literature, i.e. the more conservative nature of the onset value found with the *MBT* method. All five specimens furnished an higher onset value calculated with the *CCM* method compared with the one calculated with the *MBT* method (fig. 6.22), while during the propagation the values given by *MBT* method become higher, as can be confirmed by the comparison plot displayed in figure 6.23.

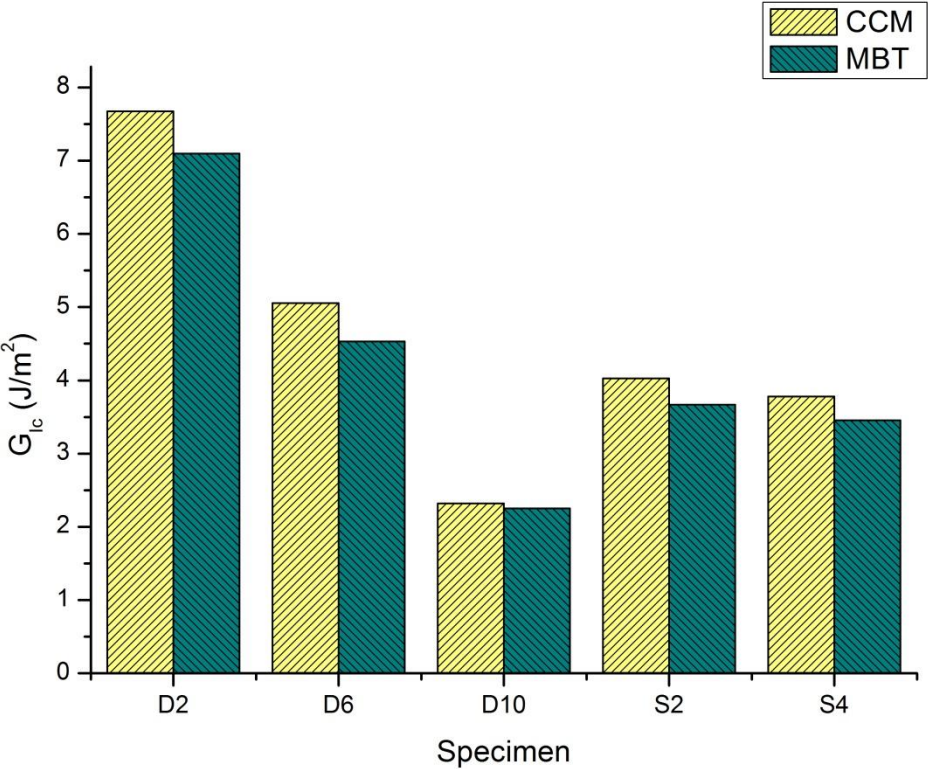


Figure 6.22 -  $G_{Ic}$  poor quality onset values

For the *poor* quality here presented the check of the onset values obtained by the *NL* method was not considered reliable, since the values given by such method were retained too high. In fact they are situated within a range of values where the delamination is unmistakable ongoing, as can be confirmed by the pictures grabbed by the camera which show the delamination tip proceeding. Plus, the values mentioned are higher than the maximum one obtained for some specimens (D2, D6, D10), while for the remaining are around the value recorded just before the end of the test, happened for the various reasons above described, such as final fracture or extended crack jump. This result well adhere to the difficulties met during the data processing of the *poor* quality data, due to its really poor quality which led to behaviours sometimes difficult to be interpreted, like for example the quick duration of the tests or the continuous crack jumps. For the sake of knowledge the *NL* values are however reported in table 6.12.

	<i>NL (J/m<sup>2</sup>)</i>	
	<i>CCM</i>	<i>MBT</i>
<i>D2</i>	83,47	77,18
<i>D6</i>	88,32	79,14
<i>D10</i>	184,79	182,64
<i>S2</i>	160,12	145,85
<i>S4</i>	78,43	71,59

Table 6.12 - Poor quality  $G_I$  onset values: NL

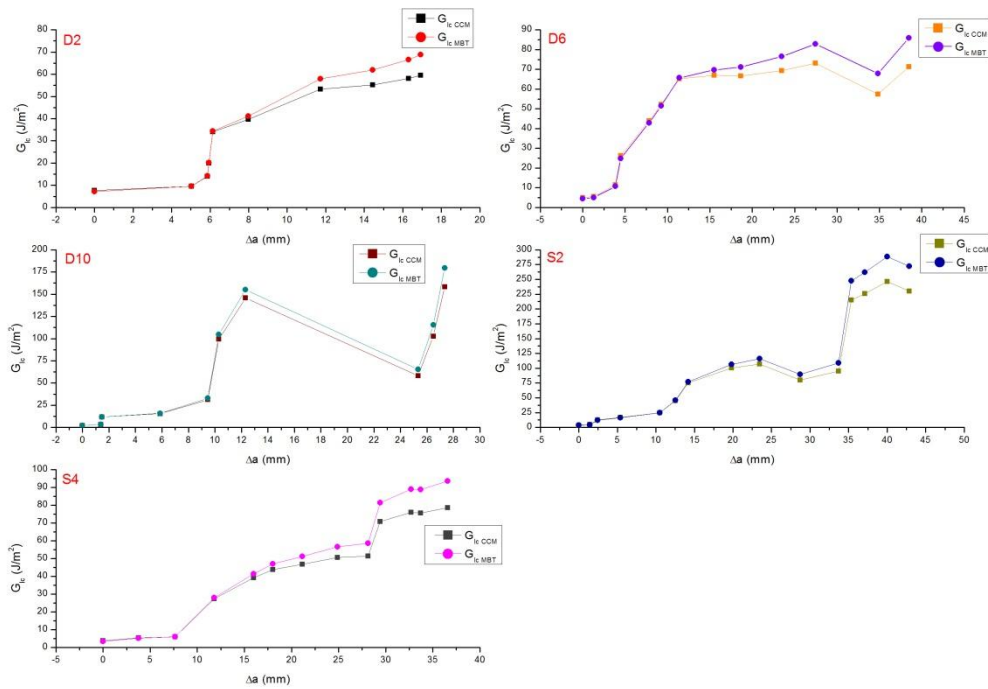


Figure 6.23 -  $G_{Ic}$  vs.  $\Delta a$ : comparison between CCM and MBT, poor quality

The precision parameters were considered. The average onset values obtained with *CCM* and *MBT* are respectively:

$$G_{IcAV} = 4,57 \text{ J/m}^2$$

$$G_{IcAV} = 4,2 \text{ J/m}^2$$

The value of the *Standard Deviation* of the onset values for each specimen are respectively for each method:

$$S_{R(CCM)} = 1,99$$

$$S_{R(MBT)} = 1,81$$

The coefficient of variation calculated using the previous values expressed in percentage are as above:

$$(CV)_{R(CCM)} = 43,72\%$$

$$(CV)_{R(MBT)} = 42,99\%$$

The latter are visibly in disagreement with the values given as reference in the *ASTM* standard already reported in the previous paragraph.

The *opening displacement* resulted to be abundantly below the value of 0,4 given by the *ASTM* reference, being around 0,02 – 0,07.

*Fibre bridging* phenomenon was observed in many cases during the tests. In some cases it represented the cause for subsequent *crack jumps*, as can be seen in fig. 6.24. The picture shows indeed the delamination growth in S4 specimen; the *fibre bridging* highlighted in it preceded a *crack jump* occurred at 11 mm of length ahead the crack tip, which increased the crack length until 28 mm followed by a *load drop*, as visible in the relative *P-δ* plot around 11 N. A *load drop* is the event noted to happen every time a *crack jump* took place; it is easily provable examining the data table for each specimen and its related load versus displacement plot.

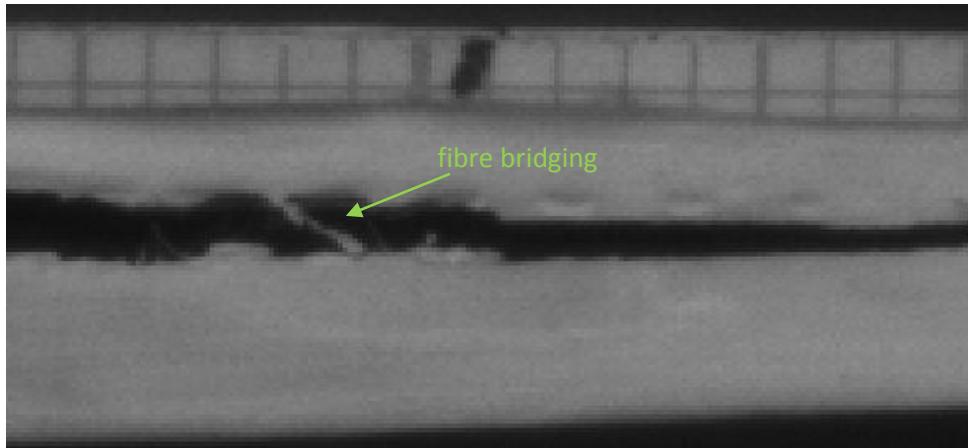
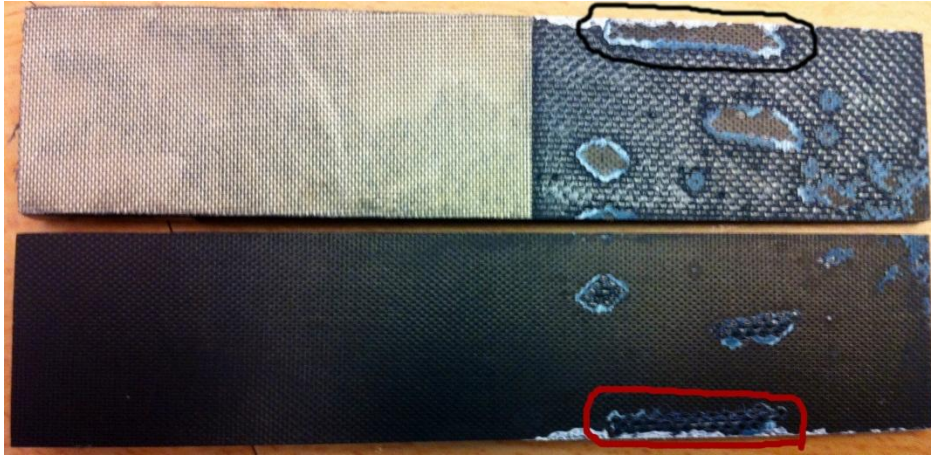


Figure 6.24 - Poor quality specimen, fibre bridging example

*Crack jumps* could be analysed through the broken specimens. For example in specimen D10 a *crack jump* occurred after 12,3 mm of delamination growth ahead the crack tip, leading the length to 25,3 mm; from a first visual inspection of the bonding surfaces after the test in the mentioned region can be observed (fig 6.25) that an *adhesive failure* took place, inducing the delamination to grow by 13 mm instantaneously.



*Figure 6.25 - Poor quality specimen failure, adhesive failure*

## 6.2 Fatigue Mode I Interlaminar Fracture Toughness test

Fatigue tests were conducted on the two different qualities of material to study mode I fatigue delamination. The aim was to provide information about the material behaviour to be used in fatigue life prediction of the laminates. In particular were obtained *fatigue curves*, which provide the variation of the fatigue parameter  $\Delta G_{\sqrt{}}$  versus the elapsed number of cycles  $N$ , and *crack growth rate curves* representing the crack growth rate per cycle  $da/dN$  versus the variation of *SEERR*, chosen to be  $\Delta G_{\sqrt{}} = (\sqrt{G_{max}} - \sqrt{G_{min}})^2$  in the previous *Chapter 4*.

Both for *good* and *poor* quality the tests were performed using the same machine adopted for the quasi-static tests, i.e. the *MBT 10kN Elastomer*. The tests were carried out in displacement control, set in order to obtain and maintain a constant stress ratio  $R=0,1$ . The frequency of the stress cycle was set to 5 Hz.

The machine gave as output the history of applied load, both maximum and minimum, applied displacement (max and min), elapsed number of cycles, actual time and seconds from the beginning. Using these data a table could be created for each specimen as done for the static tests, which allowed to calculate various parameters, such as the *R-ratio*, the displacement ratio and the compliance.

For the chosen cycles a visual length of the delamination was deduced helped by the *ImageJ* software. The values of the crack length allowed to calculate the values of the crack growth rate as  $da/dN$ , where  $da$  is the difference between two subsequent values of the delamination length  $a$  and  $dN$  the difference between two subsequent cycles  $N$  considered. For each point examined the values of *SEERR* ( $G_{I_{max}}$  and  $G_{I_{min}}$ ) were evaluated using the *CCM* method:

$$G_{I_{max}} = \frac{n_{av} P_{max} \delta_{max}}{2ba}$$

$$G_{I_{min}} = \frac{n_{av} P_{min} \delta_{min}}{2ba}$$

The value of  $n$  considered in the formulas has been calculated as the average value of those given by the static tests. The increment in *SEERR*  $\Delta G = G_{I_{max}} - G_{I_{min}}$  was then obtained for each point considered and so the corresponding fracture parameter  $\Delta G_{\sqrt{}} = (\sqrt{G_{max}} - \sqrt{G_{min}})^2$ .

From the above data three main plots were obtained. In fact a plot showing the relation between the fracture toughness and the increment of crack length (*fatigue R curves*) has been reached in addition to the mentioned *fatigue curves* ( $\Delta G_{\sqrt{}} - N$ ) and the *crack growth rate curves* ( $da/dN - \Delta G_{\sqrt{}}$ ).

### 6.2.1 Good Quality Material

As done in the previous section for static tests, it will be shown just the resultant plot for each type just introduced, displaying the total results for the whole five specimens tested.

Table 6.13 gives an example (specimen L4) of the tables created to elaborate the data collected by the machine.

Cycle	P <sub>min</sub>	P <sub>max</sub>	R	δ <sub>min</sub>	δ <sub>max</sub>	R	C	da	dN	da/dN (secant)	Pics	a	da/dN (polynomial)	G <sub>max</sub>	G <sub>min</sub>	ΔG	Loga	LogC	Δa	ΔGv	
num	N	N		mm	mm			mm		mm/ciclo	#	mm	mm/ciclo	J/m <sup>2</sup>	J/m <sup>2</sup>	J/m <sup>2</sup>			mm	J/m <sup>2</sup>	
0								0,00	1			45,00									0,00
100	1,397	133,24	0,01	0,21	5,91	0,04	0,04	10,29	100	1,03E-01	172	55,29		726,07	0,27	725,80	1,74	-1,35	10,29	698,31	
700	16,306	123,00	0,13	0,81	5,91	0,14	0,05	0,14	600	2,28E-04	179	55,43		669,02	12,21	656,81	1,74	-1,32	10,43	500,45	
2000	12,579	110,42	0,11	0,83	5,93	0,14	0,05	1,73	1300	1,33E-03	192	57,16	0,001498131	584,43	9,33	575,10	1,76	-1,27	12,16	446,10	
4500	11,647	101,10	0,12	0,82	5,92	0,14	0,06	1,51	2500	6,04E-04	217	58,67	0,000706067	520,46	8,26	512,20	1,77	-1,23	13,67	397,57	
8500	10,715	95,04	0,11	0,83	5,85	0,14	0,06	1,45	4000	3,63E-04	257	60,12	0,000423785	471,91	7,52	464,39	1,78	-1,21	15,12	360,30	
14200	10,249	89,45	0,11	0,85	5,90	0,14	0,07	0,82	5700	1,44E-04	269	60,94	0,000189564	441,59	7,27	434,32	1,78	-1,18	15,94	335,52	
20200	8,386	86,19	0,10	0,85	5,90	0,14	0,07	1,24	6000	2,06E-04	281	62,18	0,000110727	416,97	5,83	411,14	1,79	-1,16	17,18	324,17	
44300	12,579	80,60	0,16	1,04	5,94	0,17	0,07	1,27	24100	5,25E-05	329	63,44	5,94569E-05	384,68	10,50	374,18	1,80	-1,13	18,44	268,09	
74300	12,579	80,60	0,16	1,00	5,90	0,17	0,07	2,38	30000	7,94E-05	389	65,82	3,8556E-05	368,32	9,75	358,57	1,82	-1,14	20,82	258,23	
104300	14,442	80,13	0,18	1,00	5,90	0,17	0,07	0,70	30000	2,35E-05	449	66,53	3,69847E-05	362,18	11,04	351,15	1,82	-1,13	21,53	246,77	
130400	15,374	76,87	0,20	0,99	5,90	0,17	0,08	1,06	26100	4,06E-05	501	67,59	2,8742E-05	341,94	11,51	330,43	1,83	-1,12	22,59	227,99	
164400	17,703	75,47	0,23	1,00	5,90	0,17	0,08	0,41	34000	1,21E-05	569	68,00	2,08132E-05	333,73	13,26	320,46	1,83	-1,11	23,00	213,93	
187000	13,51	71,75	0,19	1,00	5,90	0,17	0,08	0,44	22600	1,95E-05	614	68,44	1,99961E-05	315,43	10,07	305,37	1,84	-1,08	23,44	212,80	
220600	10,715	68,02	0,16	1,00	5,90	0,17	0,09	0,41	33600	1,23E-05	681	68,85	1,74927E-05	297,06	7,94	289,12	1,84	-1,06	23,85	207,88	
252100	12,579	65,69	0,19	1,00	5,90	0,17	0,09	1,29	65100	1,99E-05	744	69,74	1,7313E-05	283,30	9,20	274,10	1,84	-1,05	24,74	190,40	
284700	9,317	65,22	0,14	1,00	5,90	0,17	0,09	0,68	32600	2,08E-05	809	70,41		278,59	6,75	271,84	1,85	-1,04	25,41	198,62	
314700	10,715	66,16	0,16	1,00	5,90	0,17	0,09	0,15	30000	4,90E-06	869	70,56		282,31	7,74	274,57	1,85	-1,05	25,56	196,54	
322200	14,442	63,36	0,23	1,00	5,90	0,17	0,09	0,15	7500	1,96E-05	884	70,71		269,60	10,42	259,18	1,85	-1,03	25,71	174,03	
n <sub>av</sub>	2,702																				
b	25																				

Table 6.13 - Good quality fatigue test collected data: L4 specimen

ASTM Standard [18] suggests to evaluate the trend of the compliance versus the elapsed number of cycles. Figure 6.26 shows the results for the specimens tested.

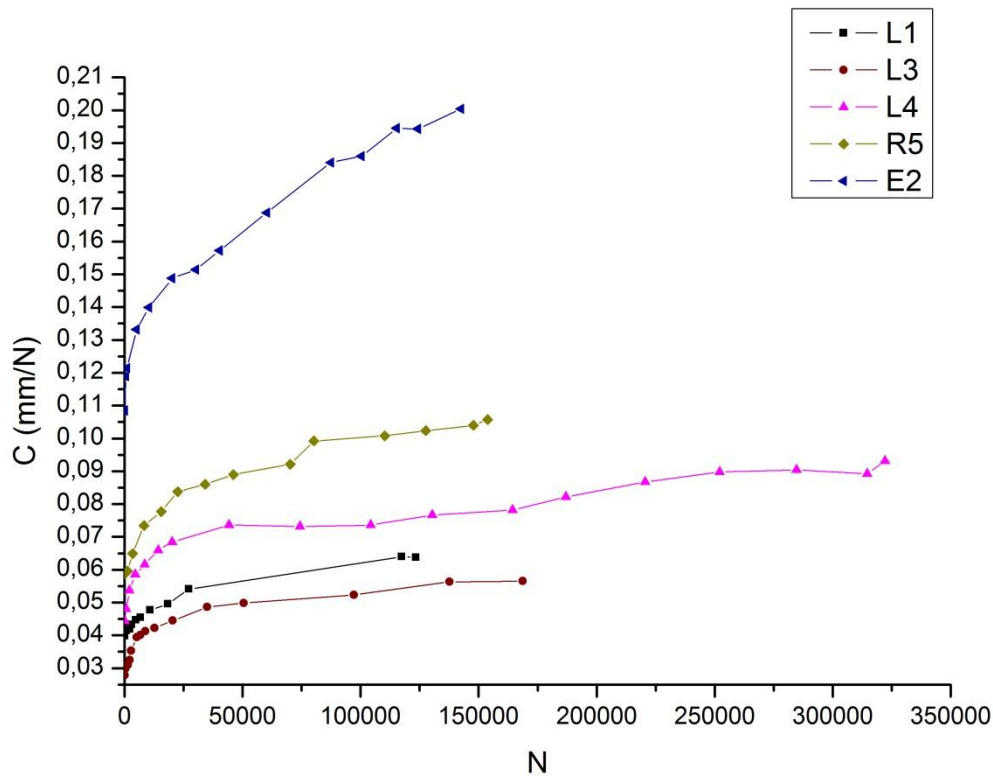


Figure 6.26 - C vs. N good quality plots

Figure 6.27 exhibits the *R curves*, i.e. the relation between the maximum fracture toughness  $G_{I_{max}}$  and the increment of crack length  $\Delta a$ .

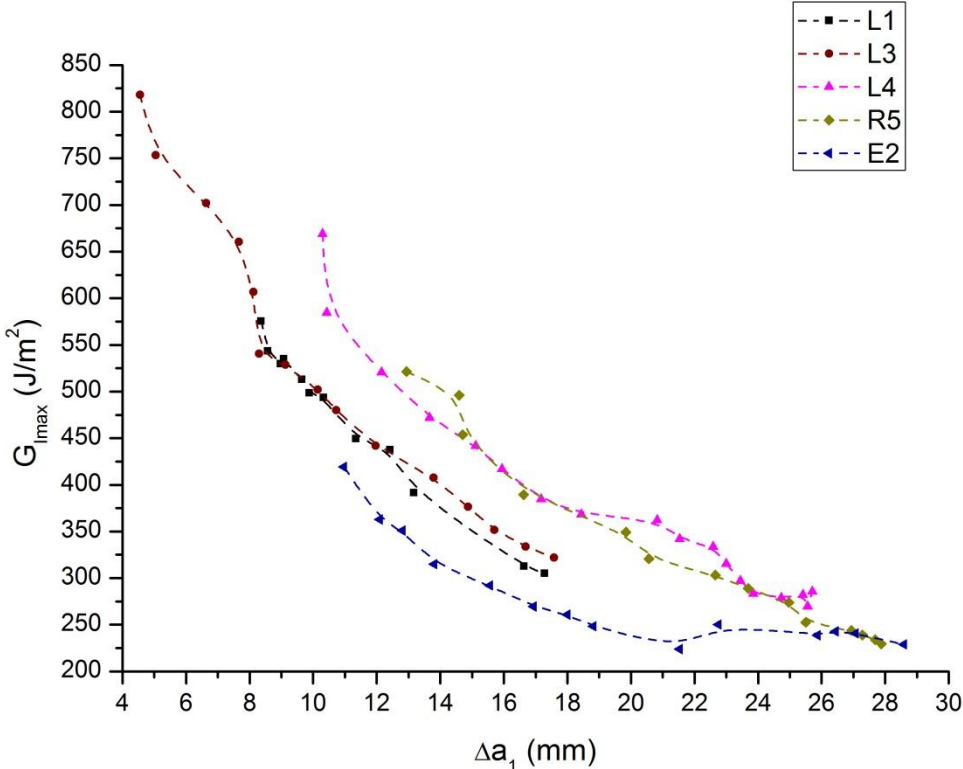


Figure 6.27 -  $G_{I_{max}}$  vs.  $\Delta a_1$  good quality plots

To specify the results displayed in the previous plot a clarification in  $\Delta a$  definition must be introduced. Using figure 6.28 two different initial situation can be noted; the first one took place when the delamination length at the end of the quasi-static test which preceded the fatigue test increased just by a length around 1 mm ahead the insert film (in red in the figure) as expected in *ASTM* reference [18]. The second situation took place when at the end of the quasi-static test a *crack jump* occurred ahead the insert film, increasing instantaneously the delamination by more than the expected 1 mm. The specimens tested went through this second condition, so the datum point initially situated at the end of the crack tip, with which the plot in figure 6.27 was obtained, has been reconsidered and placed at the end of the *crack jump* visible when starting the fatigue tests.

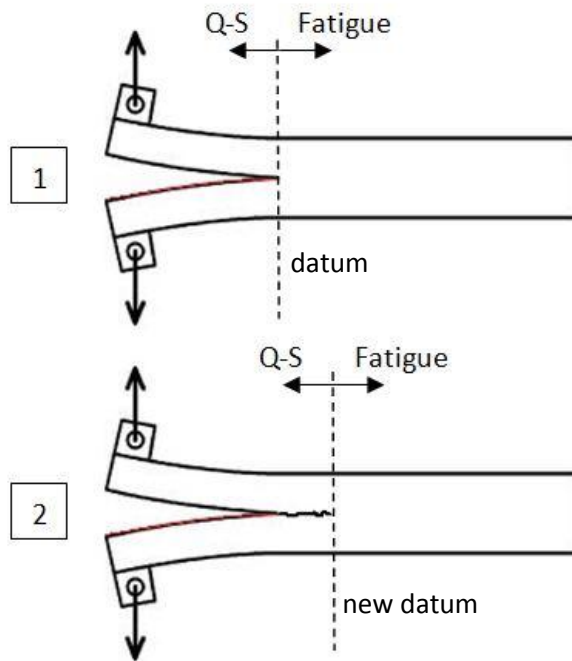


Figure 6.28 - Representation of  $\Delta a_1$  and  $\Delta a_2$

Referring to fig. 6.28, the definition of  $\Delta a$  has been changed from 1 to 2. The resultant plot found out is visible in figure 6.29.

Figure 6.30 displays the five *fatigue curves*, the fracture parameter  $\Delta G_{\sqrt{}}$  versus the number of elapsed cycles  $N$ .  $\Delta G_{\sqrt{}}$  decreases while the number of cycles proceeds, as expected. The curve deduced for L4 specimen results longer than the others, since for this specimen the test was extended in order to record data for a higher number of cycles and have so a feedback about the behaviour of the material when subjected to a longer fatigue life.

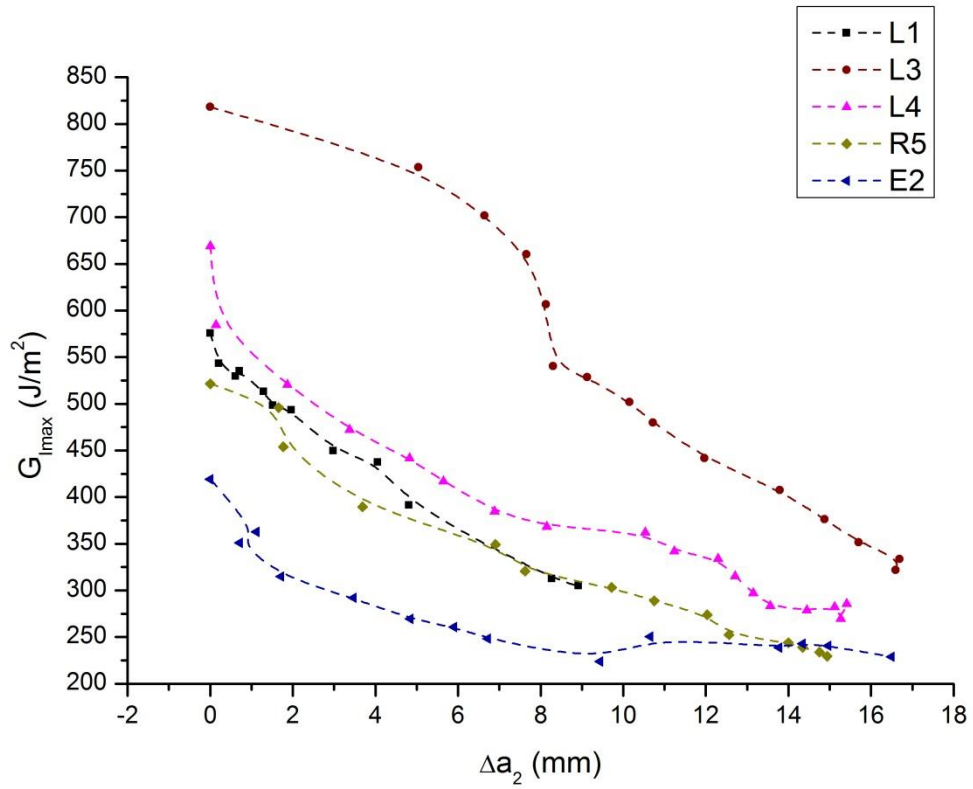


Figure 6.29 -  $G_{Imax}$  vs.  $\Delta a_2$  good quality plots

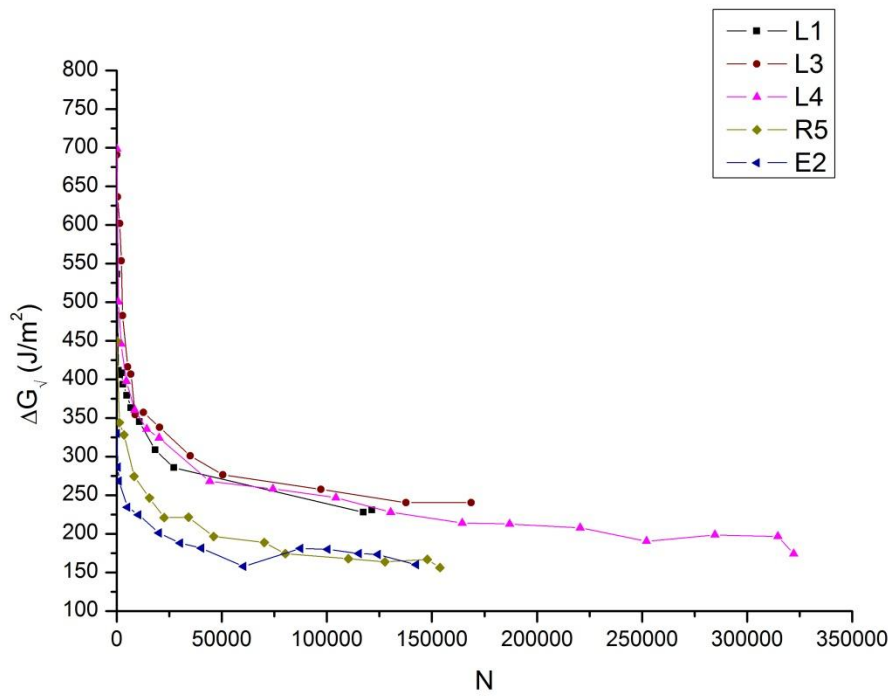


Figure 6.30 -  $\Delta G_{\sqrt{}}$  vs. N good quality plots

Figure 6.31 shows finally the *crack growth rate* plots  $da/dN$  versus  $\Delta G_{\sqrt{}}$ . To draw them it has been retained more adapt to use the values of  $da/dN$  calculated with the *secant method*, since the ones calculated by the *polynomial method* are considered not enough to fit an accurate curve; indeed the second method leads to the loss of different points (the first two and the last three) among those chosen to calculate the growth rate.

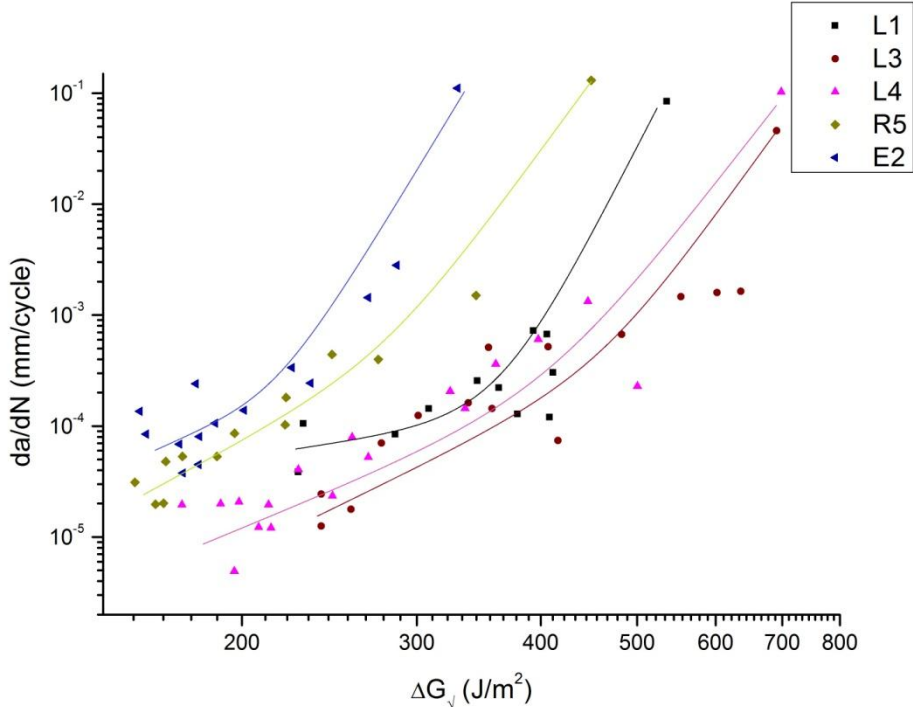


Figure 6.31 -  $da/dN$  vs.  $\Delta G_{\sqrt{}}$  good quality plots

*Fibre bridging* took place during fatigue tests as it happened for the static ones. Examples are visible in figure 6.32 for specimen R5 (a), where the bridging occurred just ahead the insert film right at the first collected point (100 cycles), and for specimen E2 (b), where it happened distant from the insert film.

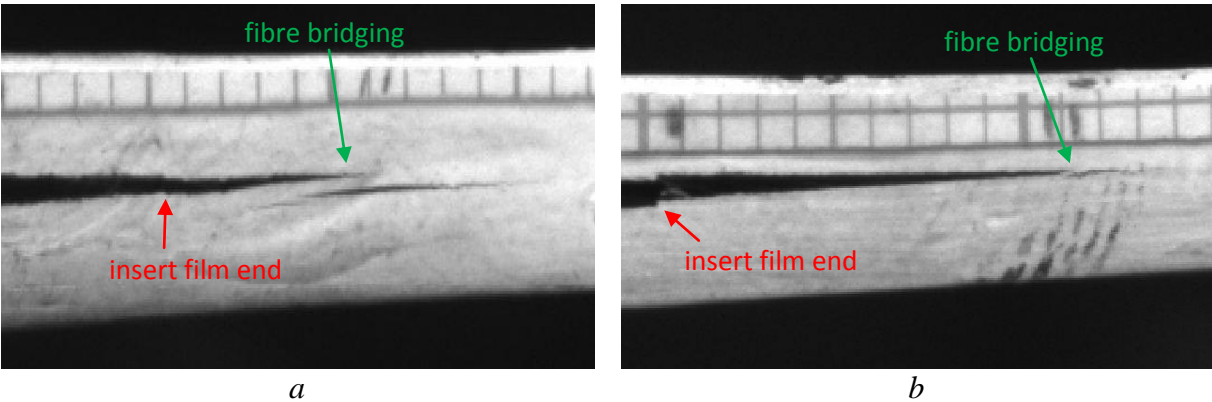


Figure 6.32 - Fibre bridging examples, good quality

### 6.2.2 Poor Quality material

The results reached for the *poor* quality are here presented following the same line up just used for the *good* one. Comments are inserted just where retained necessary, otherwise the review and discussion of the results here reported will be presented in the next *Chapter 7*, as for the rest of the test results here showed.

Table 6.14 gives again an example (specimen D9) of the tables created to elaborate the data collected by the machine.

Cycle	P <sub>min</sub>	P <sub>max</sub>	R	δ <sub>min</sub>	δ <sub>max</sub>	R	C	da	dN	a <sub>0</sub>	N	da/dN (secant)	Pics	a	da/dN (polinomial)	a <sub>i</sub>	Gmax	Gmin	ΔG	Loga	LogC	Δa	ΔG <sub>i</sub>	
num	N	N	N/N	mm	mm	mm/mm		mm		mm	N	mm/cycle	Update	mm	mm/cycle	mm	J/m <sup>2</sup>	J/m <sup>2</sup>	J/m <sup>2</sup>			mm	J/m <sup>2</sup>	
100	3,261	29,35	0,11	0,16	1,71	0,09	0,06	3,02	100	3,02	100	3,02E-02	669	3,02		3,02	487,52	5,04	482,47	0,48	-1,24	3,02	393,40	
900	5,59	30,28	0,18	0,46	1,71	0,27	0,06	2,53	800	5,55	900	3,16E-03	678	5,55		5,55	273,92	13,58	260,34	0,74	-1,25	5,55	165,52	
4600	6,988	26,56	0,26	0,49	1,70	0,29	0,06	3,07	3700	8,62	4600	8,29E-04	716	8,62	0,001216504	6,09	153,94	11,69	142,25	0,94	-1,19	8,62	80,78	
5300	4,658	29,82	0,16	0,46	1,71	0,27	0,06	2,35	700	10,96	5300	3,35E-03	723	10,96	0,000147575	8,43	136,56	5,74	130,82	1,04	-1,24	10,96	86,31	
8600	5,59	29,35	0,19	0,49	1,75	0,28	0,06	0,73	3300	11,69	8600	2,21E-04	754	11,69	4,50931E-05	9,16	129,13	6,82	122,31	1,07	-1,22	11,69	76,59	
142800	2,329	19,10	0,12	0,46	1,75	0,27	0,09	1,81	134200	13,50	142800	1,35E-05	1028	13,50	3,13228E-05	10,97	72,66	2,35	70,31	1,13	-1,04	13,50	48,87	
173500	1,397	16,77	0,08	0,47	1,75	0,27	0,10	0,69	30700	14,19	173500	2,25E-05	1089	14,19	2,86669E-05	11,66	60,69	1,34	59,34	1,15	-0,98	14,19	43,97	
205100	1,397	19,10	0,07	0,47	1,75	0,27	0,09	1,15	31600	15,35	205100	3,65E-05	1152	15,35		12,82	63,92	1,24	62,67	1,19	-1,04	15,35	47,33	
229500	1,397	15,84	0,09	0,47	1,75	0,27	0,11	1,50	24400	16,85	229500	6,15E-05	1201	16,85		14,32	48,28	1,13	47,15	1,23	-0,96	16,85	34,63	
283100	0,465	15,37	0,03	0,46	1,75	0,27	0,11	1,19	53600	18,04	283100	2,22E-05	1308	18,04		15,51	43,77	0,35	43,42	1,26	-0,94	18,04	36,28	
nav	1,468																							
b	25																							

Table 6.14 - Poor quality fatigue test collected data: D9 specimen

The plots of compliance versus number of cycles required by the *ASTM* reference are reported in figure 6.33.

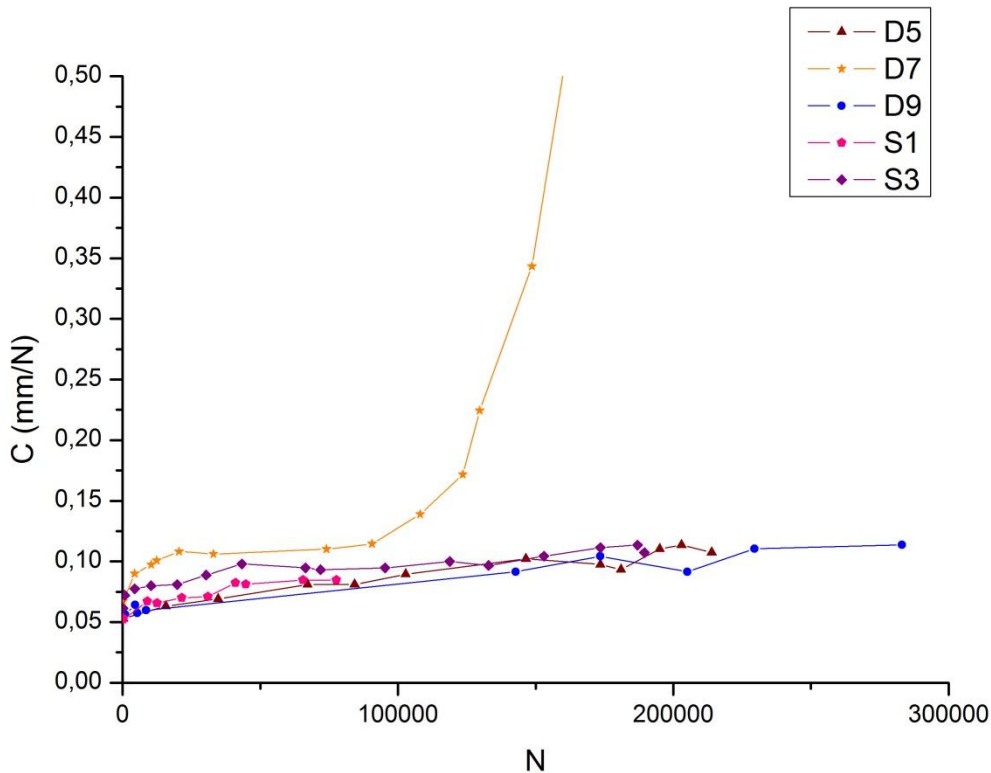
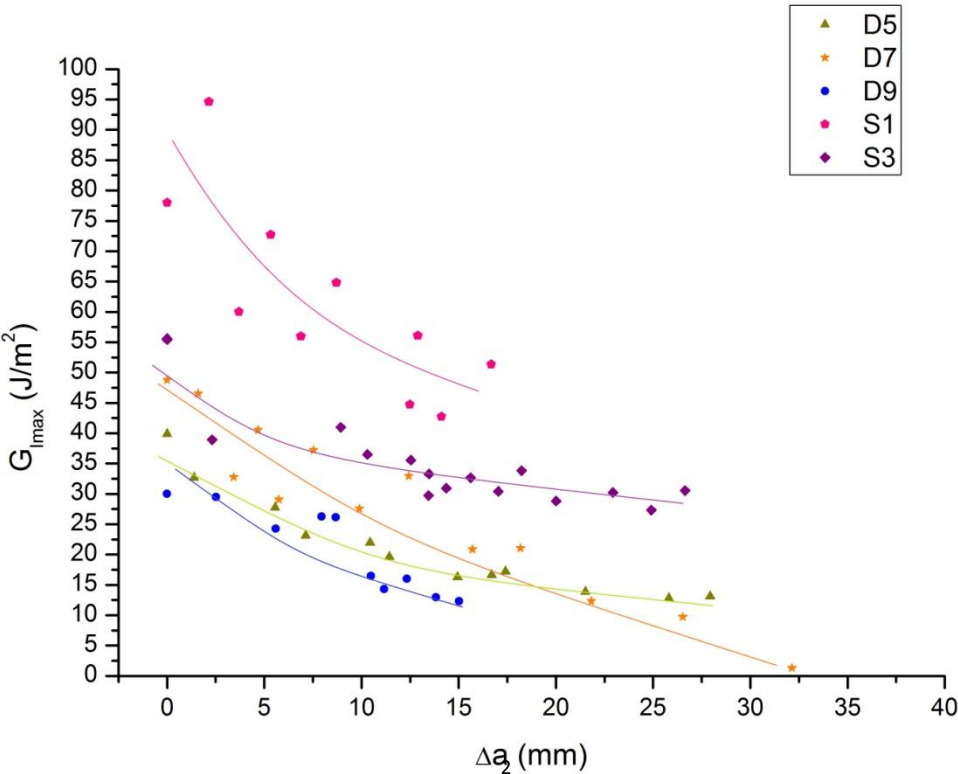


Figure 6.33 - C vs. N poor quality plots

It has been already underlined for static test results how the analysis of the *poor* quality data was more complicate, resulting often in less points collectable to describe the curves. The same happened for fatigue tests, as can be confirmed examining the *R-curves* displayed in figure 6.34. The definition of crack length increment used is again the second one,  $\Delta a_2$ . The *fatigue curves* are then reported in figure 6.35 while the *crack growth rate* curves follow in figure 6.36.



Fatigue 6.34 -  $G_{\text{Imax}}$  vs.  $\Delta a_2$  poor quality plots

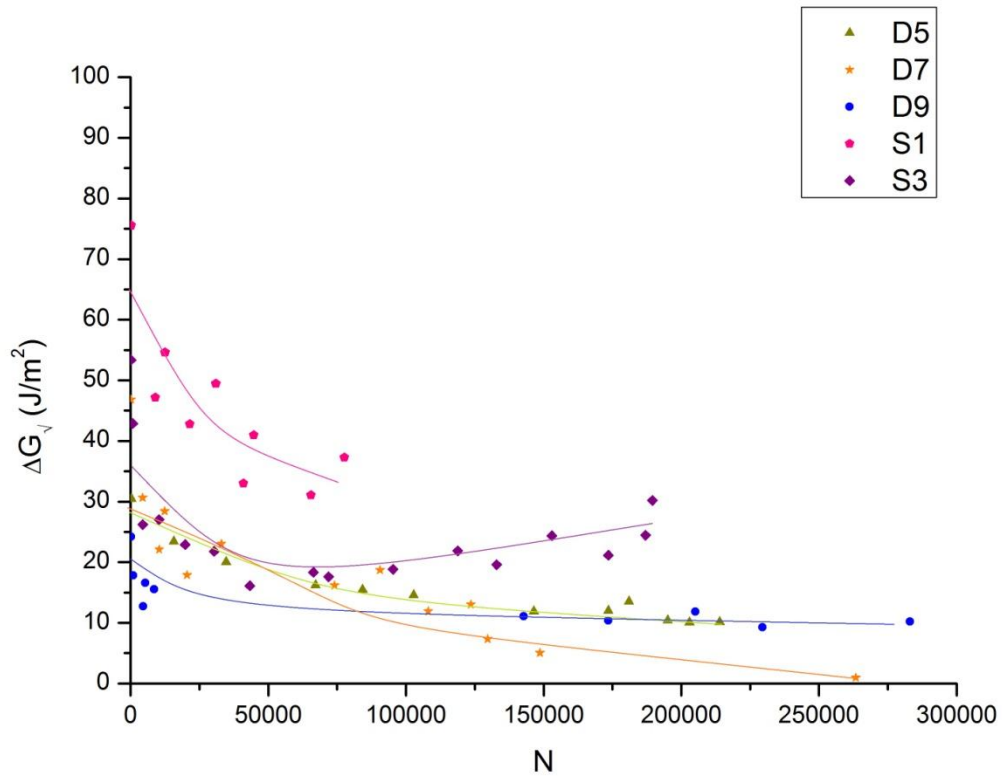


Figure 6.35 -  $\Delta G_v$  vs. N poor quality plots

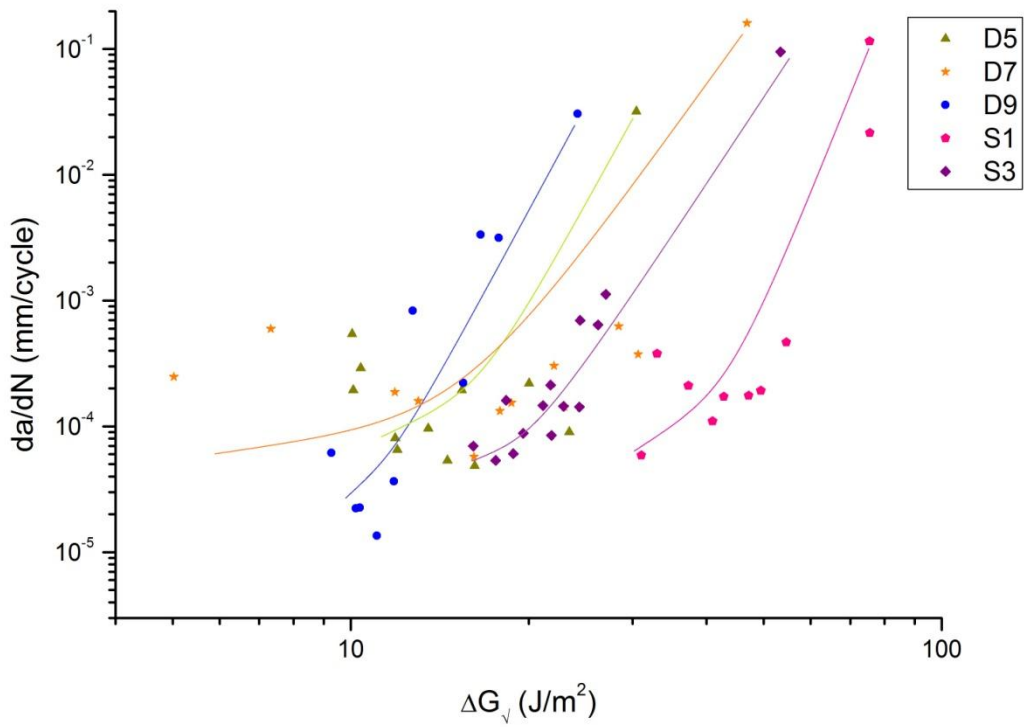


Figure 6.36 - da/dN vs.  $\Delta G_v$  poor quality plots

The scattering in the data is clear and immediate. The *crack growth rate* curves have been plotted as done for *good* quality material, but actually not all the points correspond to a stress ratio  $R=0,1$ . This issue is to be attributed to the machine, which indeed loses its accuracy while it is working with very low loads and displacements. Therefore the load displayed by the software during the test is not the one actually applied and recorded. During the analysis the continuous variation in stress ratio values has been examined.

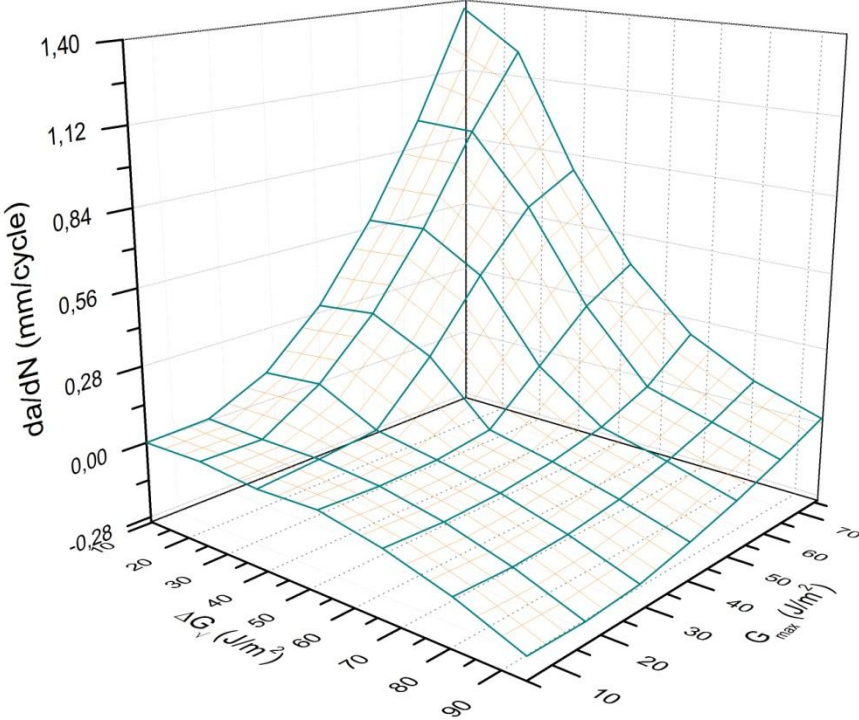
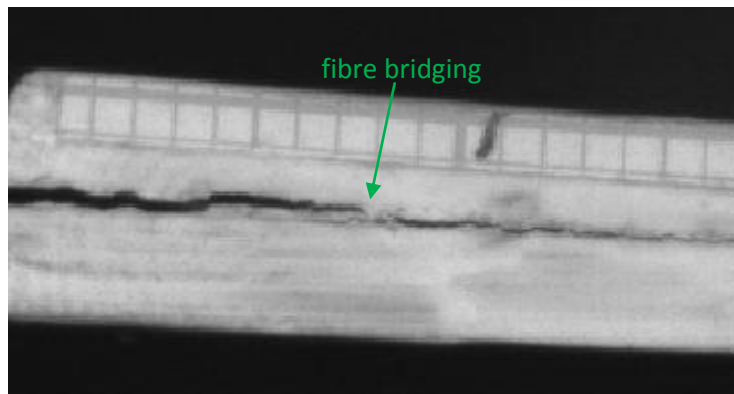


Figure 6.37 – 3D plot:  $da/dN$  as a function of  $\Delta G_{\sqrt{}}$  and  $G_{max}$ , poor quality

Fatigue is considered as a two load parameter problem. Referring to what reported in reference [41] in terms of *SIF*, and recalling the analogy with *SERR* reported in the previous chapters, a conventional representation of the crack growth  $da/dN$  as a function of a single driving force, in this case the fracture parameter  $\Delta G_{\sqrt{}}$ , can result inadequate. Two independent load parameters are necessary to describe cyclic load unambiguously. For this reason a second parameter should be used, a second driving force,  $G_{max}$ , which accounts for the effects of the *R-ratio*. Indeed the stress ratio is required to quantify the fatigue crack growth besides the fracture parameter  $\Delta G_{\sqrt{}}$ , which represents the only driving force. Adding  $G_{max}$  to the analysis gives as a results two driving forces, but only one can be the controlling parameter for a given range of *R*. For a low value of *R* the controlling parameter is  $G_{max}$  while for high values it is  $\Delta G_{\sqrt{}}$ . The results obtained carrying the described analysis are plotted in a 3D plot. The values plotted in such graph give life to a surface, as can be seen in the previous figure 6.37.

*Fibre bridging* occurred also during the fatigue test of the *poor* quality material as for all the other tests reported until now. It was not easy to distinguish the event because of the already mentioned unclear aspect of the specimens' edge. An example is reported in figure 6.38.



*Figure 6.38 - Fibre bridging example, poor quality*

## 7. Discussion

This chapter completes the dissertation furnishing a comparison between the results acquired for the two different qualities just presented in the previous chapter.

The discussion will focus first on the results for quasi static tests and then for the fatigue ones.

### 7.1 Quasi-Static tests

The first dissimilarity noticed during the quasi static tests is the different duration of the process. Indeed the machine was set with the same procedure, i.e. displacement control with a maximum displacement of 25 mm; this final point was reached by the *good* quality material in around 35 minutes, while the tests for the *poor* quality material were faster (around 7 - 10 minutes) and thus they did not reach the final displacement, stopping somehow earlier. This allowed to collected less points for the second quality, which led to curves less defined in shape and less accurate.

Beside the difference in displacement is collocated the difference in load, since the two parameters are directly connected. The maximum loads applied by the machine under the set displacement control during the *good* quality tests were approximately three times the ones for *poor* quality. To confirm what just said table 7.1 displays the maximum load recorded for each specimen and an example of load versus displacement plots can be seen in figure 7.1.

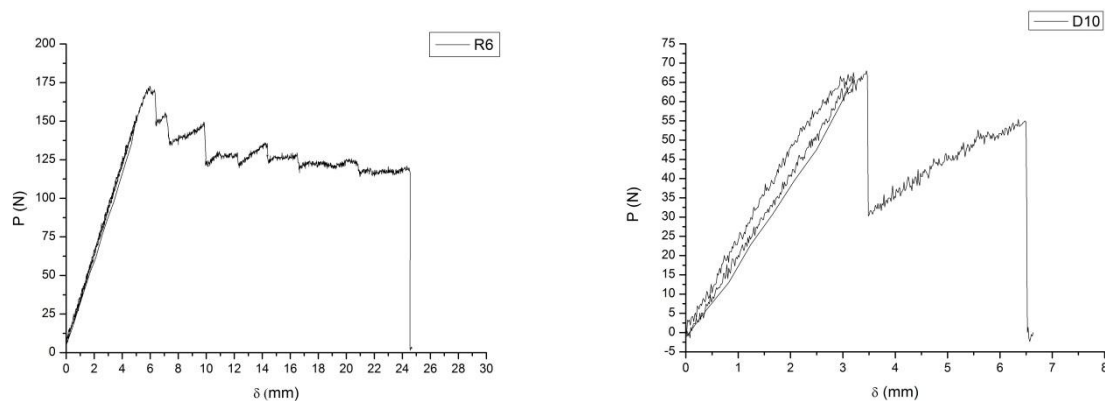


Figure 7.1 - P vs.  $\delta$  plots: comparison between good and poor quality

<i>Good quality (N)</i>		<i>Poor quality (N)</i>	
<i>R1</i>	131,84	<i>D2</i>	63,83
<i>R2</i>	143,1	<i>D6</i>	49,38
<i>R3</i>	150,68	<i>D10</i>	68,1
<i>R6</i>	172,84	<i>S2</i>	66,62
<i>R8</i>	177,97	<i>S4</i>	41,5

Table 7.1 - Maximum load: comparison between good and poor quality

Referring to the  $P$ - $\delta$  plots other considerations can be pointed out.

In the previous chapter was underlined how the *crack jumps* were frequently recorded in *poor* quality tests. Comparing the figure reporting the plots for *good* quality and the one for *poor* quality (fig. 6.2 and 6.16) this phenomenon results easily visualized. As already referred these jumps were usually preceded by *fibre bridging* and followed by a *load drop*, in some cases substantial (D2 and D10).

Figure 7.1 helps also to highlight an important difference in loading procedure. The *poor* quality specimens were subjected to an instantaneous crack increase at the end of the first loading process and just before the unloading took place. The successive reloading thus reached the maximum load value for another value of delamination length  $a$ . For this reason the plots resulted in a reloading curve shifted to the right with a certain offset compared to the first loading curve.

Concerning the slope of the linear region of the  $P$ - $\delta$  plots, a slight difference was found out between the two qualities. The average slope was evaluated considering the linear region of the reloading curve; the average value in plots for the *good* quality specimens is 24,53, while for the *poor* quality specimens is 17,04. The slope represents the reverse of the compliance  $C$  so the reason of the decreasing in slope is immediately identifiable considering what reported above, i.e. the considerable reduction in the load applied to the *poor* quality specimens resulting in a lower value of the slope (equal to the parameter  $1/C=P/\delta$ , figure 7.2).

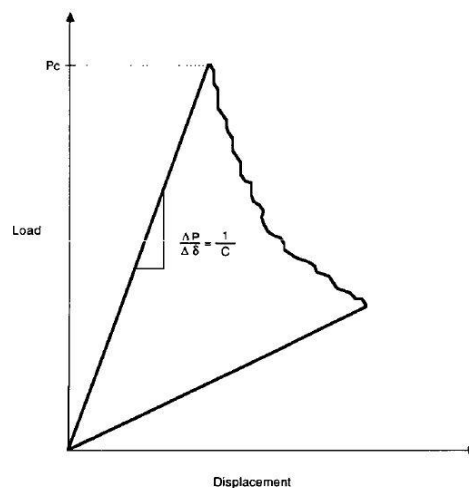


Figure 7.2 -  $P$  vs.  $\delta$  general plot: slope definition [42]

This change in behaviour agrees with the theory; in fact the slope of a load versus displacement curve indicates the flexural and shear stiffness of the material. Being its value lower for the *poor* quality specimens means that there is a loss in stiffness passing from the *good* quality to the *poor* one. Figure 7.3 displays a comparison between a *good* quality specimen (R3) and a *poor* quality one (D2).

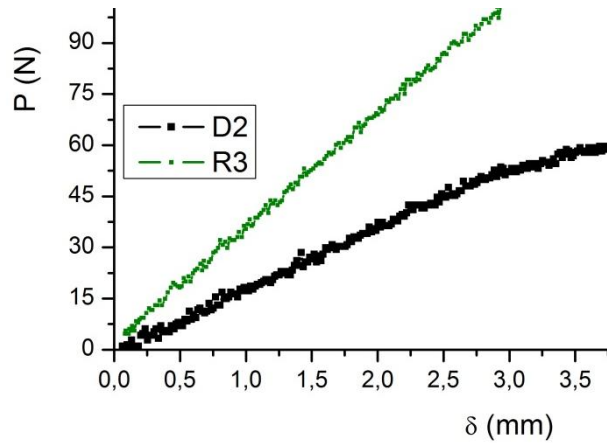


Figure 7.3 - P vs.  $\delta$  plot slope: comparison between D2 and R3

An analysis of the slope was also possible for the *R-curves* plots. Plotting in the same graph the results found out both for *good* and *poor* qualities, the two regions occupied by the data can be appreciated. Analysing the data and evaluating a linear fitting of the scatter points a value for the slopes of the ranges of values has been obtained. Figures 7.4 and 7.5 show respectively the *CCM* and *MBT* plot.

In table 7.2 are reported the values of the slope as a function of the quality and the method used. The slope of the *MBT* plots is higher than that of *CCM* plots; one reason can be that the lower onset values end up with higher final values introducing a larger scatter, so the linear fit results to be steeper. Furthermore *MBT* values present an higher variance, so it can be appointed that this method is more affected by the change in the material quality. However in both cases, the slopes for each quality are comparable each other, because they present the same order of magnitude; it can be concluded that passing from one quality to the other the plots are just shifted to a different region in the graph, because of the large difference in toughness values.

	<i>CCM</i>	<i>MBT</i>
<i>Good quality</i>	4,55	6,55
<i>Poor quality</i>	3,54	4,2

Table 7.2 -  $G_{Ic}$  vs.  $\Delta a$  slopes: comparison between quality and methods

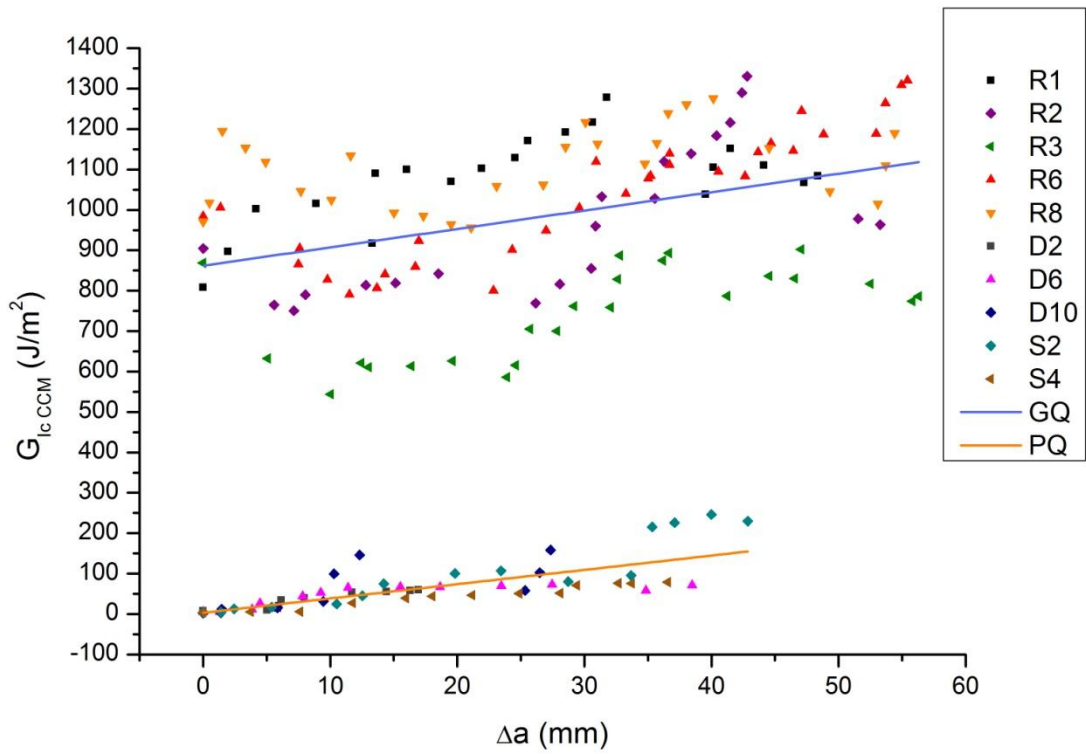


Figure 7.4 -  $G_{Ic\_CCM}$  vs.  $\Delta a$  plots: comparison between good and poor quality

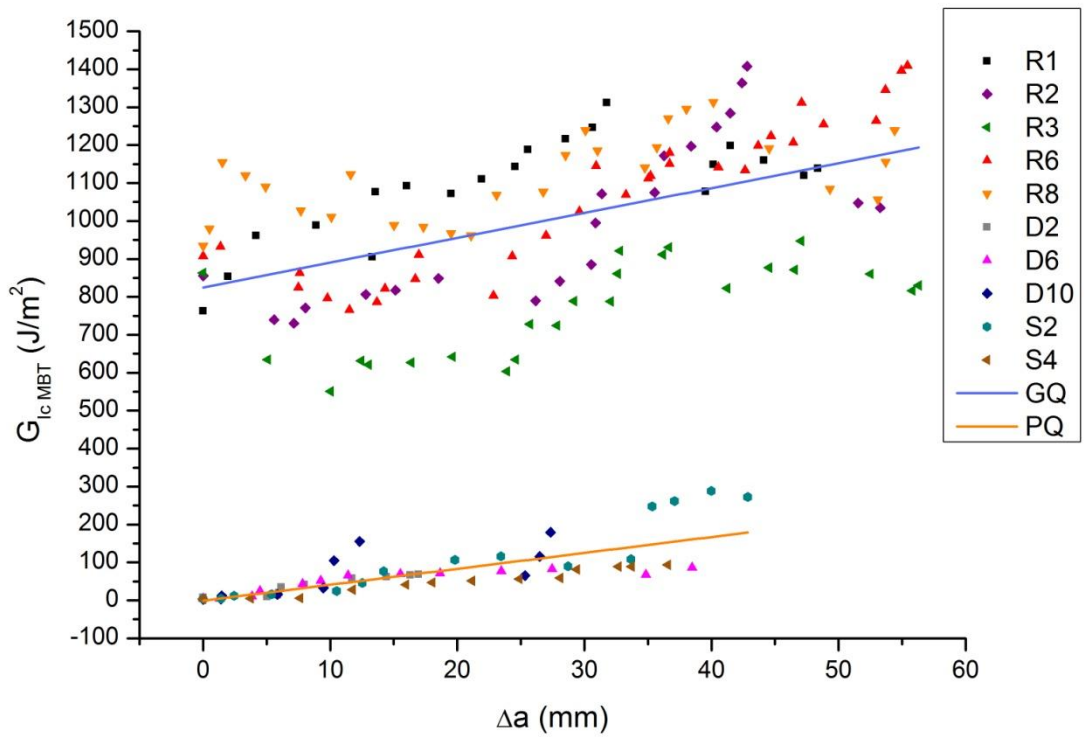


Figure 7.5 -  $G_{Ic\_MBT}$  vs.  $\Delta a$  plots: comparison between good and poor quality

Considering the precision parameters reported in the previous chapter, it is immediately certified the different behaviour of the two qualities. In fact the *good* quality specimens exhibit values of the standard deviation, the coefficient of variation and the opening displacement within the limits suggested by the *ASTM* standard method, while the *poor* quality ones are certainly contrasting.

It is finally important to remark the difference noted in the type of delamination propagation: the *good* quality specimens exhibited mainly a *cohesive failure* while the *poor* quality ones were dominated by an *adhesive failure*. These events confirm the goodness of the process followed to manufacture the plates. Indeed as already reported the quality of each single lamina is the same, i.e. a good one, obtained following the instruction given by the supplier. The difference between the plates lies in the quality of the bonding; the *poor* quality suffered the poorness of the bonding, which gave rise to an *adhesive* kind of failure, i.e. the adhesive was unable to keep the surfaces bonded. From this derives the more frequent presence of *crack jumps* and *load drops*, abundantly mentioned and shown in several pictures.

## 7.2 Fatigue tests

The values of *crack growth rates* both for *good* and *poor* quality material have been plotted in the same graph (figure 7.6) as done previously for interlaminar fracture toughness in static tests. Once again the slopes of the linear fits (here curves because both axes present logarithmic scale) have been evaluated. Their values result comparable being 8,24 for the *good* quality fit and 9,75 for the *poor* quality one; it can be concluded that it is possible to pass from one plot to the other shifting the values from one region in the graph to another, according with the fracture parameter range.

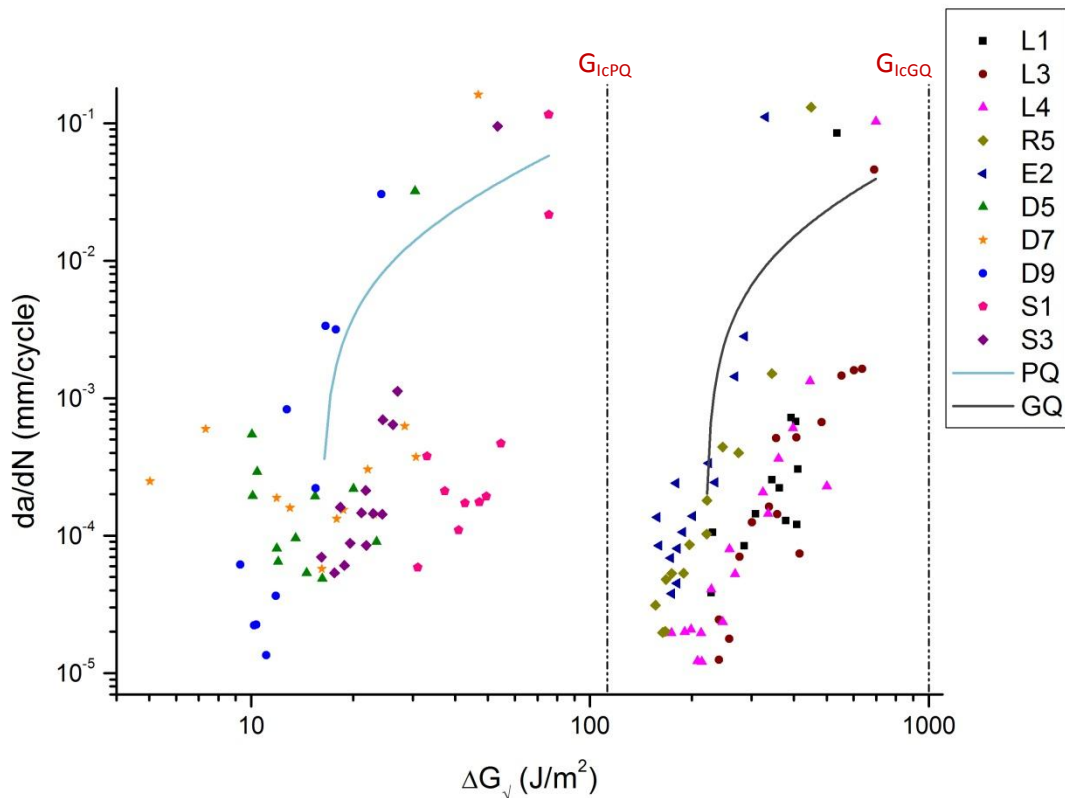


Figure 7.6 -  $da/dN$  vs.  $\Delta G_V$  plots: comparison between good and poor quality

In the same graph above the  $G_{Ic}$  for each quality has been reported. The value was obtained as the average of the onset values of the five specimens tested for each quality. For each specimen the onset value considered is the one resulting using the *NL* method with the data collected during the static tests preceding the fatigue test:

	$G_{IcAV}$ ( $J/m^2$ )
<i>Good quality</i>	1001,21
<i>Poor quality</i>	112,31

Table 7.3 -  $G_{IcAV}$  values: comparison between good and poor quality

According with the average onset values, it can be appointed that both qualities maintain their range of *SERR* within the allowed region, i.e. the maximum value for each specimen is lower

than the average value of *SERR*, which is considered as a threshold for each quality. In particular the *good* quality seems to keep a larger distance from its threshold, because it presents values hundred  $J/m^2$  lower than the average toughness. Table 7.4 reports the highest values of  $G_{I_{max}}$  for each specimen to confirm what just enunciated.

<i>Good quality (J/m<sup>2</sup>)</i>		<i>Poor quality (J/m<sup>2</sup>)</i>	
<i>L1</i>	535,91	<i>D5</i>	30,44
<i>L3</i>	690,14	<i>D7</i>	46,82
<i>L4</i>	698,31	<i>D9</i>	24,21
<i>R5</i>	449,51	<i>S1</i>	75,57
<i>E2</i>	329,91	<i>S3</i>	53,34

Table 7.4 - Highest  $G_{I_{max}}$  values: comparison between good and poor quality

Plotting in the same graph the results earned for the *R curves* the first thing which stands out analysing figure 7.7 is the gap in crack length between the two qualities. The *poor* quality reached a bigger length in a number of cycles comparable with that of the *good* quality. The number of cycles can be confronted in figure 7.8.

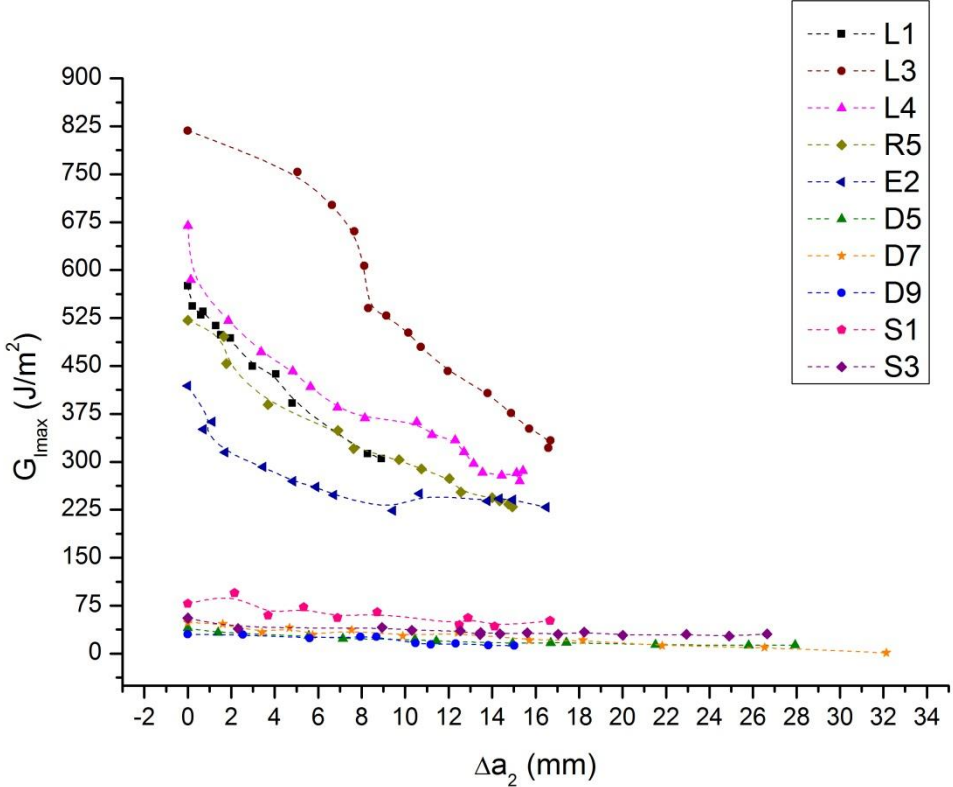


Figure 7.7 -  $G_{I_{max}}$  vs.  $\Delta a_2$  plots: comparison between good and poor quality

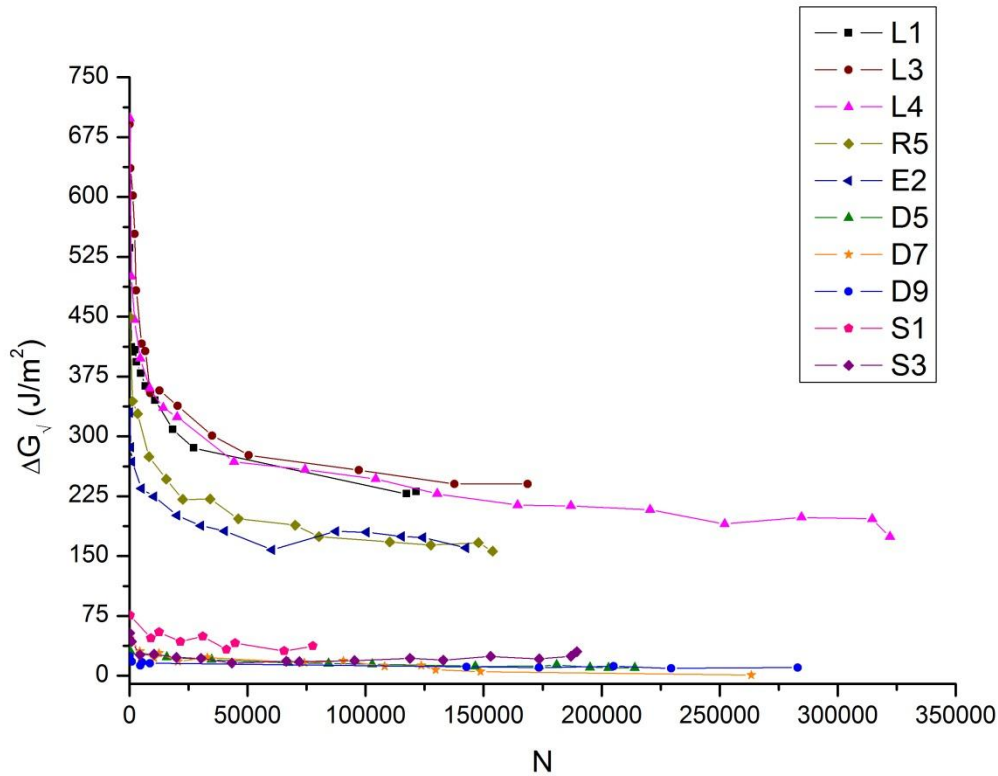


Figure 7.8 -  $\Delta G_v$  vs. N plots: comparison between good and poor quality

A difference can be also found comparing the plots displaying the compliance versus the number of elapsed cycles; the graphs are reported again here for clarity in figure 7.9.

Concerning *good* quality specimens, the curves agree with the general plot presented as an example in figure 4.2. The onset region agree in terms of slope and so the propagation region, except for specimen E2 where the latter appears steeper than the reference plot. This finds its reason in the lower maximum applied load and the higher open displacement compared with the other specimens tested. From this point of view, during fatigue test E2 specimen seems to behave differently from the specimens belonging to the same plate.

Comparing the curves for *poor* quality material with the example plot, they present an onset region shorter and characterized by a lower slope. All the specimens furnish a curve which shows the onset and the propagation regions; the curve of D7 specimen includes also the accelerate failure region, which moreover occurs for a number of cycles considerably lower compared with the other specimens, where in fact the failure region is not yet visible.

Finally can be observed how the values of compliance for *good* quality are comparable with those for *poor* quality, excepted for the two mentioned specimens, respectively E2 and D7. Indeed the values are within a range approximately of 0,03 – 0,11 mm/N for the *good* quality specimens and 0,05 – 0,1 mm/N for *poor* quality, confirming so a good agreement.

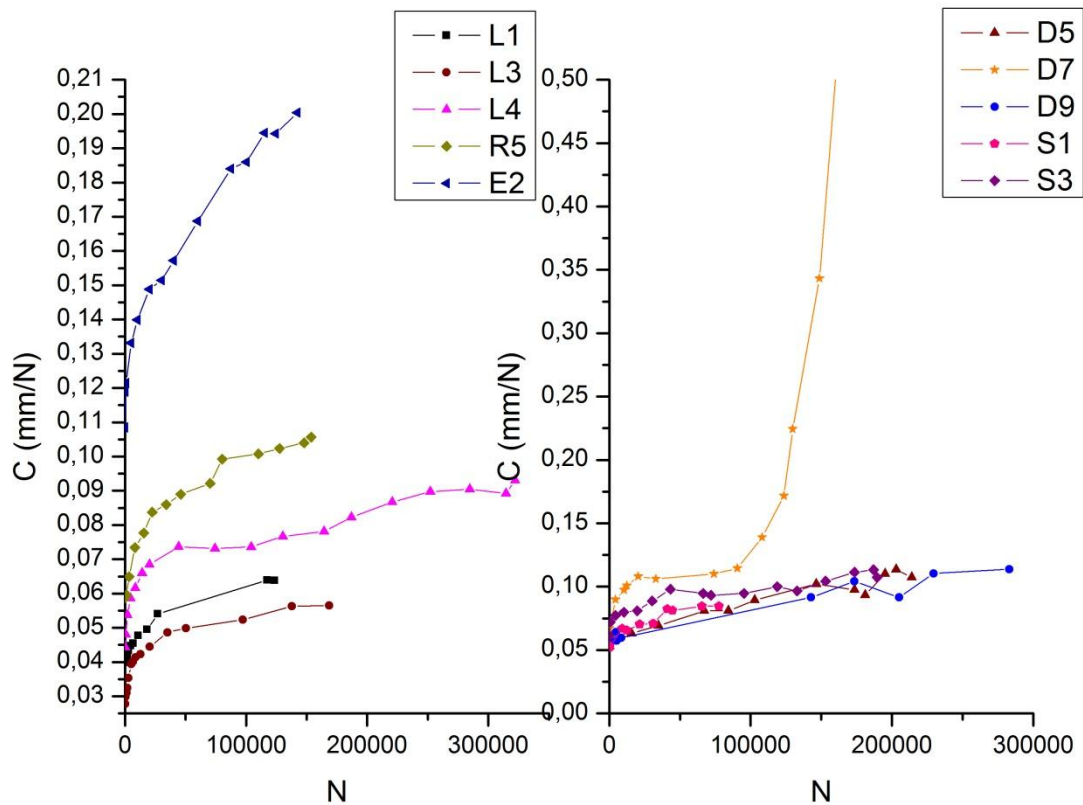


Figure 7.9 - C vs. N plots: comparison between good and poor quality

A final point to discuss is the relation between delamination behaviour and material quality, in particular referring to phenomena like *crack jumps* and *load drops* presented in the results chapter. Figure 6.23 reported the broken specimen used to justify the *adhesive failure* often noticed during crack propagation in *poor* quality specimens. This kind of failure leads to think that the quality of the bonding process had great influence in the delamination behaviour, since the main difference between the two qualities lies in a poorer bonding, obtained without applying the required pressure.

## 8. Conclusions

---

Several parameters characterizing the delamination process in the composite material manufactured were investigated in this report. Quasi-static interlaminar fracture toughness and fatigue crack growth rate were mainly evaluated through mode I loading tests. Two qualities have been compared, a *good* one and a *poor* one.

The differences presented between them originate from the different bonding process followed to bond the two laminates together using the epoxy adhesive.

In general the two qualities seem to agree in the results, i.e. the results obtained for each one can be referred to the other one simply shifting the curves to a different range of values. This resulted possible from the analysis both of static and fatigue results. The range of values are evidently different because of the different strength of the specimens belonging to each quality, resulting in lower tolerable loads for *poor* quality and so lower values of toughness for example.

Therefore to obtain a material which guaranties the best features is suggested to follow the instructions given by the suppliers to manufacture the materials. These features are in particular strength, delamination resistance in terms of interlaminar fracture toughness in quasi-static tests and crack growth rate in fatigue tests. Others undesired events such as *crack jumps* and *load drops* can be avoided using a better quality of material, reducing the risk of catastrophic failure. So a correct bonding process is suggested, creating the vacuum bag and applying the required pressure during the autoclave cycle, in order to avoid voids at the interface which can cause crack jumps and unstable crack growth.

Different and somehow deeper analysis are suggested to be carried on to understand better some events. For example a Scanning Electron Microscopy (*SEM*) inspection is suggested to study the degree of resin fracture at the delamination surfaces; it can result useful also to analyse the roughness of the surfaces related to the effect of the different R-ratio (in particular for *poor* quality specimens). A numerical simulation can also be conducted using a finite element software, for example to study the behaviour of the material under mode II loading, using the so called *cohesive analysis* and the related data reduction methods; reference [27] provides an interesting model in this sense. In addition more experimental tests can be conducted to evaluate the influence of other parameters, that is layer thickness, epoxy adhesive thickness or test temperature.



# References

---

- [1] R. Jones , Mechanics of Composite Materials, 2<sup>nd</sup> Edition (1999), Taylor & Francis
- [2] T. Sinmazçelik, E. Avcu, M. Özgür Bora, O. Çoban, A review: Fibre metal laminates, background, bonding types and applied test methods, Materials and Design 32 (2011), 3671 – 3685
- [3] I. Daniel, Failure of Composite Materials, Strain 43 (2007), 1475 – 1305
- [4] M. Sham Prasad, C. Venkatesha, T. Jayaraju, Experimental Methods of Determining Fracture Toughness of Fiber Reinforced Polymer Composites under Various Loading Condition, Journal of Minerals & Materials Characterization & Engineering 13 (2011), 1263 – 1275
- [5] J. Kim, Y. Mai, Engineered Interfaces In Fiber Reinforced Composites (1998), Elsevier Science Ltd
- [6] J. Zhou, T. He, On the analysis of the end-notched flexure specimen for measuring mode II fracture toughness of composite materials, Composites Science Technology 50 (1994), 209 – 213
- [7] J.R.J Wingfield, Treatment of Composite Surfaces for Adhesive Bonding, International Journal of Adhesion & Adhesive 13 (1993), 151 – 156
- [8] L. Nie et al., Void control in adhesive bonding using thermosetting polymer, Sensors and Actuators A 167 (2001), 398 – 405
- [9] <http://composite.about.com/>
- [10] S. Mall, K.T. Yun. Effect of Adhesive Ductility on Cyclic Debond Mechanism in Composite-to-Composite Bonded Joints, The Journal of Adhesion 23 (1987), 215 – 231
- [11] C. Rans, R. Alderliesten, Formulating an Effective Strain Energy Release Rate for a Linear Elastic Fracture Mechanics Description of Delamination Growth, Conference Paper, TU Delft (2009)
- [12] Anonimous, Guide to prepreg, Lavender CE Pty Ltd, [www.lavender.com](http://www.lavender.com)
- [13] Delta tech<sup>TM</sup> Epoxy Matrix System DT120 Datasheet, [www.delta-tech.it](http://www.delta-tech.it)
- [14] Anonimous, FM 94 Adhesive Film Technical Data Sheet, Cytec Engineered Materials, [www.cytec.com](http://www.cytec.com)
- [15] A. Brunner, B. Blackman, P. Davies, A status report on delamination resistance testing of polymer–matrix composites. Engineering Fracture Mechanics 75 (2008), 2779 – 2794
- [16] M. Shokrieh, M. Heidari-Rarani, M. Ayatollahi, Delamination R-curves as a material property of unidirectional glass/epoxy composites, Materials and Design 34 (2012), 211 – 218

- [17] Standard Test Method for Mode I Interlaminar Fracture Toughness of Unidirectional Fiber-Reinforced Polymer Matrix Composites, ASTM D5528-01 (2007), ASTM International, US
- [18] Standard Test Method for Mode I Fatigue Delamination Growth Onset of Unidirectional Fiber-Reinforced Polymer Matrix Composites, ASTM D6115-97 (2011), ASTM International, US
- [19] Standard Test Method for Measurement of Fatigue Crack Growth Rates, ASTM E647 – 00, ASTM International, US
- [20] I. Ashcroft, S. Shaw, Mode I fracture of epoxy bonded composite joints 2. Fatigue loading, *International Journal of Adhesion & Adhesive* 22 (2002), 151 – 167
- [21] M. Fernandez et al., Composite bonded joints under mode I fatigue loading, *International Journal of Adhesion & Adhesive* 31 (2011), 280 – 285
- [22] R. Khan, C. Rans, R. Benedictus, Effect of stress ratio on delamination growth behaviour in unidirectional carbon/epoxy under mode I fatigue loading, Conference Paper, TU Delft (2009)
- [23] P. Davies, B. Blackman, A. Brunner, Standard test methods for delamination resistance of composite material: current status. *Applied Composite Material* 5 (1998), 345 – 364
- [24] Standard Test Methods for Flexural Properties of Unreinforced and Reinforced Plastics and Electrical Insulating Materials, ASTM D790-07, ASTM International, US
- [25] Airbus Industrie, Carbon fibre reinforced plastics, Determination of interlaminar fracture toughness energy, Mode II, AITM 1.0006 (2004)
- [26] K. Tanaka, K. Kageyama, M. Hojo, Prestandardization study on mode II interlaminar fracture toughness test for CFRP in Japan, *Composites* 26 (1995), 257 – 267
- [27] M. de Moura, R. Campilho, J. Gonçalves, Pure mode II fracture characterization of composite bonded joints, *International Journal of Solids and Structures* 46 (2009), 1589 – 1595
- [28] H. Yoshihara, Mode I and mode II initiation fracture toughness and resistance curve of medium density fireboard measured by double cantilever beam and three-point bend end-notched flexure tests, *Engineering Fracture Mechanics* 77 (2010), 2537 – 2549
- [29] H. Saidpour et al., Mode II interlaminar fracture toughness of carbon/epoxy laminates, *Iranian Polymer Journal* 12 (2003), 389 – 400
- [30] K. O'Brien, W. Johnston, G. Toland, Mode II Interlaminar Fracture Toughness and Fatigue Characterization of a Graphite Epoxy Composite Material, NASA/TM-2010-216838 (2010)
- [31] C. Rans, Fatigue Delamination Growth Characterization of Bonded Interfaces, Conference Paper, TU Delft (2010)
- [32] J. A. Pascoe, Delamination of Bonded Repairs A Damage Tolerance Approach, Master of Science Thesis, TU Delft (2012)

- [33] R. Rodi, Characterization of the fatigue delamination growth in GFRP for wind turbine blades, Summary of the project results and future possible work, Conference Paper, TU Delft (2011)
- [34] W. Cui, M. Wisnom, M. Jones, An experimental and analytical study of delamination of unidirectional specimens with cut central plies, *Journal of Reinforced Plastics and Composites* 13 (1994), 722 – 739
- [35] L. Kawashita et al., Static and fatigue delamination from discontinuous plies – experimental and numerical investigations, ACCIS, University of Bristol
- [36] G. Allegri et al, A new semi-empirical model for stress ratio effect on mode II fatigue delamination growth, *Composites: Part A* 42 (2011) 733 – 740
- [37] J. Andersons, M. Hojo, S. Ochiai, Empirical model for stress ratio effect on fatigue delamination growth rate in composite laminates, *International Journal of Fatigue* 26 (2004), 597 – 604
- [38] Y. Zhu. Characterization Of Interlaminar Fracture Toughness Of A Carbon/Epoxy Composite Material, Master of Science Thesis, Pennsylvania State University (2009)
- [39] S. Spearing, The Role Of Fiber Bridging In The Delamination Resistance Of Fiber-Reinforced Composites, *Acta Metallurgica et Materialia* 9 (1992), 2191 – 2199
- [40] F. Hélénon, M. Wisnom, S. Hallett, G. Allegri, An approach for dealing with high local stresses in finite element analyses, *Composites: Part A* 41 (2010), 1156 – 1163
- [41] K. Sadananda, A. Vasudevan, Crack tip driving forces and crack growth representation under fatigue, *International Journal of Fatigue* 26 (2004), 39 – 47
- [42] A. Smiley, R. Pipes, Rate Effects on Mode I Interlaminar Fracture Toughness in Composite, *Journal of Composite Materials* 21 (1987), 670 – 687

# Acknowledgments

---

I miei ringraziamenti iniziano con i miei due relatori, prof. Troiani in Italia, René Alderlienzen in Olanda. Al primo la riconoscenza per la simpatia, la spensieratezza e la capacità di affrontare le situazioni senza mai perdere il sorriso, al secondo la gratitudine per avermi accolto, instradato e seguito, e per le belle parole di apprezzamento finali. It was my pleasure.

Grazie anche a tutto il personale del TU Delft e allo Staff del DASML per il continuo supporto, così come ai cari compagni d'ufficio e ai ragazzi dottorandi. Sono stati sei mesi fantastici e formativi.

Ringrazio la mia famiglia tutta, mia madre, mio padre e mio fratello in primis, per essermi sempre stati vicini spiritualmente e fisicamente, soprattutto nel momento più buio, *che la diritta via era smarrita*.

Non lo dimenticherò.

Ai nonni, agli zii tutti, ai cugini e alla mia amata figlioccia un abbraccio profondo.

Gli amici tutti, a ritroso questa volta, iniziando dalla mia Dutch Family, persone vere in un lasso di tempo troppo ristretto, che mi hanno fatto sentire apprezzato come non mai, e mi hanno fatto capire che ovunque nel mondo potrò mettermi in gioco e giocare da titolare. Pauly, Ale, Sere, Giò, Tito, Cata, Martins, French guys, Maria, you are family.

Ai compagni di baldoria e/o università di questi ultimi anni va un grazie per esserci stati sempre nei momenti di serietà e in quelli in cui essa era vietata. A Steh, Albe, Dani, Dome, Dottore, Robax, Burrasca, Lo, Ire, Sere, Irash, Dome, Paolo, Anto, Flavio, Fede, Bardox, Nani, Iris, Vero, Babba, Silvia, Ade&co., ai coinquilini di ieri e di oggi, ai compagni di vita portoghesi, ai compagni di squadra, alle persone incontrate per caso, a quelli che non ho nominato per non rendere i miei ringraziamenti un trattato infinito, vanno la mia stima e il mio riconoscimento per essere stati parte di una vita che mi ha formato, cambiato, preparato a ciò che verrà.

Un pensiero di rito agli amici della madre patria Sardegna e ai miei ex compagni di classe, dai quali la vita credo mi terrà lontano fisicamente, ma che porterò sempre nel cuore.

*I ain't afraid to led it out, I'm unafraid to take that fall, but I have found beyond all doubt, we say more by say nothing at all. (Pantomime)*